Fast Digitizing and Digital Signal Processing of Detector Signals

Roland Hannaske

Januar 2009

WISSENSCHAFTLICH-TECHNISCHE BERICHTE

Forschungszentrum
Dresden Rossendorf

Roland Hannaske

Fast Digitizing and Digital Signal Processing of Detector Signals

**Forschungszentrum
Dresden** Rossendorf

Fast Digitizing and Digital Signal Processing of Detector Signals

Diplomarbeit
Zur Erlangung des akademischen Grades
Diplom-Physiker

vorgelegt von

Roland Hannaske

geboren in Eisenhüttenstadt

Institut für Angewandte Physik
Fachrichtung Physik
Fakultät Mathematik und Naturwissenschaften
der Technischen Universität Dresden

und

Institut für Strahlenphysik
Forschungszentrum Dresden-Rossendorf

2008

1. Gutachter: Prof. Dr. Roland Sauerbrey

2. Gutachter: Prof. Dr. Thomas Cowan

Datum des Einreichens der Arbeit: 30. September 2008

Kurzfassung

Ein auf schnellen Digitizern basierendes Daten-Erfassungs-System, das vor kurzem am Neutronen-Flugzeit Experiment nELBE am supraleitenden Elektronenbeschleuniger ELBE des Forschungszentrums Dresden-Rossendorf aufgebaut wurde, wird mit zwei verschiedenen Detektortypen getestet. Zum einen werden die Vorverstärker-Signale eines hochreinen Germanium Detektors digitalisiert, gespeichert und anschließend verarbeitet. Um die Energie der detektierten Strahlung mit hoher Genauigkeit zu bestimmen, werden der *Moving Window Deconvolution* Algorithmus zur Korrektur des ballistischen Defizits sowie verschiedene Algorithmen zur Pulsformung verwendet. Die Energieauflösung wird in einem Experiment mit der γ-Strahlung einer ^{22}Na Quelle bestimmt und mit der Energieauflösung verglichen, die bei analog verarbeiten Signalen erreicht wird. Zum anderen werden Signale digitalisiert, die von Bariumfluorid- und Plastik-Szintillationsdetektoren stammen. Von diesen Signalen mit einer Anstiegszeit von nur wenigen Nanosekunden soll der Zeitpunkt, zu dem die Wechselwirkung der Strahlung mit dem Detektor stattfand, mit Methoden der digitalen Signalverarbeitung bestimmt werden. Dazu werden verschiedene Zeit-Bestimmungs-Algorithmen angewendet und anhand von Daten aus einem Experiment an nELBE getestet. Die mit diesen Algorithmen erreichten Zeitauflösungen werden sowohl untereinander verglichen als auch mit Referenzwerten, die aus analoger Signalverarbeitung stammen. Zusätzlich zu diesen Experimenten wurden einige Eigenschaften der Digitalisierungs-Hardware gemessen und ein Programm für die Analyse gespeicherter, digitalisierter Signale entwickelt. Die durchgeführten Untersuchungen zeigen, dass das verwendete 10-bit Digitizer-System nicht die Auflösung eines 14-bit peak-sensing ADC erreicht, obwohl das ballistische Defizit vollständig korrigiert werden kann. Hingegen werden bei der Zeit-Bestimmung im sub-ns Bereich bessere Resultate als mit analoger Signalverarbeitung erreicht.

Abstract

A fast-digitizer data acquisition system recently installed at the neutron time-of-flight experiment nELBE, which is located at the superconducting electron accelerator ELBE of Forschungszentrum Dresden-Rossendorf, is tested with two different detector types. Preamplifier signals from a high-purity germanium detector are digitized, stored and finally processed. For a precise determination of the energy of the detected radiation, the moving-window deconvolution algorithm is used to compensate the ballistic deficit and different shaping algorithms are applied. The energy resolution is determined in an experiment with γ-rays from a ^{22}Na source and is compared to the energy resolution achieved with analogously processed signals. On the other hand, signals from the photomultipliers of barium fluoride and plastic scintillation detectors are digitized. These signals have risetimes of a few nanoseconds only. The moment of interaction of the radiation with the detector is determined by methods of digital signal processing. Therefore, different timing algorithms are implemented and tested with data from an experiment at nELBE. The time resolutions achieved with these algorithms are compared to each other as well as to reference values coming from analog signal processing. In addition to these experiments, some properties of the digitizing hardware are measured and a program for the analysis of stored, digitized data is developed. The analysis of the signals shows that the energy resolution achieved with the 10-bit digitizer system used here is not competitive to a 14-bit peak-sensing ADC, although the ballistic deficit can be fully corrected. However, digital methods give better result in sub-ns timing than analog signal processing.

Contents

List of Figures

List of Tables

List of Acronyms and Abbreviations

AC	alternating current
ADC	analog-to-digital converter
ASP	analog signal processing
BGO	bismuth germanate
CFD	constant fraction discriminator
CFT	constant fraction timing
cPCI	compact peripheral component interconnect
CR	capacitor-resistor
DAQ	data acquisition
DC	direct current
DSP	digital signal processing
ELBE	electron linac for beams with high brilliance and low emittance
ELET	extrapolated leading edge timing
ENOB	effective number of bits
FC	fibre channel
FCFT	fitting constant fraction timing
FDDAS	fast digitizing data acquisition system
FWHM	full width at half maximum
HPGe	high purity germanium
JBOD	just a bunch of disks
JTS	JORDANOV trapezoid shaper
LET	leading edge timing
MWD	mowing window deconvolution
ndf	number of degrees of freedom
nELBE	neutron time-of-flight experiment at ELBE
PMT	photomultiplier tube
PSENOB	peak-sensing-equivalent number of bits
RC	resistor-capacitor
SAN	storage area network
SMAR	simultaneous multi-buffer data acquisition and readout
TDC	time-to-digital converter
ZCCFT	zero-crossing constant fraction timing
ZCT	zero-crossing shaper timing

Chapter 1

Introduction

1.1   Analog and Digital Signal Processing

Signal Processing, no matter whether it is done by digital or by conventional analog means, is the part of a measurement, in which a raw signal from a detector is modified in such a way that finally a digitized value of the measured quantity with the best possible accuracy is obtained. A simplified signal chain in analog signal processing (ASP) is sketched in figure 1.1. It consists typically of the detector followed by a preamplifier and a main amplifier. Depending on what is measured, the chain continues with a discriminator - to produce a logical signal for counting or timing measurements - or, in the case of pulse height analysis, with dedicated electronics (pile-up rejector, baseline restorer) and a multi-channel analyzer. Several textbooks [1, 2, 3] deal with this topic and explain underlying electronics, basic principles and applications in nuclear physics experiments but also limitations and problems caused by analog pulse processing.

The requirements to a measuring system in nuclear physics are very high and are not always met by ASP. An ideal measuring system extracts the desired information from all detected events with highest precision even at high count rates, is stable over time, insensitive to any disturbance, compensates systematic deficits of the detector and is cheap. The realization of all these issues is sometimes contradictory in itself and underlies general limitations. Most of the electronics used is based on semiconductor components, which change their properties while temperature changes. Every stage of analog pulse processing may contribute some noise to the signal. An accurate pulse height analysis can cause significant dead time and is impaired by piled-up pulses at high counting rates. The detector response to radiation can vary in a nonlinear way. There are lots of other examples, but nevertheless, since ASP was the first and for a long time only way of pulse processing, big efforts were made to compensate its drawbacks and over decades ASP was and still is used very successfully.

Detector → Preamplifier → Main amplifier → Single-channel analyzer → Counter

Main amplifier → Pile-up rejector, Baseline restorer → Multi-channel analyzer
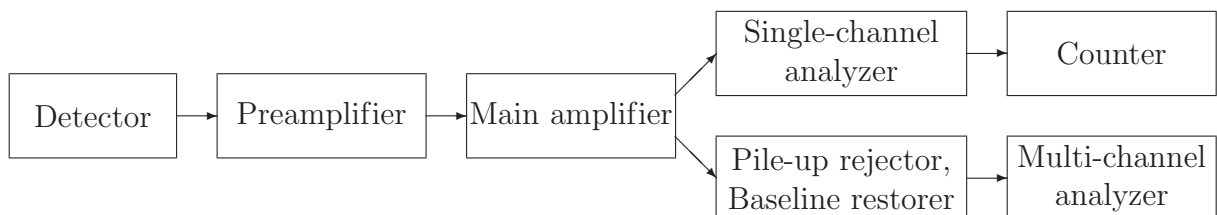
Figure 1.1: Simplified signal chain in analog signal processing for pulse counting (upper branch) or pulse height spectrometry (lower branch).

In digital signal processing (DSP) fast digitizers are used to convert the analog preamplifier signals into digital signals. Then the process of amplifying and shaping is done by digital means, e.g. by filters, shapers or even more complex algorithms for specific problems. Noise characteristics of analog shaping circuits using components which are susceptible to changes in temperature and other environmental disturbances, have no influence anymore. On the other hand, one has to deal with huge amounts of data that have to be transfered, stored and analyzed. Figure 1.2 shows two typical signal chains in DSP. One option is to analyze the digitized data online in field-programmable gate arrays (FPGAs) or digital signal processors and store the results only, while another approach is to store all digitized signals and process them after the end of the experiment offline. But however this is realized, DSP only makes sense if it is competitive to ASP, i.e. DSP must be a feasible solution that delivers equal or better results than ASP.
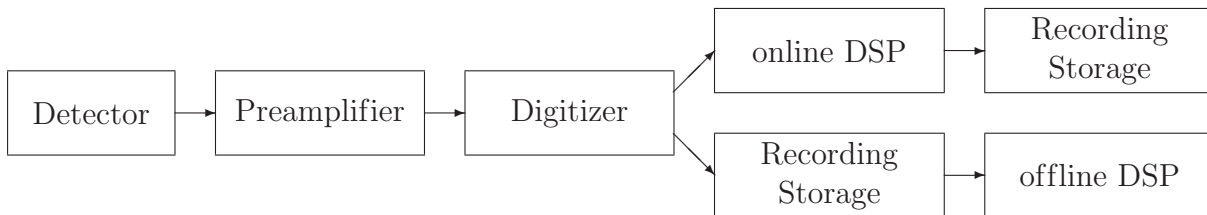
Figure 1.2: Simplified signal chain in digital signal processing performed online (upper branch) or offline (lower branch).

1.2   Nuclear Physics Experiments at ELBE

A good benchmark test for DSP in nuclear physics are experiments which use state of the art ASP. At the radiation source ELBE (Electron Linac for beams with high Brilliance and low Emittance) at Forschungszentrum Dresden-Rossendorf such experiments are performed. ELBE is a superconducting accelerator for electrons up to 40 MeV which are used to generate infrared light in a free-electron laser, X-rays, positrons, fast neutrons or bremsstrahlung [4].

Figure 1.3 shows a sketch of the ELBE bremsstrahlung facility which is used for photoactivation studies on p-process nuclei [5] as well as for photon scattering experiments [6]. The electrons with energies up to 20 MeV generate bremsstrahlung in a radiator made of a thin niobium foil. Afterwards the electrons are deflected into a beam dump, where they are stopped and produce bremsstrahlung again. The high photon flux inside the electron beam dump is used to activate nuclear samples. After the irradiation, these samples are taken to a low background installation where the decay of the produced unstable nuclei is measured using high-purity germanium (HPGe) detectors with high efficiency and high energy resolution. Steering magnets in front of the radiator allow the use of partly polarized off-axis bremsstrahlung. Behind the radiator the γ-beam goes through a hardener, a collimator, a thin deuteron-breakup target for beam monitoring and through the actual target before it is stopped in the photon beam dump. The target nuclei are excited by the bremsstrahlung and deexcite by emitting γ-transitions of discrete energies, which can be detected by one of four HPGe detectors. Each detector is surrounded by an escape-suppression shield made of bismuth germanate (BGO) scintillation detectors. For this experiment a pulse-height analysis of digitized HPGe preamplifier signals and the implementation of digital methods are planned.
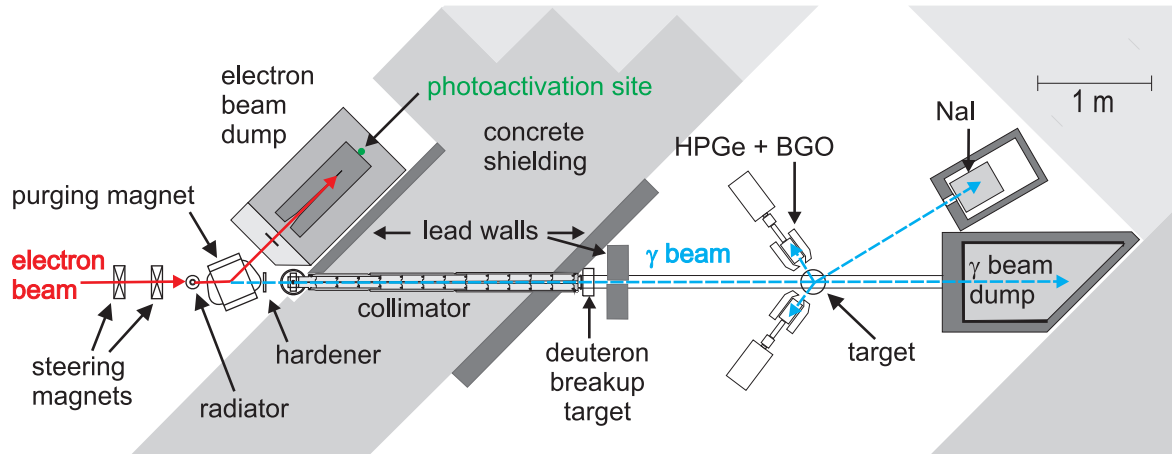
Figure 1.3: The bremsstrahlung facility at the ELBE accelerator with electron beam (red line), photoactivation site (green dot) within the electron beam dump and γ-beam (blue line) for photon scattering experiments. See text for details. Figure from reference [5].

Another experiment at ELBE is the neutron time-of-flight system nELBE [7, 8] shown in figure 1.4. It was developed for neutron cross section measurements relevant for the transmutation of minor actinides in nuclear waste, as well as for applications to fission and fusion reactors. Neutrons are generated in (γ,n)-reactions when the ELBE electron beam hits a radiator and produces bremsstrahlung. In order to cope with the high power density of the electron beam, the radiator is a liquid-lead loop. Its volume is kept small in order to avoid moderation and — because the electron beam has pulse lengths of some picoseconds — to reduce the time during which photo-neutron are produced to a sub-nanosecond region. Thereby, only the neutrons emitted at about 90° from the direction of the electron beam, in which the photon rate is relatively small, are used for experiments and are shaped by a collimator into a well-defined beam, entering the experimental site in the adjacent room. Between the radiator and the collimator there is a holder for ab-
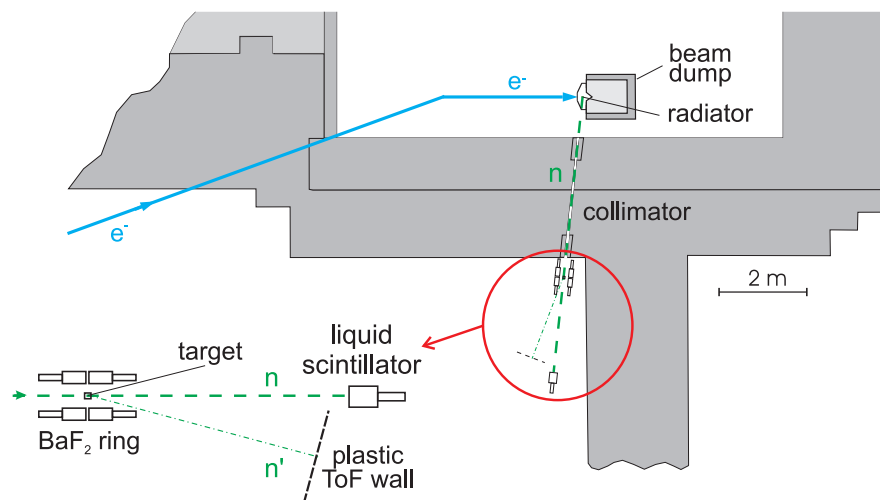
Figure 1.4: The neutron time-of-flight system nELBE with electron beam (blue line), liquid lead radiator (right upper corner) and neutron beam (dashed green line). Target and detector systems (within red circle) are enlarged in the lower left corner. See text for details. Figure from reference [7].

sorbers and samples for transmission measurements. After a flight path of 4 to 7 meters the neutrons can undergo interactions with the scattering target surrounded by an array of 42 barium fluoride (BaF_2) crystals with photomultipliers, that detect γ-rays created in neutron capture or inelastic scattering reactions. The neutron time-of-flight is measured using a liquid scintillator or a wall of plastic scintillators [9]. For all of these detector systems a high time resolution is demanded for a precise determination of the neutron energy, which is distributed between some tens of keV and a few MeV. The fast signals of these detector systems are also well suited to implement and test digital methods for high-resolution timing measurements.

1.3   Objectives and Contents of this Diploma Thesis

The aim of this diploma thesis is to perform first measurements with a digitizer system recently installed at nELBE and to analyze the acquired data with methods of digital signal processing. Therefore, experiments with high-purity germanium detectors and scintillation detectors are to be carried out. An analysis program has to be developed which contains algorithms to determine the energy deposition and the moment of interaction from the digitized signals with high precision. Finally, these algorithms are to be tested and compared to each other as well as to standard methods of analog signal processing.

In chapter 2, a short introduction is given about how digitizing generally works and how it is realized in analog and digital signal processing. The digitizing hardware at nELBE as well as the analysis software is introduced. Pulser signals are processed to measure the dead time of the digitizing hardware.

Chapter 3 starts with some fundamentals about semiconductor diode detectors. The ballistic deficit of a charge-sensitive preamplifier is derived and an algorithm to compensate this effect is discussed. Further algorithms for the shaping of signals are presented. All these algorithms are applied to signals, which were acquired in a measurement with an HPGe detector and ^{22}Na source, and the energy resolution is used the give statements about the precision of these methods.

In chapter 4, barium fluoride and plastic scintillation detectors are introduced and timing algorithms are presented. A measurement at nELBE is described and the acquired signals are analyzed. The parameters of the algorithms are varied in order to determine the optimum time resolution. The results are compared with analogously processed data.

Finally, in chapter 5, conclusions are drawn from the results. Problems and future plans are discussed in an outlook. In the subsequent appendices, the source code of the used algorithms and some mathematical supplements are given.

Chapter 2

Fast Digitizer Data Acquisition and Data Analysis

2.1 Digitizing of Analog Signals

In the processing of analog voltage signals of detectors several applications based on analog-to-digital converters (ADCs) are used which are usually located at the end of the signal chain. The *peak-sensing ADC* delivers a digital signal equal to the peak amplitude during a certain time interval, the *charge-sensitive ADC* (often called QDC) delivers a digital signal equal to the charge collected during a certain time interval and the time-to-digital converter (TDC) delivers a digital signal proportional to the length of a time interval between a start and a stop signal. In digital signal processing it is not enough to know the amplitude, the charge or a characteristic time of the detector signal, but the whole analog signal has to be digitized.

During this digitizing process the continuous signal is reduced to a discrete signal, both in amplitude and time. Using the sampling rate (also: sampling frequency) f_S, which corresponds to a sampling interval $\Delta t = (f_S)^{-1}$, a continuous-time signal $s(t)$ with $t \in \mathbb{R}$ is converted to a discrete-time signal $s_n = s(n \cdot \Delta t)$ with $n \in \mathbb{N}$. This is shown in figure 2.1. Although it is unusual, it should be mentioned that the signal amplitude could be treated in an equivalent way: after the amplitude digitization with an ideal N-bit digitizer corresponding to $M = 2^N$ amplitude values, $s(t)$ could also be represented by $s(t) = s_{offset} + m(t) \cdot \Delta s$, whereas Δs is the so-called code width, $N, M, m(t) \in \mathbb{N}$ and $0 \leq m(t) < M$. Apart from the number of bits N, the *effective number of bits (ENOB)* is often used to take into account that digitized noise decreases the resolution. It is defined by $ENOB = (SNR - 1.76)/6.02$ for a full-scale sine wave with a signal-to-noise ratio SNR in dB. In the ideal case only the quantization error, which is $\sqrt{2/3}$ for a sine wave, contributes to the noise. Then, the signal-to-noise ratio is $SNR = 20 \log(2^N/\sqrt{2/3})$ and it follows that $ENOB = N$.

Fast digitizers are mainly characterized by the parameters f_S and N. For precise amplitude determination, N is chosen that the quantization error, i.e. the deviation between the amplitude of the analog and the digitized signal, does not effect the detector resolution. For example, in high-resolution γ-spectroscopy with germanium detectors, digitizers with $N \geq 13$ bit are used. Contradictory to this, high sampling rates are required, if timing information has to be extracted from signals with short rise times, e.g. signals from scin-
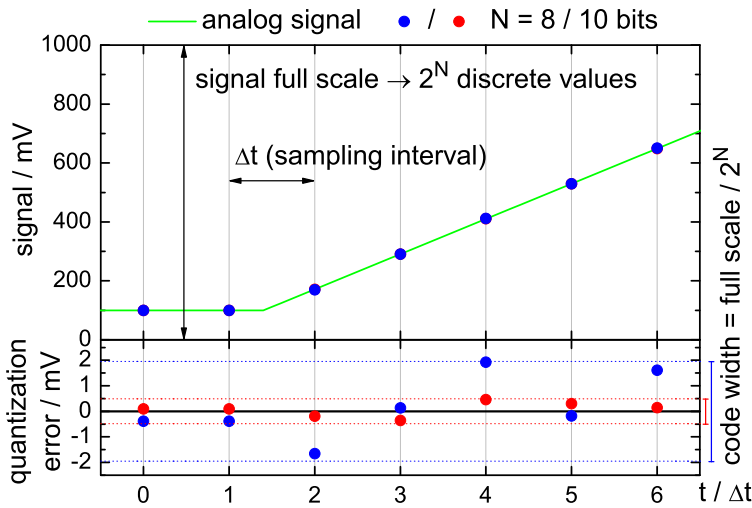
Figure 2.1: Digitizing of an analog signal (upper panel) and corresponding quantization errors (lower panel).
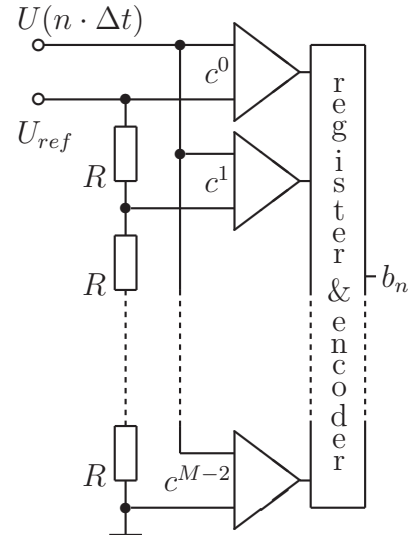
Figure 2.2: Schematic of a flash ADC. See text for details.

tillation detectors in time-of-flight experiments, in which digitizers with $f_S \geq 500\,\mathrm{MS/s}$ (megasamples/second) are used. Fast digital oscilloscopes also use fast digitizers and have high sampling rates up to $20\,\mathrm{GS/s}$, but usually only 8 bit resolution. Even higher sampling rate are usually limited by the analog bandwidth.

There are several technical possibilities to construct ADCs but the majority of them is not practicable for fast digitizing due to their long conversion time t_{conv}. Therefore, the idea of the *flash ADC* (or direct conversion ADC) is to reduce t_{conv} by simultaneous comparisons of the input voltage to successive reference voltages. This principle is shown in figure 2.2. In an N-bit flash ADC the voltage signal $U(n \cdot \Delta t)$ is fed into $2^N - 1$ comparators (c^0, ..., c^{M-2}) together with each one voltage reference signal, which is realized in a

Figure 2.3: Crate with four digitizer cards (upper slots) and one recording card (VMETRO, lower slot). The nELBE FDDAS consists of two of these crates and two JBODs (see text for details).

voltage ladder with a maximum reference voltage U_{ref} applied across $2^N - 2$ resistors R connected in series. The comparators deliver a logical signal containing the information whether the signal is greater than the reference signal or not. All these logical signals are combined in a register and are encoded to a binary sequence b_n of the length N. The drawback of the very short conversion time is the large number of comparators which are needed. That's why fast digitizers have usually only 8 to 12 bit vertical resolution. If very high sampling rates are required so that $t_{conv} > \Delta t$, then a demultiplexer delivers the analog signal to several flash ADCs.

To compare fast digitizers to peak-sensing ADCs, BARDELLI and POGGI introduced the *Peak-Sensing-Equivalent Number of Bits (PSENOB)* [10]. It is defined by

$$PSENOB = ENOB + \frac{1}{2}\log_2\left(\frac{f_S}{k_G^2}\right) - \frac{1}{2} \quad . \tag{2.1}$$

The parameter $k_G^2 = k_{G\star}^2/\vartheta$ describes the influence of a digital filter used to shape the signal, whereas the dimensionless $k_{G\star}$ is between 0.7 and 1.5 depending on the filter and ϑ is a time parameter of the shaper. A "bit-gain" is expected for fast digitizers compared to peak-sensing ADCs with the same ENOB. In the same reference, an example of a digitizer with $ENOB = 11.0$ and $f_S = 100\,\mathrm{MS/s}$ is presented. In this example, a CR-$(RC)^4$ shaper ($k_{G\star}$=0.823) with an optimized shaper time $\vartheta = 6\,\mathrm{\mu s}$ is used, resulting in $PSENOB \approx 15$. The PSENOB of the digitizer system used here is discussed in section 3.4.2.

2.2 FDDAS and DSP at nELBE

The nELBE Fast Digitizing Data Acquisition System (FDDAS) consists of three components: The digitizer cards, the recording cards and the storage device. The *Acqiris DC282* digitizer card[1] [11, 12] allows the sampling of four channels, each at a sampling rate up to $2\,\mathrm{GS/s}$ and a resolution of 10 bit. The cards in the nELBE FDDAS have the *standard* front end options, i.e. the input impedance is $50\,\Omega$, the full scale voltage range can be chosen between $50\,\mathrm{mV}$ and $5.0\,\mathrm{V}$ and the maximum bandwidth is $2\,\mathrm{GHz}$. At this bandwidth a pulse with a rise time θ_{real} will be observed with a value determined by the relation $\theta_{observed}^2 = \theta_{real}^2 + (0.17\,\mathrm{ns})^2$, which is of interest for the sampling of fast-changing signals. The ENOB is between 5.4 and 7.2 depending on the test conditions. The on-board acquisition memory is $256\,000$ points per channel and can be segmented in order to use the *Simultaneous Multi-buffer data Acquisition and Readout mode (SMAR-mode)*. Further adjustable global parameters are the number of sampled points and the trigger delay (number of points stored before the trigger time), while for every channel some local parameters can be adjusted: full scale voltage range, voltage offset, coupling (AC/DC), trigger type (leading edge, window trigger) and trigger threshold. The triggering can either be realized with an internal hardware trigger, while every channel can trigger the whole card, or with an external signal which can be fed to a trigger input of the card. For each trigger a time stamp is generated and tagged to the digitized signals. Figure 2.3 shows four of these digitizing cards in a crate, which connects them via a 64-bit $66\,\mathrm{MHz}$ compactPCI (cPCI) backplane with the recording card located in the lowest slot of the shown crate.

---

[1]The company *Acqiris* was acquired by *Agilent Technologies* in 2006 and the name of the digitizer card was changed to *Agilent U1065A*.

The recording card is a cPCI single board computer, whose task it is to configure and read out the digitizing cards on the one hand and to transfer the data to the storage device on the other hand. At the nELBE FDDAS two different combinations of recording card and storage device are available. The "small" solution, which was not used here, is a 1.6 GHz *Pentium* single board computer with a *Linux* operating system, *Acqiris* drivers and acquisition software. It is remote-controlled via ethernet and connected to an external hard disk, where the data is stored. The "big" solution is a *VMETRO Vortex* system consisting of the single board computer *PowerMIDAS C5000* [13], the storage device *VS-FC41F* [14] and the *SAN Access Kit* [15]. The latter is a fibre channel (FC) host bus adapter and a software suite for the analysis server to provide direct high-speed access to the storage area network (SAN). The *VS-FC41F* is *Just a Bunch Of Disks (JBOD)* which uses twelve physical drives of each 300 GB to create one logical drive but provides no data redundancy. The SAN includes dual 2 Gb/s fibre channels connecting the recording card to the JBOD and the JBOD to the analysis server. The *PowerMIDAS C5000*, which is shown in figure 2.3, is an *IBM 440GX PowerPC* with a *VxWorks* operating system and provides a web-based graphical user interface as well as an *Application Programming Interface (API)* to configure the card via ethernet.

Data acquired with this FDDAS is processed using a dedicated *HP ProLiant DL380 G5 server* [16] with a 1.86 GHz *Intel Xeon* quad-core-processor and 4 GB RAM. Since the data cannot be read directly from the JBOD, an API script [17] copies the data to named pipes. The algorithms, which are described in the following chapters and listed in appendix A, are implemented as functions within a self-developed analysis program using the programming language C and the C++ based program ROOT [18] in its version 5.16.16. For the analysis of signals and spectra the MINUIT fitting package implemented in ROOT is applied. The analysis program also contains several functions for reading meta data and the digitized signals from data files (or pipes). Furthermore, graphical output by predefined ROOT-commands and argument-handling is realized in the program. To run an analysis the program has to be compiled and can then be executed with different arguments and data files, whereas several analyses (even of the same data) using different instances of the compiled program are possible. Thanks to the quad-core processor up to four analyses can be carried out at the same time without a loss in performance.

2.3   Measurement of the Dead Time of the nELBE FDDAS

There are two processes contributing to the dead time of the nELBE FDDAS. On the one hand, the internal hardware trigger needs a certain time t_{dt1} to rearm after an event occurred. This time is given by the manufacturer to be 350 ns. On the other hand, the FDDAS is only ready to trigger if there is free on-board acquisition memory to store another event. The time t_{dt2} that is needed to transfer data points from this memory to the JBOD is theoretically limited by the maximum data transfer rate of the cPCI backplane, which is $64\,\text{bit} \cdot 66\,\text{MHz} = 528\,\text{MB/s}$. The specifications to the manufacturer of the recorder card was, that t_{dt2} should be zero at a trigger rate of up to 1000 detections per second per channel with a frame size of 1000 (i.e. 1000 stored data points per event per channel), within any 30 ms time period.
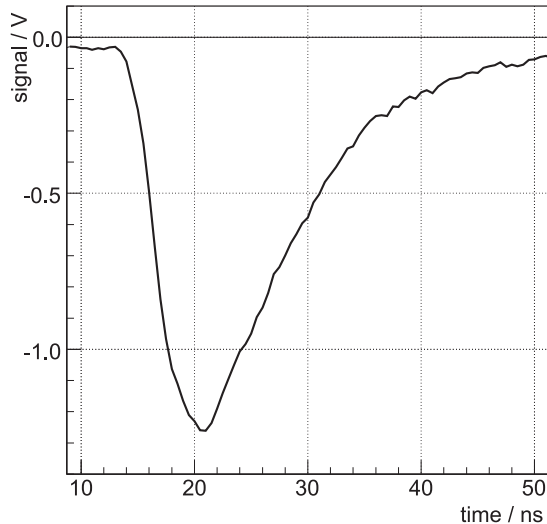
Figure 2.4: Such digitized signals of a pulse generator are used to determine the dead time of nELBE FDDAS.
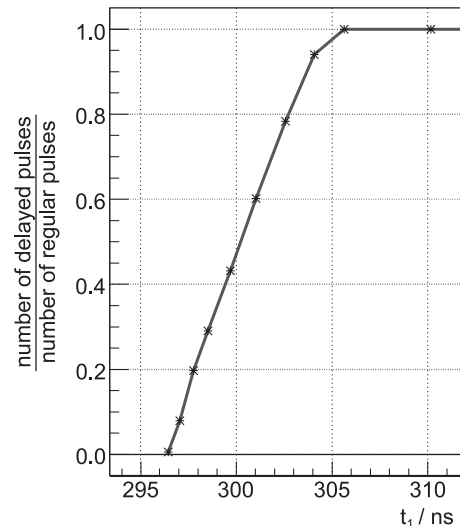
Figure 2.5: Plot of t_1 from equation (2.2) vs. the number of delayed pulses divided by the number of regular pulses. See text for details.

Both contributions are investigated with signals from a BNC BL-2 pulse generator [19] with the pulse repetition rate f_{pulse}. To determine the rearm time t_{dt1} the pulse generator is set to $f_{pulse} \approx 200\,\text{kHz}$ and is operated in the so called double-pulse mode, i.e. every regular pulse is followed by a similar pulse with an adjustable delay t_{delay}, while the regular pulses are separated by the time $(f_{pulse})^{-1}$. Figure 2.4 shows a signal from this pulse generator. The nELBE FDDAS, equipped with one digitizer card and the VMETRO recording card, is used with the parameters $f_S = 2\,\text{GS/s}$, leading edge trigger (negative slope) with a threshold of $-600\,\text{mV}$ and a trigger delay of $P_{trig} = 32$ points.

The time stamps of the acquired signals are analyzed to separate the events into regular pulses and delayed pulses. In a first qualitative investigation, t_{delay} and P, which is the number of acquired data points per event per channel, are varied. From the absence of the delayed pulses the dead time is roughly estimated to be about 300 ns and it turns out that the trigger-rearming process starts after the last point is acquired. In other words, the dead time is the highest value of $(t_{delay} - (P - P_{trig})\Delta t)$ in the case that no delayed pulses are measured.

This is investigated in a more quantitative way with a fixed delay time $t_{delay} \approx 425\,\text{ns}$. Since t_{delay} drifts a little bit, the difference t_{diff} of the time stamps of a regular and of a delayed signal is determined, filled into a histogram and fitted with a gaussian function with the mean value $\bar{t}_{diff}$. This is done for several values of P. The time between the last acquired data point of a regular pulse and the trigger time of the following delayed pulse is determined by

$$t_1(P) = \bar{t}_{diff}(P) - (P - P_{trig})\Delta t \quad . \tag{2.2}$$

A figure of merit, which is the ratio of the number of delayed pulses to the number of regular pulses, is calculated for each value of P and shown in figure 2.5 as a function of t_1. As one can see, all regular pulses are followed by a delayed pulse if $t_1 > t_{dt1} = 306\,\text{ns}$. Below this value the delayed pulse are overlooked partly or fully since the trigger is not rearmed yet.

To investigate the second contribution t_{dt2} coming from the data transfer time, the same pulse generator is used but operated in the normal (single-pulse) mode. Also the nELBE FDDAS is in the same configuration as in the dead time measurement before. The repetition rate f_{pulse} is varied between 3 and 20 kHz. As in the specifications required, 1000 data points per event for each of the four channels are acquired. Thereby, the pulser is connected to one channel only, but if an event occurs the signals of all four channels are acquired. The on-board acquisition memory is divided into two segments of each 128 000 data points per channel in order to use the SMAR-mode. With this specifications, 115 events (each with 1000 data points plus some data points overhead) per channel can be filled in each memory segment. The next 115 events are then filled in the second segment while the first segment is read out and the data is transfered to the JBOD.

By increasing the repetitions rate, the limit of transfer-time free data acquisition is investigated. The transfer time is determined from the time difference between the first events of two subsequent segments, which differs from $115 \cdot (f_{pulse})^{-1}$ if the FDDAS can not trigger the events during the readout process. Up to $f_{pulse} = 10$ kHz, which is equivalent to a data transfer rate of 80 MB/s ($= 2$ Byte $\cdot$ 4 channels $\cdot$ 1000 data points $\cdot$ 10 kHz), no transfer time is measured. At $f_{pulse} = 20$ kHz the data transfer time is about 10 ms, which is needed to read ≈ 1 MB ($= 2$ Byte $\cdot$ 4 channels $\cdot$ 128 000 data points) from the memory. This is equivalent to a data transfer rate of 100 MB/s. Therefore, a maximum data transfer rate of 400 MB/s is expected if all four digitizer cards are installed and used.

Chapter 3

Pulse Height Analysis of HPGe Preamplifier Signals

3.1 Semiconductor Diode Detectors

In several applications of γ-ray detection, semiconductor diode detectors have major advantages compared to other detector types. Their high density makes them more efficient than gas-filled detectors and their extremely good energy resolution makes them more precise than scintillation detectors. Information about general properties of semiconductors like band structure, effects of impurities and dopants, etc. and about different detector types are well described in textbooks, e.g. in KNOLL [1]. Drawing on the example of high-resolution γ-spectroscopy with high-purity germanium (HPGe) detectors, in this section the detection process is explored step by step from the interaction of the radiation with the detector material via the charge collection to the final preamplifier signal. Typical effects influencing the energy resolution such as charge carrier trapping or the ballistic deficit will be discussed.

3.1.1 Interaction of γ-rays with Matter

According to the BEER-LAMBERT law

$$I(l) = I_0 \cdot e^{-\mu \cdot l} \tag{3.1}$$

a beam of monoenergetic γ-rays of the intensity I_0 penetrating into homogeneous matter on a path of the length l is attenuated exponentially with the so called *linear attenuation coefficient* μ. An equivalent formula of equation (3.1) is

$$I(\rho \cdot l) = I_0 \cdot e^{-(\mu/\rho) \cdot (\rho \cdot l)} \tag{3.2}$$

with the mass thickness $\rho \cdot l$, the *mass attenuation coefficient* μ/ρ and the density ρ. Since different processes contribute to the attenuation of the beam — for each process with a fixed probability of occurrence per unit path length — the total linear attenuation coefficient is

$$\mu_{total} = \sum_x \mu_x = \mu_{pea} + \mu_{cs} + \mu_{ppn} + \mu_{ppe} \tag{3.3}$$

with the process-specific linear attenuation coefficients μ_x described below. Figure 3.1 shows μ_{total} and several μ_x in the upper panel and the contribution of several processes to the total attenuation μ_x/μ_{total} in the lower panel as a function of the γ-ray energy E_γ.
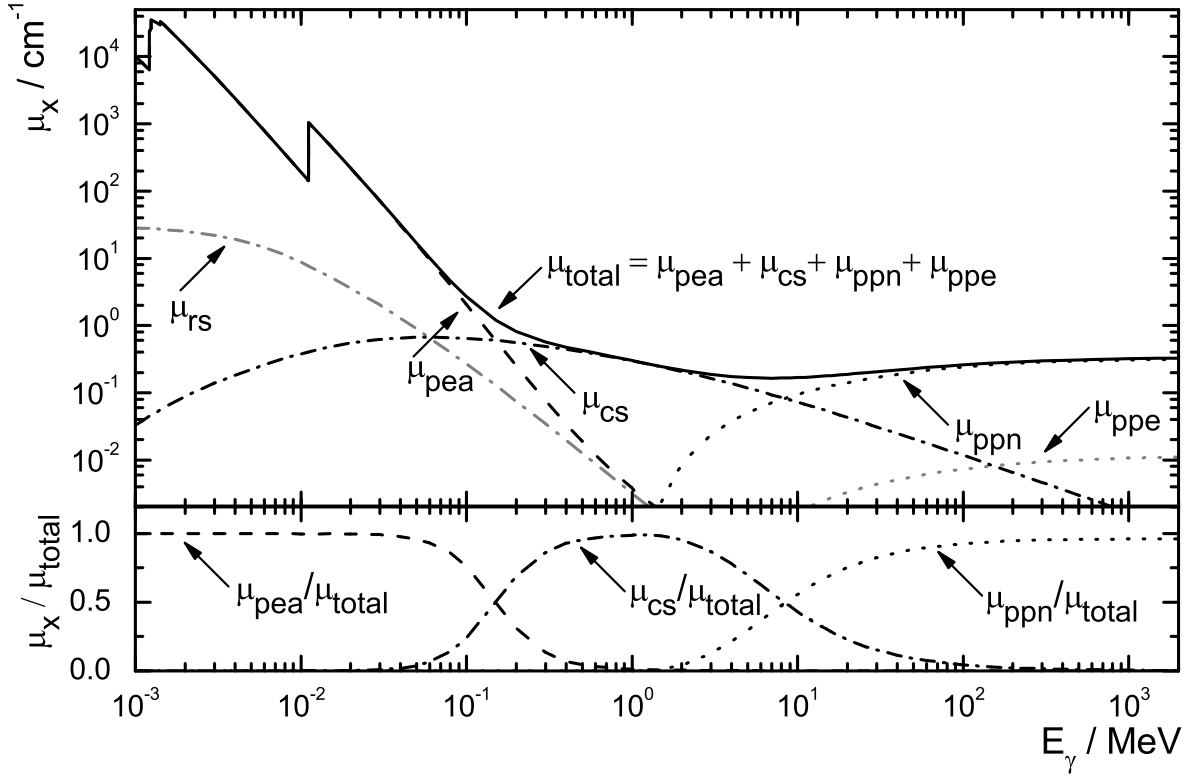
Figure 3.1: Linear attenuation coefficient for γ-rays in germanium. Apart from the total linear attenuation coefficient (μ_{total}, solid line) from equation (3.3), the particular processes photoelectric absorption (μ_{pea}, dashed line), RAYLEIGH scattering (μ_{rs}, dash-dotted gray line), COMPTON scattering (μ_{cs}, dash-dotted black line), pair production in the COULOMB field of a nucleus (μ_{ppn}, dotted black line) and of an electron (μ_{ppe}, dotted gray line) are shown in the upper panel. The major contributions relative to μ_{total} are shown in the lower panel. (Data are taken from the NIST XCOM database [20].)

In the low-energy range (up to 100 keV), μ_{total} is dominated by μ_{pea}, i.e. by **photoelectric absorption**. In this process the incident photon interacts with an atom of the absorbing material and disappears resulting in a so-called photoelectron emitted from one of the bound states of the atom. Since momentum has to be conserved, the photoelectric absorption cannot take place with free electrons. The energy of the photoelectron is $E_e = E_\gamma - E_b$ in which E_b is the binding energy of the photoelectron before the interaction. In the case of germanium the highest binding energies are $E_K = 11.103\,\text{keV}$, $E_{L1} = 1.415\,\text{keV}$, $E_{L2} = 1.248\,\text{keV}$ and $E_{L3} = 1.217\,\text{keV}$ which can be identified in the upper panel of figure 3.1 as discontinuities of μ_{pea} at these energies. After the emission of the photoelectron, the atom refills the vacancy in its electron shells resulting in characteristic X-rays or Auger electrons.

Another, less dominant process in this low-energy range is **coherent scattering or** RAYLEIGH **scattering**, i.e. elastic scattering at the whole atom. Here, the atom is not ionized or exited and the photon retains its energy only changing direction. Since high-resolution γ-spectroscopy aims to measure the photon energy, the detector volume is normally large enough to ensure that coherent scattered photons will be absorbed by other subsequent processes and hence μ_{rs} does not contribute to equation (3.3) here.

Incoherent scattering or COMPTON scattering, expressed by μ_{cs}, is the major contribution to μ_{total} in the mid-energy range (between $200\,\text{keV}$ and $4\,\text{MeV}$). In contrast to coherent scattering, the incident photon interacts with one single bound electron. The photon changes direction and partly transfers its energy to this recoil electron. As a result, the scattered photon retains the energy E'_γ and is deflected through an angle θ with respect to its original direction. Neglecting the binding energy of the electron in this energy range, it can be considered to be free and at rest. The energies of the scattered photon E'_γ and the recoil electron E'_e can be derived using conservation of energy and momentum. They are

$$E'_\gamma = E_\gamma \cdot \frac{1}{1 + \epsilon\,(1 - \cos\theta)} \qquad\qquad E'_e = E_\gamma \cdot \frac{\epsilon\,(1 - \cos\theta)}{1 + \epsilon\,(1 - \cos\theta)} \qquad (3.4)$$

with $\epsilon = E_\gamma/(m_e c^2)$. This shows that for every angle θ the photon retains a portion of its original energy and thus can undergo further interactions or – in the worst case – leave the detector volume before the whole energy of the original photon E_γ is absorbed. From the mean free path $\lambda_{cs} = (\mu_{cs})^{-1} \approx 2 \dots 10\,\text{cm}$ it becomes clear, that large volume detectors are needed to avoid the escape of a COMPTON-scattered photon. Often, these escaping photons can be detected in scintillators surrounding the HPGe detector in order to reject events without the full energy.

In the high-energy range (above $10\,\text{MeV}$) **pair production** is the dominant interaction mechanism. Within a COULOMB-field, an electron-positron pair can be created while the incident photon disappears. One distinguishes between μ_{ppn} for the pair production in the COULOMB-field of a nucleus with an energy threshold of two electron rest masses and μ_{ppe} for the less probable pair production in the COULOMB-field of an electron with an energy threshold of four electron rest masses. The remaining energy $E_{pp} = E_\gamma - 2m_e c^2$ is transferred to the created electron and positron as kinetic energy and also to the nucleus or electron as recoil energy resulting from the conservation of momentum.

Except for coherent scattering, all these processes decrease the energy of the incident photon and create electrons and positrons. These light charged particles loose their energy in matter, too. Their main interaction mechanisms are collisions resulting in ionized or excited atoms and radiative losses due to coulomb interactions resulting in bremsstrahlung, whereas the ratio of the specific energy losses of these processes is $\approx EZ/700$ for electrons with the energy E in MeV in a material with the atomic number Z. Slowed down positrons will annihilate with an electron of the absorbing material and two or more photons are created. Secondary electromagnetic radiation follows the same interaction mechanisms as the γ-rays described above.

Crystalline materials with a periodic lattice are well described using models of delocalized electrons which arrange in so-called bands of allowed energies with gaps between these bands. The energetically highest band that is completely filled is called valence band. The electron population of the next band above (conducting band) and the band gap in between categorize the material into a metal, a semiconductor or an insulator. In the case of the semiconductor the band gap is relatively small and electrons from the valence band can be transferred to the conducting band, while a hole is left at the electron's position. The energy necessary for the creation of one electron-hole pair is for example $\varepsilon = 2.96\,\text{eV}$ for germanium and can be gained from the deceleration of moving charged particles.

3.1.2 Charge Collection

An HPGe detector is a crystal of germanium in which the concentrations of acceptor and donor impurities are nearly zero. These small impurities, which always remain in the material, are used to classify germanium as ν-*type* (high-purity n-type) or π-*type* (high-purity p-type) depending on whether the donors or the acceptors prevail. On the crystal, contacts of high donor or acceptor concentration (n$^+$- or p$^+$-contacts) are created and a high voltage is applied on the resulting n$^+$-p or p$^+$-n junction. With this reverse biasing, a depleted zone is formed that normally reaches through the whole detector volume, in order to separate electron-hole pairs created in any place inside the detector. Finally the electrons and holes drift with characteristic velocities v_e and v_h along the electric field lines towards the contacts, where they form the detector current $I_{det}(t)$. The drift velocities v_e and v_h are both strongly depending on the electric field strength and the temperature. Hence a sufficient overvoltage is applied to saturate the drift velocities. The detector volume is cooled down to the temperature of liquid nitrogen anyhow to reduce the leakage current through the junction to acceptable levels.

The estimation of a mean free path of several centimeters in the mid-energy range is followed by the requirement for large volume detectors. Such detectors are realized in an coaxial configuration with one contact on the inside and the other one on the outside. Usually, *closed-ended coaxial* detectors – with the closed end directed onto the radiation source – are used instead of *true coaxial* detectors. Compared to planar detectors, the drawback of the higher volume and the dedicated geometry is a more complicated field strength distribution and stronger varying drift path lengths. These two effects cause position-sensitive drift times and lead to complicated shapes of the detector current $I_{det}(t)$. Another influence on the shape of the detector current are trapping and detrapping processes. Due to crystal imperfections, interstitial impurities or radiation damage (especially by fast neutrons) there are so called traps, which can catch the charge carriers and inhibit their drifting towards a contact. This statistical process can lead to a permanent loss of charge carriers or, if the trapped charge carriers are detrapped again, to a delayed arrival at the contact. As mentioned above, the incident photon is not necessarily absorbed at its first interaction, but can be scattered and undergo further interactions at other places within the detector, which is also true for the created secondary radiation that can move through the detector. Hence, the detector current is usually a superposition of currents created in a cascade of multiple interactions.

The following four representative examples show the influence of the charge collection process to the preamplifier signal. These examples are revived in section 3.2.1 to demonstrate how this influence is compensated by DSP algorithms. The process of charge collection shall be represented by the four normalized detector currents

$$I_1(t) = \begin{cases} Q_0/\theta & : & 0 \leq t < \theta \\ 0 & : & \theta \leq t \end{cases}$$

$$I_3(t) = e^{-t/\theta} \cdot Q_0/\theta \quad : \quad 0 \leq t$$

$$I_4(t) = \delta(t) \cdot Q_0$$

$$I_2(t) = \begin{cases} 0.75 \cdot Q_0/\theta & : & 0 \leq t < \theta \\ 0.25 \cdot Q_0/\theta & : & \theta \leq t < 2\theta \\ 0 & : & 2\theta \leq t \end{cases} \tag{3.5}$$

whereas $I_i(t) = 0$ for $t < 0$. θ is a characteristic charge collection time, Q_0 is the total

collected charge and $\delta(t)$ is the DIRAC delta function. The collected charge is

$$Q_i(t) = \int_{-\infty}^{t} I_i(t')dt' \quad . \tag{3.6}$$

$I_i(t)$ and $Q_i(t)$ are shown in figures 3.2 and 3.3 for $i \in \{1, 2, 3\}$. $Q_4(t)$ is not shown since it is constant at Q_0. The shapes of $I_i(t)$ in equation (3.5) simplify the statements on the charge collection process: I_1 and I_2 can be interpreted as the current from a single interaction in a homogeneous electric field for $v_e = v_h$ and $v_e \neq v_h$, respectively, I_3 as combined effects from drift time variations, multiple interactions and trapping and I_4 as an ideal pulse with zero drift time.
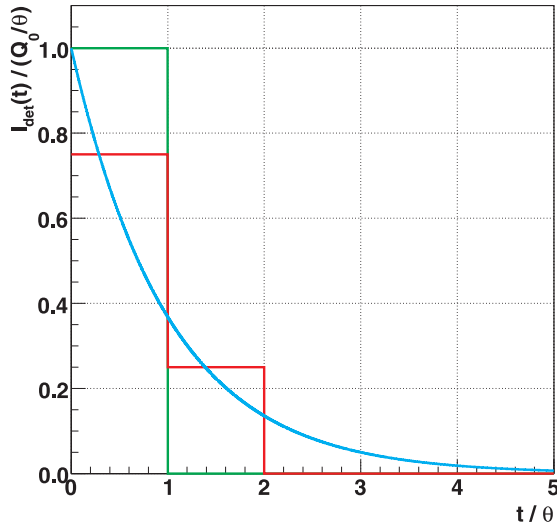
Figure 3.2: Detector currents $I_1(t)$ (green line), $I_2(t)$ (red line) and $I_3(t)$ (blue line) from equation (3.5).
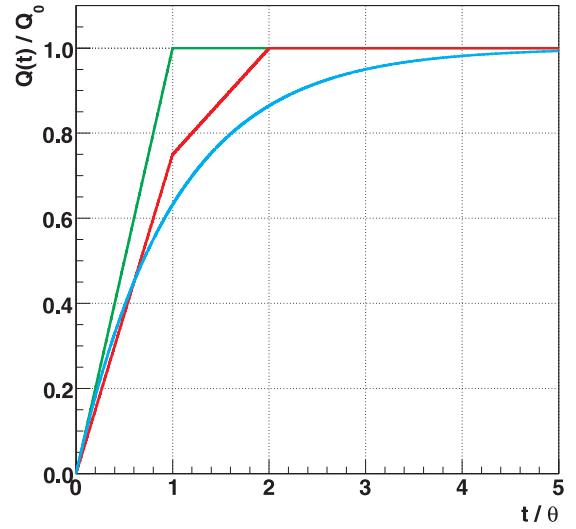
Figure 3.3: Detector charges $Q_1(t)$ (green line), $Q_2(t)$ (red line) and $Q_3(t)$ (blue line) from equation (3.6).

3.1.3 Preamplifier

The function of a preamplifier is not only to amplify the pulse but mainly to interface the detector to the amplifier. Figure 3.4 shows a schematic of a charge-sensitive preamplifier connected to a reverse-biased semiconductor diode detector. The detector is represented by its capacitance C_D, its generated current signal $I_{det}(t)$, its bias resistor R_b and its bias voltage U_b and is coupled to the inverting input of an operational amplifier via a DC-blocking capacitor C_c. The operational amplifier is supplied by V_{S-} and V_{S+}, which are usually symmetric. Its non-inverting input is grounded and its output $U(t)$ is fed back to its inverting input via a resistor R_f and a capacitor C_f connected in parallel. In this feedback-circuit, the charge generated within the detector is collected in the capacitor C_f which then is discharged across the resistor (so called *resistive feedback preamplifier*)[1]. Without discharging, the capacitor would fully charge and the output signal would saturate after a certain number of signals. Then the preamplifier would become insensitive to further detector signals. A feature of the charge-sensitive preamplifier is, that its output signal $U(t)$ is only a function of R_f, C_f and $I_{det}(t)$ but not of the detector capacitance C_d

---

[1]Another method to reset the capacitor is to use a transistor (so called *transistor reset preamplifier*).
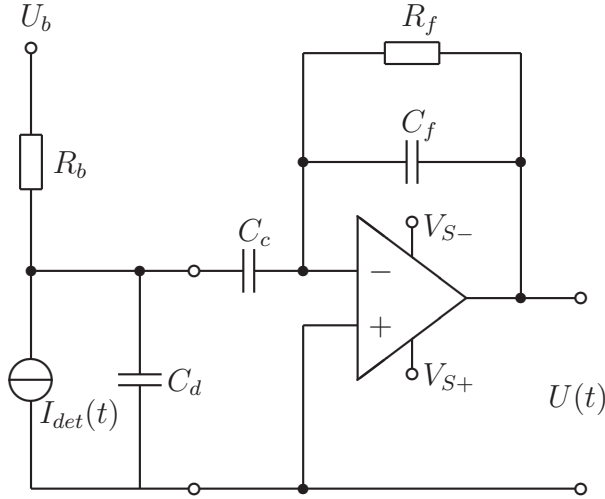
Figure 3.4: Schematic of a reverse-biased semiconductor diode detector connected to a charge-sensitive preamplifier. See text for detailed description.
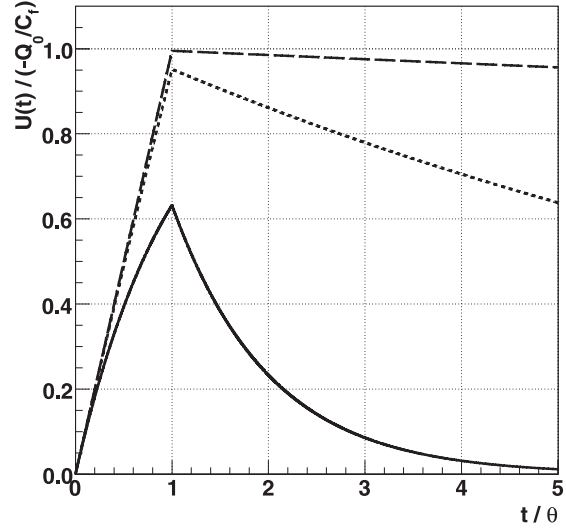
Figure 3.5: Calculated preamplifier signal $U_1(t)$ from equation (B.9) with $\theta/\tau = 1$ (solid line), $\theta/\tau = 0.1$ (dotted line) and $\theta/\tau = 0.01$ (dashed line).

that may depend on U_b.

The proper choice of the feedback resistor R_f is a matter of relative importance, because several effects are influenced by it. On the one hand, thermal noise associated with the feedback resistor, which is one of the significant contributors to preamplifier noise, and the ballistic deficit discussed below are decreased by increasing R_f. One the other hand, a high value of R_f causes a long decay time constant τ and pulses will sit on the tail of their previous pulse more often. This effect is called pile-up and normally does not cause trouble, since it is removed by subsequent shaping in the main amplifier. However, the operational amplifier only provides a linear amplification for output signals $V_{S-} < U(t) < V_{S+}$ and hence can saturate if the count rate becomes too high.

In appendix B.1 the response $U(t)$ of a resistive feedback preamplifier to a detector current signal $I_{det}(t)$ is derived. With the constraints $I_{det}(t) = 0$ for $t < 0$ and $U(t) = 0$ for $t < 0$ it is

$$U(t) = -\frac{1}{C_f} \int_0^t I_{det}(t') \cdot e^{-(t-t')/\tau} dt' \tag{3.7}$$

with the time constant $\tau = R_f C_f$. The responses $U_i(t)$ of the detector currents $I_i(t)$ from equation (3.5) and their minima $U_i^{min} = U_i(t_i^{min})$ can be found in appendix B.1, too. $U_1(t)$, $U_2(t)$ and $U_3(t)$ are shown in figures 3.5, 3.6 and 3.7 for different ratios θ/τ. The ideal case $U_4(t)$ is not shown since it is a simple exponential decay. For $\theta/\tau \to 0$ the preamplifier output $U_i(t)$ merges into $-Q(t)/C_f$ from equation (3.5) shown in figure 3.3. Higher values of θ/τ result in a reduced amplitude. This effect is called *ballistic deficit*, which is defined here by the fractional reduced amplitude $BD_i = 1 - U_i^{min}/(-Q_0/C_f)$. It
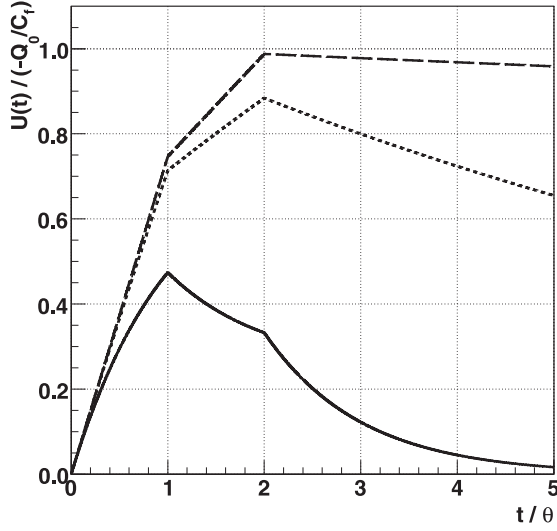
Figure 3.6: Calculated preamplifier signal $U_2(t)$ from equation (B.13) with $\theta/\tau = 1$ (solid line), $\theta/\tau = 0.1$ (dotted line) and $\theta/\tau = 0.01$ (dashed line).
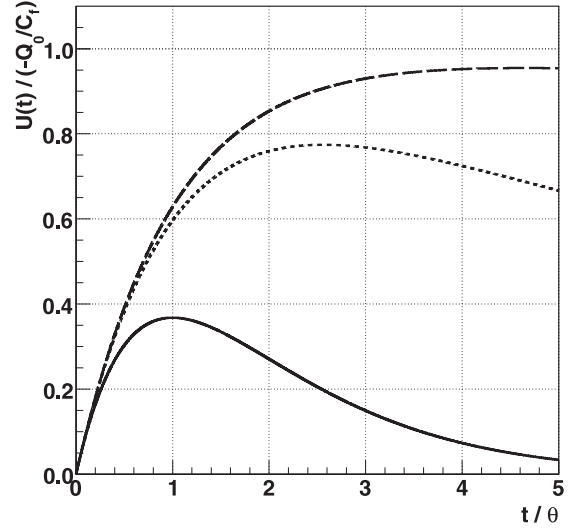
Figure 3.7: Calculated preamplifier signal $U_3(t)$ from equation (B.17) with $\theta/\tau = 1$ (solid line), $\theta/\tau = 0.1$ (dotted line) and $\theta/\tau = 0.01$ (dashed line).

is

$$BD_1 = 1 - \frac{\tau}{\theta}\left(1 - e^{-\theta/\tau}\right) \tag{3.8}$$

$$BD_2 = \begin{cases} 1 - 0.75 \cdot \dfrac{\tau}{\theta}\left(1 - e^{-\theta/\tau}\right) & : \quad \theta \geq \tau \cdot \ln\frac{3}{2} \\[2mm] 1 - 0.25 \cdot \dfrac{\tau}{\theta}\left(1 + 2 \cdot e^{-\theta/\tau} - 3 \cdot e^{-2\theta/\tau}\right) & : \quad \theta < \tau \cdot \ln\frac{3}{2} \end{cases} \tag{3.9}$$

$$BD_3 = \begin{cases} 1 - \left(\dfrac{\theta}{\tau}\right)^{\theta/(\tau-\theta)} & : \quad \tau \neq \theta \\[2mm] 1 - e^{-1} & : \quad \tau = \theta \end{cases} \tag{3.10}$$

$$BD_4 = 0 \tag{3.11}$$

and is obviously independent from the signal charge Q_0. In figure 3.8 the ballistic deficits (except BD_4) are shown depending on the ratio θ/τ.

The most important goal of signal reconstruction of either ASP or DSP is to reduce the effect of ballistic deficit while staying insensitive to electronic noise, pile-up or other effects. According to GOULDING and LANDIS [21], a photon with the energy E_γ detected within a large-diameter coaxial germanium detector does not result in a sharp line in the pulse height spectrum, but in a broadened peak with a total full width at half maximum (FWHM) W_T, which can be written as

$$W_T^2 = W_n^2 + 2.35^2 \epsilon F \cdot E_\gamma + A^2 \cdot E_\gamma^2 \quad . \tag{3.12}$$

The first term of equation (3.12) is the contribution of any electronic noise, which is independent of E_γ and the second term is the contribution of non-statistical sequences of individual process in the charge collection with the FANO factor $F \approx 0.1$ and the energy per electron-hole pair $\epsilon = 2.96\,\mathrm{eV}$, which are both assumed to be independent of E_γ. The last term is the contribution of the ballistic deficit with a constant A independent of E_γ.
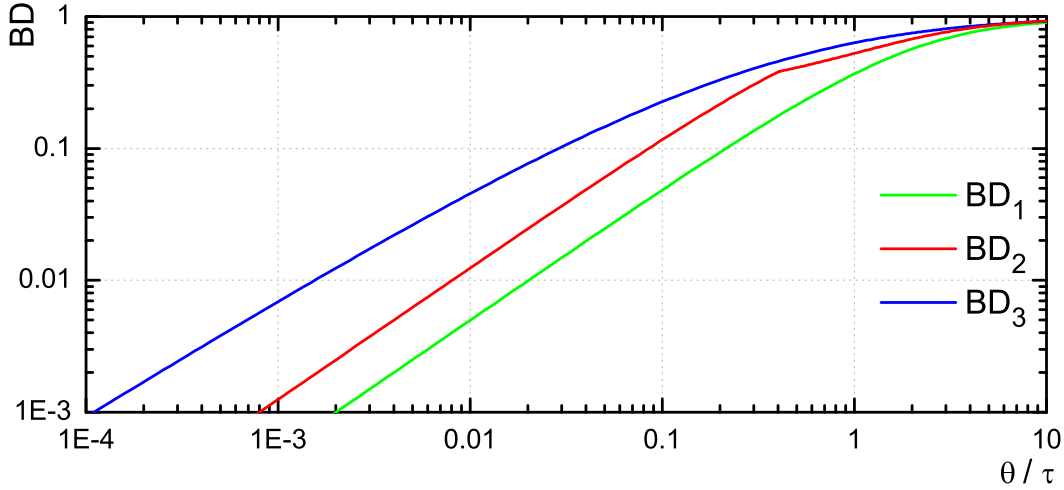
Figure 3.8: Ballistic deficits BD_1 (green line), BD_2 (red line) and BD_3 (blue line) from equations (3.8), (3.9) and (3.10) depending on the ratio θ/τ.

From equations (3.8), (3.9) and (3.10) it becomes clear, that for a fixed amplitude of the preamplifier the measured value can fluctuate due to fluctuations in the signal's rise time. At high energies the ballistic deficit is the major contribution to the energy resolution, especially for large-volume detectors and if the time constant τ is chosen small in order to reduce pile-up at high count rates. From that, the importance of a ballistic deficit correction becomes clear especially for higher energies.

3.2   Algorithms for Pulse Height Analysis

Since effects associated with the analog shaping process like undershoot or baseline shift do not occur in the digital shaping process, there are — apart from the pile-up problem at high count rates — three things left which are important for pulse height analysis of preamplifier signals: (a) the compensation of the ballistic deficit, (b) the reduction of fluctuations, and (c) a shape suitable for a precise determination of the pulse height Therefore, in this section three groups of algorithms are introduced that deal with these three requirements: (a) algorithms for finite decay-time correction, (b) filter and (c) shaper. In spite of this categorization it should be mentioned that filters may also shape the signal and that shapers usually reduce the fluctuations of the signal, too. For all algorithms the following nomenclature is arbitrary chosen: v_n is the digitized input signal to be processed and s_n is the output signal of the algorithm.

3.2.1   Finite Decay-Time Correction

In appendix B.1 the response $U(t)$ of a resistive feedback charge-sensitive preamplifier with a decay time constant τ to a detector current signal $I_{det}(t)$ is derived. With the constraints $I_{det}(t) = 0$ for $t < 0$ and $U(t) = 0$ for $t < 0$ it is

$$U(t) = -\frac{1}{C_f} \int_0^t I_{det}(t') \cdot e^{-(t-t')/\tau} dt' \quad . \tag{3.13}$$

This formula can be interpreted as a convolution of the detector current $I_{det}(t)$ with the impulse response of the preamplifier since it can be rewritten as

$$
\begin{aligned}
U(t) &= -\frac{1}{C_f} \int_{-\infty}^{+\infty} I_{det}(t') \cdot H(t-t') \cdot e^{-(t-t')/\tau} dt' \\
&= I(t) * \left(-\frac{1}{C_f} \cdot H(t) \cdot e^{-t/\tau} \right)
\end{aligned} \tag{3.14}
$$

in which $*$ is the convolution operation and $H(t)$ is the HEAVYSIDE step function.

Using equation (3.13) the response for specific currents $I_{det}(t)$ with a characteristic rise time θ is derived in section 3.1 and the ballistic deficit BD is introduced as an intrinsic property of the preamplifier in the case $\theta/\tau > 0$, which is valid for any realistic measurement with $\theta > 0$ and a finite decay time constant τ. The ballistic deficit is the major contribution to the FWHM at high γ-ray energies. To overcome this effect, BÜCHNER ET AL. developed a digital filter algorithm called *Moving Window Deconvolution (MWD)* [22, 23, 24] that restores the original charge information and shapes the preamplifier signal. The MWD is expressed by

$$
s_n = v_n - v_{n-m} + \alpha \sum_{i=n-m}^{n-1} v_i \tag{3.15}
$$

$$
\alpha = 1 - e^{-\Delta t/\tau} \tag{3.16}
$$

whereas m is a number of samples used for the correction, Δt is the sampling interval and τ is the decay time constant of the preamplifier. In figure 3.9 the response of the MWD to $U_1(t)$, $U_2(t)$ and $U_3(t)$ from equations (B.9), (B.13) and (B.17) is shown. Comparing to figure 3.3 one sees that the MWD algorithm converts the preamplifier output signal into the output signal of the ideal integrator for the first m samples. In the case $m \to \infty$ and according to equation (3.5), the preamplifier signals $v_n^{(i)} = U_i(n\Delta t)$ from figures 3.5, 3.6 and 3.7 should result in $s_n^{(i)} = -Q_i(n\Delta t)/C_f$ and have the shape of their charge signals from figure 3.3. This is true for the zero risetime pulse $U_4(t)$, but not for any other signal, if the sampling interval Δt is not chosen as small relative to the characteristic time constants θ and τ. Applying the MWD with $m \to \infty$ to $U_1(t)$ and $U_3(t)$ from equations (B.9) and (B.17) one finds

$$
s_n^{(1)} \overset{\theta < n\Delta t}{=} -\frac{Q_0}{C_f} \cdot \frac{\tau}{\Delta t} \left(1 - e^{-\Delta t/\tau} \right) \overset{\Delta t \ll \tau}{\approx} -\frac{Q_0}{C_f} \tag{3.17}
$$

$$
s_n^{(3)} \overset{n \to \infty}{=} -\frac{Q_0}{C_f} \cdot \frac{\tau}{\tau - \theta} \left(1 - \frac{1 - e^{-\Delta t/\tau}}{1 - e^{-\Delta t/\theta}} \right) \overset{\Delta t \ll \tau, \theta}{\approx} -\frac{Q_0}{C_f} \quad . \tag{3.18}
$$

In figure 3.10 this small variation is shown for $s_n^{(3)}$ in the case $\tau_f = 100\,\mu s$ (solid blue line) and $\tau_f = 1\,\mu s$ (solid gray line) with $\theta = 0.1\,\mu s$ each. Another variation occurs if the decay time constant of the resistive feedback preamplifier τ_f and the decay time constant τ_{MWD} given to the MWD algorithm as a parameter do not match, which is shown in figure 3.10 for $s_n^{(3)}$, too.

Choosing $m \to \infty$ allows the use of shapers from subsection 3.2.3 while choosing a finite value of m results in the truncated signal of the ideal integrator. In both cases, the characteristic shaper length has to be longer than the time needed to collect the whole charge.
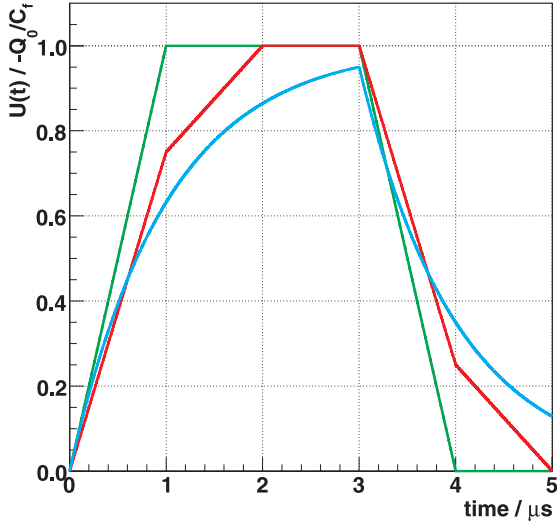
Figure 3.9: Response s_n of the MWD with $m = 6000$ to $U_1(t)$ (green line), $U_2(t)$ (red line) and $U_3(t)$ (blue line) each with $\tau = 1\,\mu s$ and $\theta = 1\,\mu s$ from equations (B.9), (B.13) and (B.17). $\Delta t = 0.5\,ns$. Compare with figure 3.3.
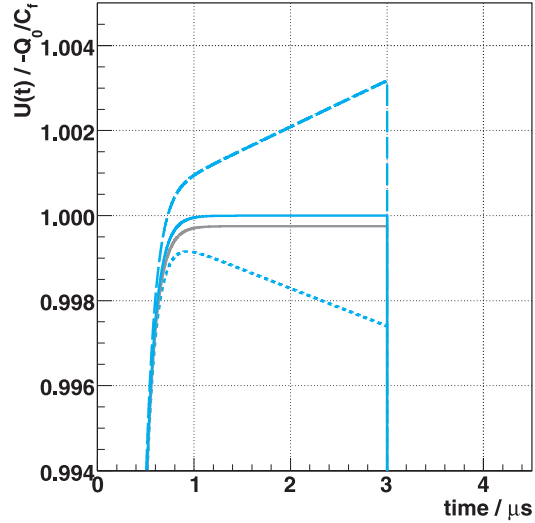
Figure 3.10: Pulse height variations in the response s_n of the MWD with $m = 6000$ to $U_3(t)$ with $\theta = 0.1\,\mu s$ from equation (B.17). $\Delta t = 0.5\,ns$.
$\tau_f = 1\,\mu s$ (gray line)
$\tau_f = 100\,\mu s$ (blue lines)
$\tau_{MWD} = 0.9\,\tau_f$ (dashed line)
$\tau_{MWD} = \tau_f$ (solid lines)
$\tau_{MWD} = 1.1\,\tau_f$ (dotted line)

In the examples shown here, this time has to be θ for $U_1(t)$, 2θ for $U_2(t)$ and $\approx 5\theta$ for $U_3(t)$. The latter is not valid in figure 3.9 where $m \cdot \Delta t = 6000 \cdot 0.5\,ns = 3\,\mu s$ but the rise time constant of $U_3(t)$ is $\theta = 1\,\mu s$, so the maximum amplitude is proportional to the charge collected after $m \cdot \Delta t$.

After the MWD has been published, JORDANOV and KNOLL presented an algorithm for the correction of the ballistic deficit, which they created with a method called *digital synthesis* [25]. This trapezoidal shaping algorithm is given by

$$
\begin{aligned}
d_n &= v_n - v_{n-k} - v_{n-k-m} + v_{n-2\cdot k-m} \\
p_n &= p_{n-1} + d_n \\
s_n &= s_{n-1} + N \cdot (p_n + M \cdot d_n)
\end{aligned}
\tag{3.19}
$$

with the slope length k, the plateau length m, the decay time constant of the sampled exponential signal M and a normalization factor $N = 1$. In appendix B.3 the parameters M and N are derived using an exponentially decaying signal $v_n = A \cdot e^{-n\Delta t/\tau}$. One finds

$$
M = \frac{1}{e^{\Delta t/\tau} - 1} \approx \tau/\Delta t
\tag{3.20}
$$

$$
N = \frac{(1-c)^2}{M + k - (M + k + 1) \cdot c - M \cdot c^k + (M + 1) \cdot c^{k+1}}
\tag{3.21}
$$

with the abbreviation $c = e^{-\Delta t/\tau}$. The identity of this *Jordanov-Trapezoid-Shaper (JTS)* with the parameters $k = 1$, $m = l - 1$ and the MWD with the parameter $m = l$ is shown in appendix B.4.

3.2.2 Filter

Input signals

To illustrate the filter and shaper algorithms, their response to typical input signals, which are shown in figure 3.11, is investigated. One realistic example is the offset-corrected, negative HPGe preamplifier signal, which is digitized with the nELBE FDDAS with 10 bit and a sampling rate of $f_S = 2\,\mathrm{GS/s}$ for $5\,\mathrm{\mu s}$ resulting in a discrete time-signal r_n with $0 \leq n < 10000$. The amplitude of this signal is $\approx -25\,\mathrm{mV}$, its trigger time (where half the amplitude is reached) is $\approx 1.6\,\mathrm{\mu s}$, its rise time (time between 10% and 90% of the amplitude) is $\approx 250\,\mathrm{ns}$ and its decay time constant is $\approx 60\,\mathrm{\mu s}$. Using this decay time constant, the response of the MWD to r_n is u_n. For a better graphical representation the noisy signals, like u_n or the response of some filters to u_n, are smoothed by digital means using the moving average filter (see below) with a window length of 100 samples.

To have an ideal, noise-free signal, a modified HEAVYSIDE step function

$$h_n = \begin{cases} 0.0 & : & n < 1600 \\ -25.0 & : & n \geq 1600 \end{cases} \tag{3.22}$$

is used to determine the so called step response of the algorithms. The reason for modifying the HEAVYSIDE step function is to have an amplitude similar to u_n and to plot both in the same graph. Furthermore h_n represents a preamplifier signal with zero rise time and infinite decay time, which is ideal to determine the signal amplitude.

If input signals starting at a certain point v_0 are to be processed, assumptions for the unknown values for $n < 0$ are necessary. The simplest thing is to assume that any value is zero for $n < 0$, although this means that a signal with an offset is similar to a step function at $n = 0$. As a result of this, the shaper will give a start-up response, which can disturb the response to the signal, if the length of the shaper is in the order of the signal length. In this case an offset compensation, that can can be realized easily by subtracting the signal's baseline average from the signal, is indispensable.

High-Pass Filter (CR Filter, Differentiator)

Some fundamental circuits in analog electronics are resistor-capacitor circuits (RC circuits). Working exactly like a voltage divider, an input voltage is applied across the impedances of a capacitor (with the capacitance C) and a resistor (with the resistance R) connected in series or parallel and the output is the voltage across one impedance. Considering a series connection, the voltage across the resistor is the output of a passive, analog, first-order high-pass filter with a time constant $\tau_{analog} = R \cdot C$ and a cutoff frequency $1/\tau_{analog}$. Starting from this analog filter and the sampling interval Δt, its digital representation is derived in appendix B.2. It is

$$s_n = \frac{\tau}{\tau + \Delta t} \cdot (s_{n-1} + v_n - v_{n-1}) \tag{3.23}$$

and is valid for $\Delta t \ll \tau$. This constraint becomes obvious in the simple example $\Delta t = \tau$ and $v_n = 1$ for $0 \leq n$, in which $s_0 = 1/2$ instead of $s_0 = 1/e$. Figure 3.12 shows the response of the high-pass filter for different time constants τ.

Low-Pass Filter (RC Filter, Integrator)

In the series RC circuit mentioned above, the voltage across the capacitor is the output of a passive, analog, first-order low-pass filter with a time constant $\tau_{analog} = R \cdot C$ and a cutoff frequency $1/\tau_{analog}$. Its digital representation (in the case $\Delta t \ll \tau$)

$$s_n = \frac{\tau}{\tau + \Delta t} \cdot s_{n-1} + \left(1 - \frac{\tau}{\tau + \Delta t}\right) \cdot v_n \tag{3.24}$$

is derived in appendix B.2 as well. Figure 3.13 shows the response of the low-pass filter for different time constants τ.

Moving Average Filter

In general, a moving average (MA) filter is the weighted sum of a certain number l of data points with specific, relative positions to the current data point v_n. Usually v_n is at the end (*prior moving average*) or in the middle (*central moving average*) of this sample of l data points, leading to the iterative equations

$$s_n^{prior} \quad = \sum_{i=0}^{l-1} w_i \cdot v_{n-i} \qquad \text{with } l \in \mathbb{N}$$

$$s_n^{central} = \sum_{i=0}^{l-1} w_i \cdot v_{n-i+a} \qquad \text{with } a \in \mathbb{N}, l = 2 \cdot a + 1$$

whereas w_i is a weighting function, for example:

$$w_i = w^{const} = 1 \qquad\qquad\qquad s_n \text{ is an unweighted moving sum}$$

$$w_i = w^{mean} = \frac{1}{l} \qquad\qquad\qquad s_n \text{ is a moving arithmetic mean}$$

$$w_i = w_i^{lin} \quad = \frac{2 \cdot (l - i)}{l \cdot (l + 1)} \qquad\qquad s_n^{prior} \text{ is a linear weighted MA}$$

$$w_i = w_i^{exp} \quad = \begin{cases} \alpha \cdot (1 - \alpha)^i & : \quad i < n \\ (1 - \alpha)^n & : \quad i = n \end{cases} \qquad s_n^{prior} \text{ is an exponentially weighted MA}$$

The weighting functions w_i listed above are not suited for the central moving average. In this case, so-called *window functions* are used, which are symmetric to $i = 0$, e.g. cosine-, triangular-, Hamming-, Hann-, or Gauss-windows.

To save computing time a recursive representation (including suitable initial values) of the algorithms of practical interest is desirable. Therefore, in the case of the moving arithmetic mean with $w = l^{-1}$, s_n^{prior} can be written as

$$s_n = s_{n-1} + w \cdot (v_n - v_{n-l}) \tag{3.25}$$

and is shown in figure 3.14. Equation (3.25) is also true for the unweighted moving sum with $w = 1$. While the linear weighted MA has no recursive expression, one can show that

the recursive exponential weighted MA is identical to the recursive integrator algorithm in equation (3.24) with $\alpha = 1 - \tau/(\tau + \Delta t)$. The response of these MA filters is similar to that of the high-pass filter: It reduces the amplitude of periodic signals with a period T shorter than the filter duration $l \cdot \Delta t$ and smoothes noisy signals.
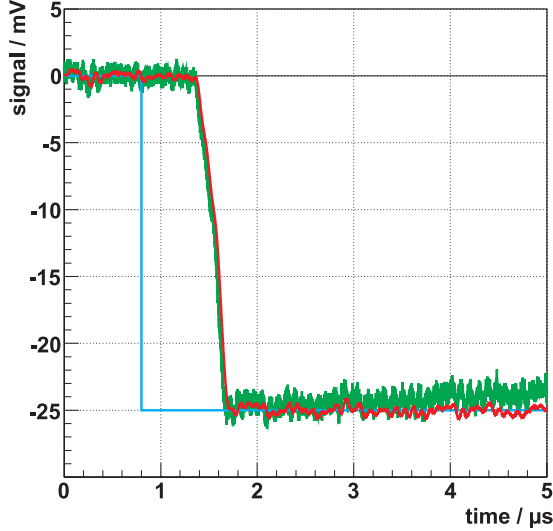
Figure 3.11: Digitized, offset-corrected HPGe preamplifier signal (green line), its smoothed MWD response u_n (red line) and the step function h_n from equation (3.22) (blue line). $\Delta t = 0.5$ ns.
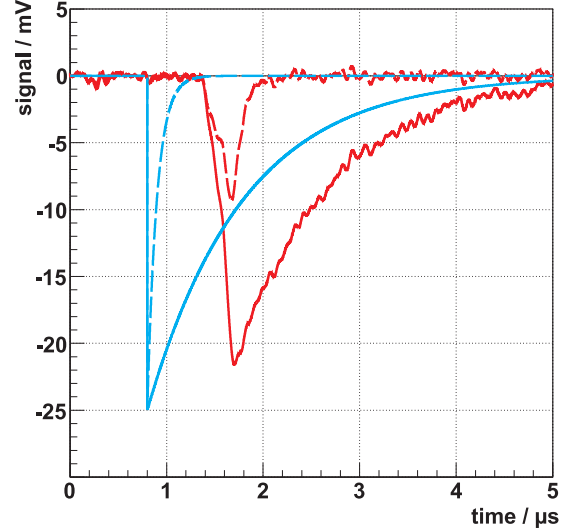
Figure 3.12: Responses of the high-pass filter from equation (3.23) to u_n (blue lines, smoothed) and to h_n (red lines) with $\tau = 0.1\,\mu$s (dashed lines) and $\tau = 1\,\mu$s (solid lines). $\Delta t = 0.5$ ns.
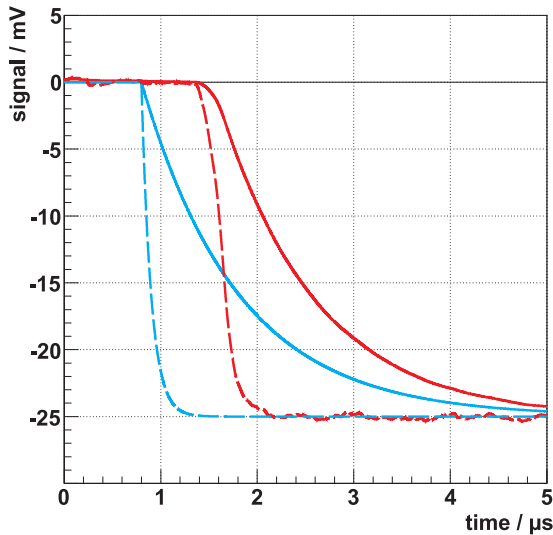
Figure 3.13: Responses of the low-pass filter from equation (3.24) to u_n (blue lines) and to h_n (red lines) with $\tau = 0.1\,\mu$s (dashed lines) and $\tau = 1\,\mu$s (solid lines). $\Delta t = 0.5$ ns.
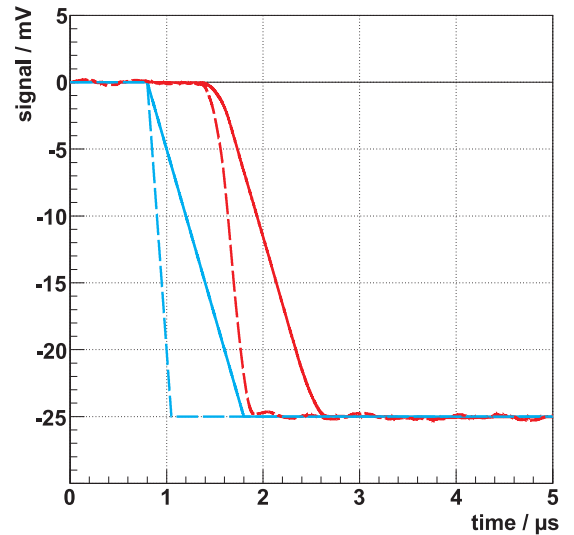
Figure 3.14: Responses of the MA filter from equation (3.25) with $w = l^{-1}$ to u_n (blue lines) and to h_n (red lines), with $l = 500$ (dashed lines) and $l = 2000$ data points (solid lines). $\Delta t = 0.5$ ns.

3.2.3   Shaper

Gaussian Shaper (CR-$(\mathrm{RC})^n$ Shaper)

The result of a high-pass filter, described by equation (3.23), is already very well suited to eliminate tails of preamplifier signals, which have relative long time constants of about $100\,\mu\mathrm{s}$. However, the sharply pointed top makes a precise determination of the amplitude difficult and in addition fast fluctuations passing the filter can worsen the accuracy of this measurement, too. To overcome these drawbacks, one could take advantage of the low-pass filter, described by equation (3.24). By applying n sequent stages of the low-pass filter after one high-pass filter — all of them with the same time constant τ — a Gaussian-like or CR-$(\mathrm{RC})^n$ shaper is obtained. The *peaking time*, i.e. the time value with the maximum amplitude, is given by $\tau_p = n \cdot \tau$, the normalization factor is given by $N = n! \cdot e^n/n^n$. While CR-RC shaping ($n = 1$), shown in figure 3.15, results in a clear asymmetric shape, the deviations to a Gaussian curve become negligible for $n = 4$, which is shown in figure 3.16.

Triangular and Trapezoidal Shaper

With the method of *digital synthesis* by JORDANOV and KNOLL [25], it is not only possible to correct the ballistic deficit but also to implement several shapers. Trapezoidal shaping shown in figure 3.17 can be realized with the recursion formula

$$s_n = s_{n-1} + N \cdot (v_n - v_{n-k} - v_{n-k-m} + v_{n-2 \cdot k - m}) \tag{3.26}$$

where k is the slope length, m is the plateau length and $N = 1/k$ is the normalization factor. For $m = 0$ the trapezoidal shaper becomes a triangular shaper. Choosing $k = 1$ will result in a rectangular shape.

Cusp-like and Truncated Cusp-like Shaper

The cusp-like shaping is similar to the triangular shaping, but with slopes rising or falling faster than linear slopes, which is indicated in figure 3.18 and expressed recursively by

$$\begin{aligned} p_n &= p_{n-1} + v_n - v_{n-2 \cdot k - 1} \\ s_n &= s_{n-1} + N \cdot [p_n - (2 \cdot k + 1) \cdot v_{n-k}] \quad . \end{aligned} \tag{3.27}$$

Having slopes as cusp-like shapers but a plateau in between the truncated cusp-like shaper is being described in the recursion formula

$$\begin{aligned} p_n &= p_{n-1} + v_n - v_{n-k} + v_{n-k-m} - v_{n-2 \cdot k - m} \\ s_n &= s_{n-1} + N \cdot [p_n - k \cdot (v_{n-k} + v_{n-k-m}) - v_{n-k-m} + v_{n-2 \cdot k - m}] \quad . \end{aligned} \tag{3.28}$$

The parameters of both shapers are the slope length k, the plateau length m and the normalization factor $N = 2/(k^2 + k)$.
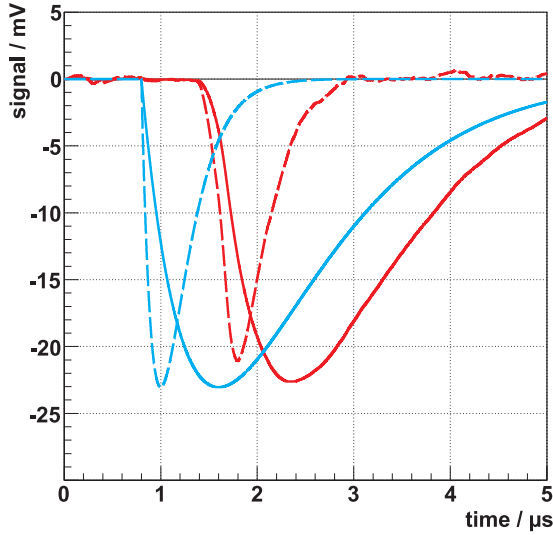
Figure 3.15: Responses of the CR-RC shaper from equations (3.23) and (3.24) to u_n (blue lines) and to h_n (red lines), with $\tau = 200\,\text{ns}$ (dashed lines) and $\tau = 800\,\text{ns}$ (solid lines). $\Delta t = 0.5\,\text{ns}$.
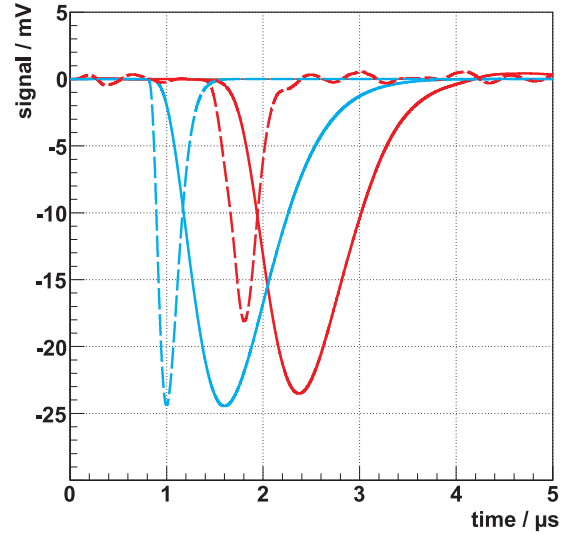
Figure 3.16: Responses of the Gaussian or CR-$(\text{RC})^4$ shaper from equations (3.23) and (3.24) to u_n (blue lines) and to h_n (red lines), with $\tau = 50\,\text{ns}$ (dashed lines) and $\tau = 200\,\text{ns}$ (solid lines). $\Delta t = 0.5\,\text{ns}$.
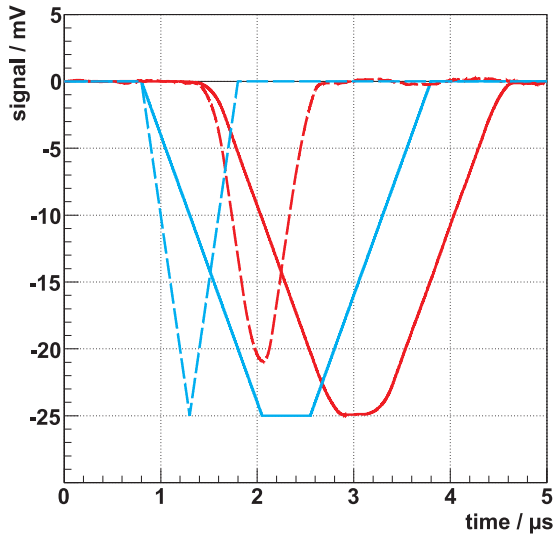
Figure 3.17: Responses of the triangular shaper with $k = 1000$ (dashed lines) and the trapezoidal shaper both from equation (3.26) with $k = 2500$, $m = 1000$ (solid lines) to u_n (blue lines) and to h_n (red lines). $\Delta t = 0.5\,\text{ns}$.
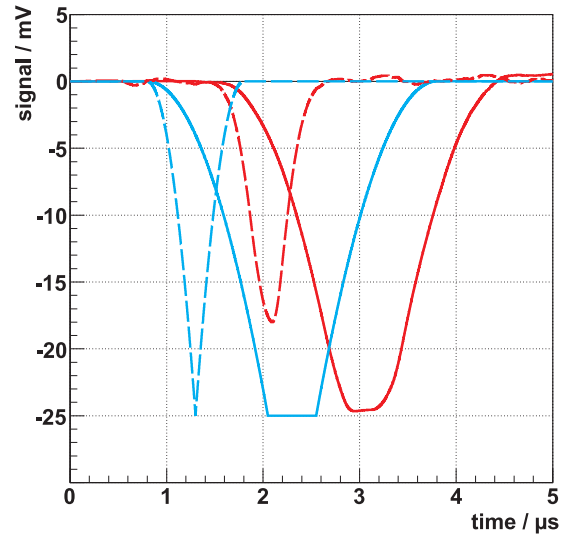
Figure 3.18: Responses of the cusp-like shaper from equation (3.27) with $k = 1000$ (dashed lines) and the truncated cusp-like shaper from equation (3.28) with $k = 2500$, $m = 1000$ (solid lines) to u_n (blue lines) and to h_n (red lines). $\Delta t = 0.5\,\text{ns}$.

3.3 Measurements with an HPGe Detector and a ^{22}Na Source

One of the HPGe detectors, which are usually used in the photon scattering experiments introduced in section 1.2, is set up together with two BaF$_2$ scintillation detectors from the nELBE experiment as shown in figure 3.19. The *ORTEC GMX-100* [26] used here is a coaxial n-type HPGe detector with a crystal length of 90.0 mm and a diameter of 79.1 mm. This detector has a relative efficiency of 105 % and an operating bias voltage of -4500 V. The HPGe crystal is surrounded by eight BGO scintillation crystals to detect escaping photons. The whole detector system is surrounded by a 2 cm thick lead shielding. The BGO shield does not cover the end cap of the HPGe crystal. There, a 10 cm thick lead collimator with a conical aperture centered around the end cap is mounted. Figure 1.2 shows a radiation source mounted in this aperture. The radiation to detect in this experiment is emitted from an encapsulated ^{22}Na source. ^{22}Na decays by electron capture (branching ratio: 9.5 %) and β^+ decay (90.5 %) with a half-life of 2.6 years to an excited state of the stable ^{22}Ne. This excited state decays state by emitting a photon with the energy $E_\gamma = 1274.53$ keV [27]. The positron produced in the β^+ decay is slowed down and annihilates with an electron within the source material. In this annihilation, two photons with the energy $E_\gamma = 511$ keV each are emitted. In both cases mono-energetic γ-rays are emitted which are well suited to determine the resolution of detectors in high-resolution γ-ray spectroscopy. The annihilation quanta are subject to DOPPLER-broadening so the peak at 511 keV will be wider than a "regular" γ-peak. The BaF$_2$ detectors are supposed to detect the photons in coincidence with the HPGe detector, however this coincidence is not analyzed in this experiment.
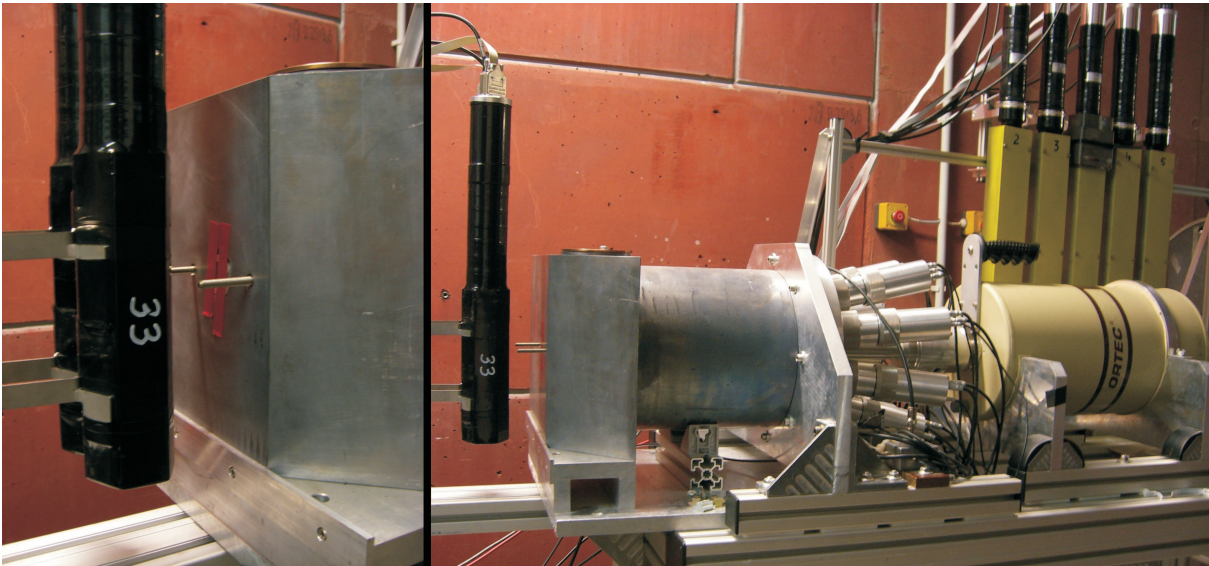
Figure 3.19: Setup of an HPGe detector and two BaF$_2$ detectors in the measurement with the ^{22}Na source. The picture shows in the left the radiation source mounted in the aperture of the lead collimator with red stripes of adhesive tape. The right half of the picture shows (from left to right) the BaF$_2$ detectors, the shielding lead block, the shielded germanium crystal, the PMs of the BGO crystals and the dewar filled with liquid nitrogen.
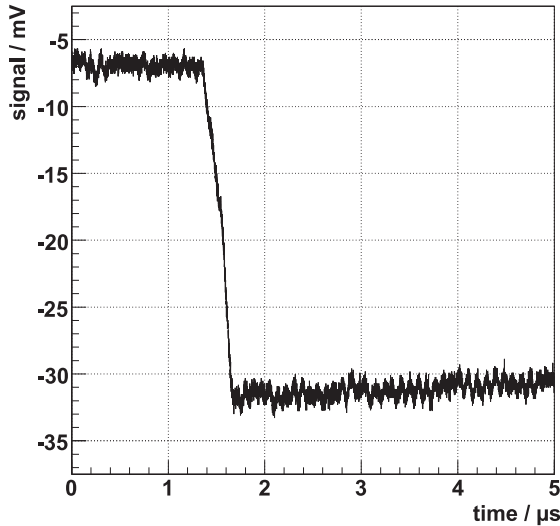
Figure 3.20: Digitized preamplifier signal of the HPGe detector. It is the same signal as in figure 3.11.
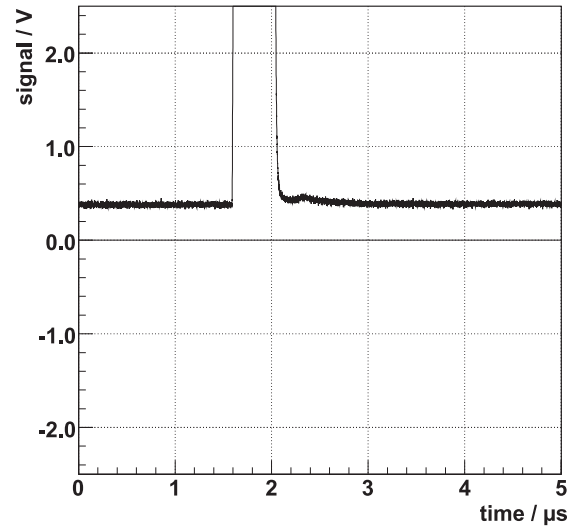
Figure 3.21: Logical signal generated by an analog CFD from the signal in figure 3.20. This signal triggered the nELBE FDDAS during the experiment.

The nELBE FDDAS was equipped with one Acqiris DC-282 digitizing card and the VMETRO recording card in this experiment. In preparation of the data acquisition two problems were observed. The first problem was to configure the trigger conditions of the FDDAS. The intention was to trigger on the preamplifier signal of the HPGe detector only and acquire it together with the two BaF$_2$ signals and a veto signal of the BGO detectors. Since it is not possible to disable the triggers of the other channels, their trigger thresholds were set to values which are usually not reached. Anyhow, the FDDAS did not acquire data in this configuration[2]. After tests with several trigger configurations, one suitable configuration was found that triggered on a positive signal. A logical signal (TTL standard) was generated by an analog constant-fraction discriminator from the HPGe preamplifier signal and used to trigger the FDDAS. The trigger thresholds of the negative HPGe preamplifier signal and the negative BaF$_2$ signals were set to a positive value. In figure 3.20 one of the preamplifier signals is shown while figure 3.21 shows the corresponding logical signal. In this configuration, signals were sampled with $N = 10$ bits for 5 µs at a sampling rate $f_S = 2$ GS/s, i.e. the sampling interval was $\Delta t = 0.5$ ns, resulting in 10000 data points per channel per event. The pre-trigger-delay, i.e. the number of data points which are stored before the trigger point was set to 3200 in order to determine the baseline of the signal. The HPGe preamplifier signal was acquired in the range from -100 mV to 0 mV while the trigger threshold was set to -2 mV. Due to the offset this value is not realized for any signal. The logical signal was acquired in the range from -2500 mV to 2500 mV and triggered the FDDAS after the threshold at 2400 mV was crossed with a positive slope.

The second problem was that at a random time after the acquisition started all preamplifier signals showed an offset in the order of 100 mV and therefore left the predefined voltage range of the digitizer. This happened suddenly and can not be explained by a saturation of the preamplifier due to high count rates. After the acquisition was stopped

---

[2]Later it turned out, that there are constraints for the trigger levels.

and the next acquisition was started, the signals had returned to their usual baseline. This strange behavior of preamplifier and digitizer is not yet understood. As a consequence of this, data was acquired in nine subsequent runs with each 3600 events in order to keep the number of events affected by this problem small. In total 2700 MiB or 32400 events were digitized, 22109 of those events do not have this problem.

For comparison also the energy resolution of the HPGe detector was measured with the state of the art signal-processing and data-acquisition system of the photon-scattering experiments at ELBE. The preamplifier signal was shaped by an *ORTEC 671 spectroscopy amplifier* [28] and the pulse height was determined by the 14-bit peak-sensing ADC *SILENA 7423* [29]. The shaping time-constant was optimized in order to achieve the best possible energy resolution. The ADC was controlled and read out by a fast ADC-controller [30] which routed the ADC value to higher channels within the final spectrum if there was a veto signal of the BGO detectors. The results of this measurement are discussed in the next section.

3.4   Energy Resolution of the HPGe Detector

3.4.1   Analogously Processed Data

The pulse height spectrum of the analogously processed signals is shown in figure 3.22. The pulse height is given in ADC channels, which are in the range from from 0 to $2^{14} = 16348$. All pulse heights are below channel 5200. The mean values k_{511} and k_{1275} of the peaks at 511.00 keV and 1274.53 keV are used to perform an energy calibration. The energy is

$$
\begin{aligned}
E(k) &= m \cdot k + n &&(3.29)\\
\text{with}\quad m &= \frac{(1274.53 - 511.00)\,\text{keV}}{k_{1275} - k_{511}} \quad \text{and}\quad n = 511.00\,\text{keV} - m \cdot k_{511} \quad,
\end{aligned}
$$

whereas k is the quantity of the pulse height measurement (e.g. voltage or channel number). The full width at half maximum of the peaks is calculated by $FWHM = m \cdot \sigma \cdot 2\sqrt{2\ln 2}$. For this spectrum the calibration parameters are $m = 0.5295$ keV/channel and $n = -34.38$ keV, so the dynamic range of the ADC is $m \cdot 2^{14} \approx 8660$ keV. The energy scale is shown in the upper part of figure 3.22. Apart from the two peaks coming from the ^{22}Na source, three other peaks from the natural occurring background radiation are visible.

The mean values of the peaks are determined by a fit with an asymmetric gaussian function, which is implemented in the analysis program. The parameters of this fit function defined in appendix B.5 are the area A, the mean value k and the standard deviation σ of the symmetric part, the asymmetric area A_{as} (relative to A) and an asymmetry parameter λ. The peaks at 511.00 keV and 1274.53 keV are shown in figures 3.23 and 3.24 together with the asymmetric gaussian function. For comparison a normal gaussian function is fitted to the data, too. As one can see, the value χ^2 becomes significantly smaller for the asymmetric function and also the standard deviations improve a little bit. The energy resolutions (FWHM) are 3.46 keV at 511.00 keV and 2.88 keV at 1275.53 keV.
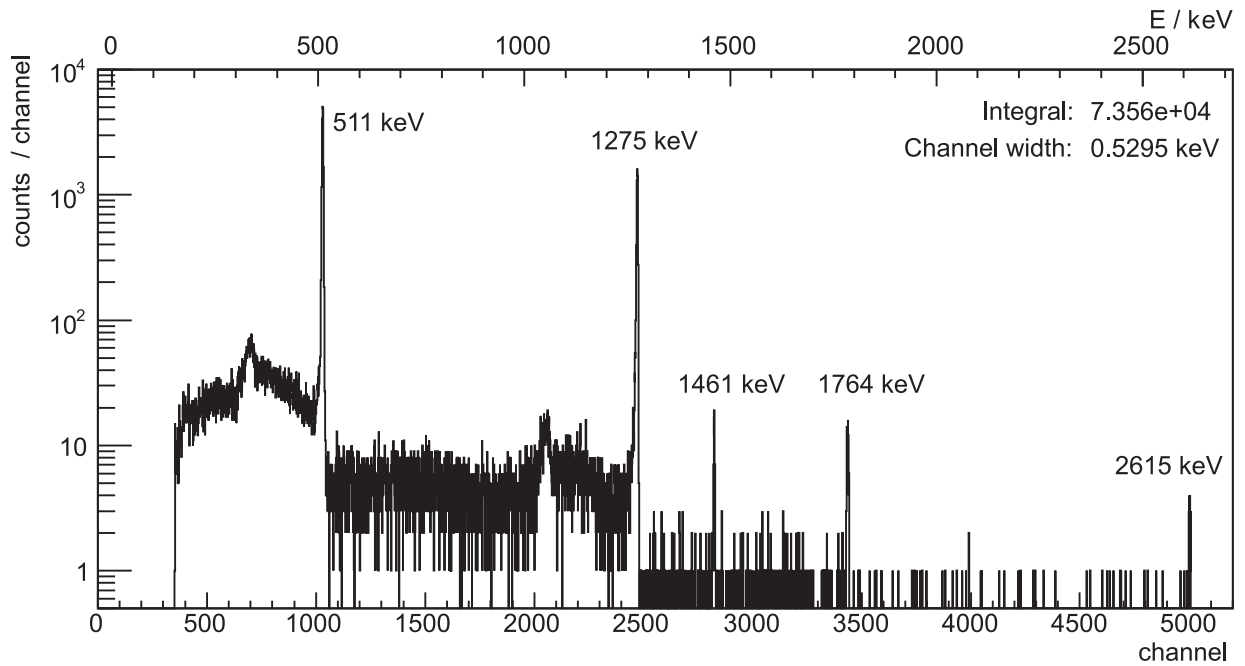
Figure 3.22: Spectrum of the pulse heights of analogously processed preamplifier signals of the HPGe detector. The pulse heights are digitized with a 14-bit peak-sensing ADC with 16384 channels. The peaks at 511 keV and 1275 keV stem from a ^{22}Na source and are used for the energy calibration. The other peaks stem from naturally occurring background radiation of the isotopes ^{40}K, ^{214}Bi and ^{208}Tl (from left to right).
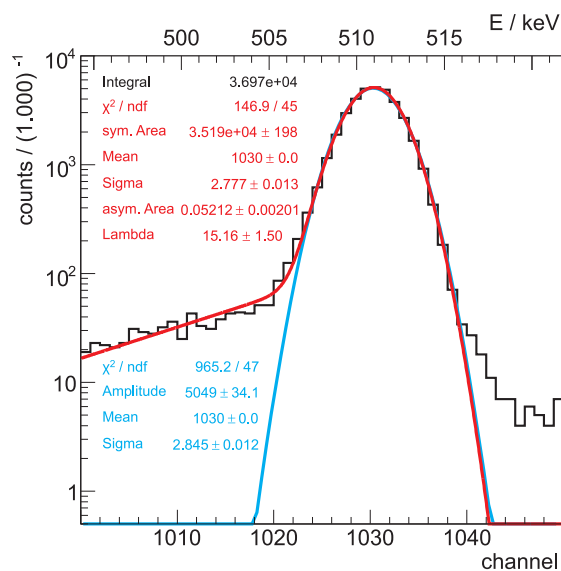
Figure 3.23: Peak in the ASP pulse height spectrum at $E = 511.00$ keV fitted with a gaussian (blue line) and an asymmetric gaussian function (red line). With the latter the energy resolution (FWHM) is 3.46 keV.
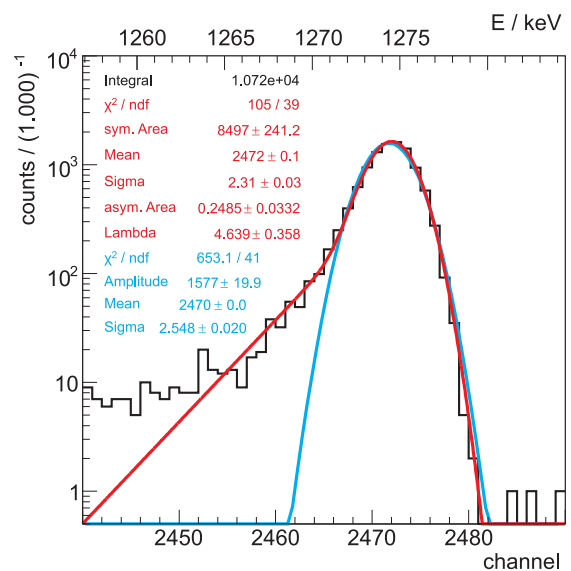
Figure 3.24: Peak in the ASP pulse height spectrum at $E = 1274.53$ keV fitted with a gaussian (blue line) and an asymmetric gaussian function (red line). With the latter the energy resolution (FWHM) is 2.88 keV.
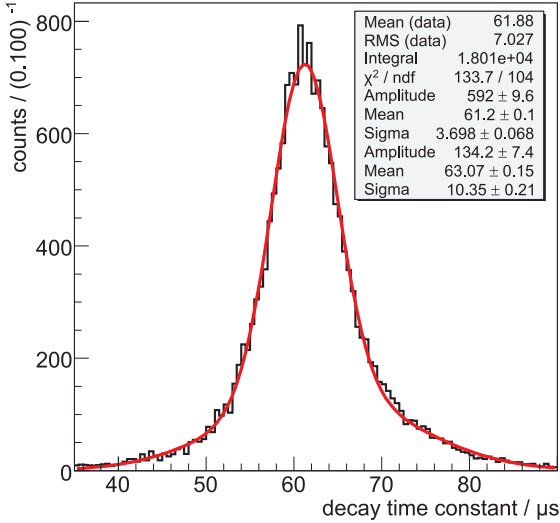
Figure 3.25: Histogram of the preamplifier decay time constant determined from the digitized signals. See text for details.
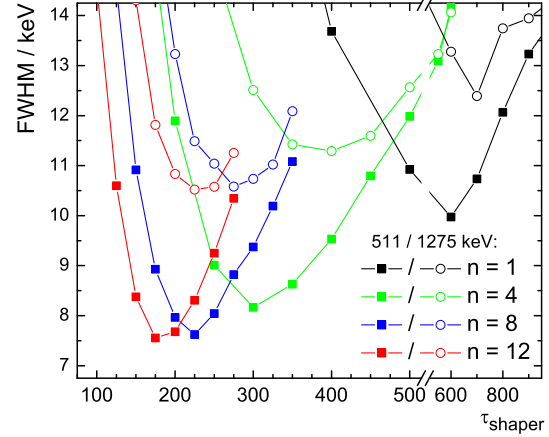
Figure 3.26: Energy resolutions (FWHM) achieved with CR-$(RC)^n$ shaping. Note the change of the time-constant scale.
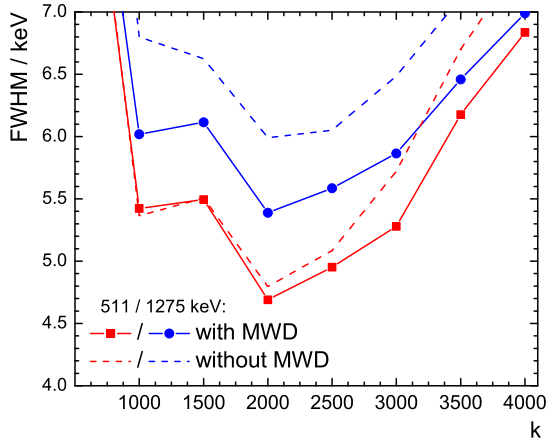
Figure 3.27: Energy resolutions (FWHM) achieved with trapezoidal shaping with the plateau length $m = 1000$ with and without MWD.
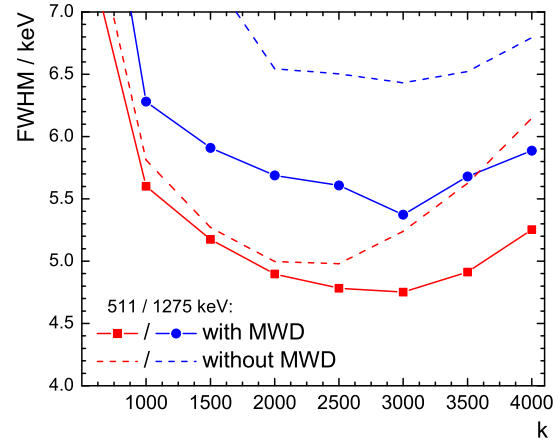
Figure 3.28: Energy resolutions (FWHM) achieved with truncated cusp-like shaping with the plateau length $m = 1500$ with and without MWD.

3.4.2 Digitally Processed Data

The algorithms described in section 3.2 are applied to digitized preamplifier signals of the HPGe detector, which were acquired in the experiment in section 3.3. The baseline of the signals is between $-6.8\,\text{mV}$ and $-7.8\,\text{mV}$. This offset is determined by averaging the baseline and then subtracted from the signal in order to suppress the response of the applied algorithms to the step at $t = 0$. Then the moving window deconvolution is applied with a length m_{MWD} longer than the number of sampled data points (here: 10000 data points) in order to convert the preamplifier signal to a step signal which is then shaped by a CR-$(RC)^n$, trapezoidal or truncated cusp-like shaper. Thereby, the application of MWD with $m_{MWD} = 10000$ followed by trapezoidal shaping with the slope length k and the plateau length m_{shaper} is equivalent to the application of MWD with $m_{MWD} = k + m_{shaper}$ followed by the MA filter from equation (3.25) with the length $l = k$. Finally, the pulse

height of the shaped signals is determined and filled into histograms. The energy calibration and the determination of the FWHM is done in the same way as for the analog data.

One parameter of the MWD algorithm is the decay time constant τ_{decay} of the preamplifier, which is here determined from the signals. Therefore, the exponential decaying tail of each signal is fitted with the function

$$f(t) = p_1 \cdot e^{-t/p_2} \tag{3.30}$$

with the time t and the parameters p_1 and p_2. Then the values of p_2 are filled into a histogram, whereas each value is weighted with its relative error from the fit. This histogram is shown in figure 3.25 and gives a mean value $\tau_{decay} = 61.58\,\mu s$ for the MWD. The sampling interval $\Delta t = 0.5\,ns$ is given to the MWD algorithm as the other parameter.

The CR-$(RC)^n$-shaper is applied to the output signal of the MWD with different parameters n (number of integrations) and τ_{shaper} (time constant of differentiator and integrator). For the cases $n = 1$, $n = 4$, $n = 8$ and $n = 12$ the FWHM is shown as a function of τ_{shaper} in figure 3.26. There one can see that for each curve the FWHM has a minimum, which decreases for increasing n. The best results here are FWHM of 7.55 keV at 511.00 keV and 10.52 keV at 1275.53 keV for $n = 12$. In the application of the trapezoidal and truncated cusp-like shaper to the MWD output signal, the plateau length m is varied between 500 and 3000 points and the slope length k is varied between 500 and 4000 points. For the trapezoidal shaper the best result are FWHM of 4.69 keV at 511.00 keV and 5.39 keV at 1275.53 keV for $m = 1000$ and $k = 2000$ and for the truncated cusp-like shaper the best result are FWHM of 4.75 keV at 511.00 keV and 5.37 keV at 1275.53 keV for $m = 1500$ and $k = 3000$. Although these results are very close to each other, the truncated cusp-like shaper has the better results over a wide range of k. Figures 3.27 and 3.28 show the best results as a function of k. Furthermore, the FWHM achieved with this shapers in this configuration but without the MWD are shown there. As one can see this makes a significant difference especially for the higher energy of 1275.53 keV. Tests with $m = 0$ (i.e. triangular and cusp-like shaper) are performed, too, but do not result in competitive energy resolutions. The results of all measurements are summarized in table 3.1 for CR-$(RC)^n$-shaping and in table 3.2 for all other shapers.

In figure 3.29 the pulse height spectrum of the signals processed with the truncated cusp-like shaper with $m = 1500$ and $k = 3000$ is shown. The energy calibration is performed with equation (3.29) and the two peaks shown in figures 3.30 and 3.31 are fitted with the asymmetric gaussian function. The calibration parameters are $m = 20.41$ keV/mV and $n = 1.23$, so the dynamic range is $m \cdot 100\,mV = 2041$ keV.

In section 2.1 the concept of the *Peak-Sensing Equivalent Number Of Bits (PSENOB)* is introduced. The truncated cusp-like shaper used here is nearly equivalent to the shaper "Trapezoidal 2" in table 1 of reference [10]. With $\vartheta = k \cdot \Delta t = 1.5\,\mu s$, $k_{G\star} = 1.225$ and an $ENOB$ given between 5.4 and 7.2 the PSENOB calculated with equation (2.1) is between 10.4 and 12.2. In comparison to the analogously processed data one finds that digital methods applied to signals digitized with the nELBE FDDAS can reduce the problem of the ballistic deficit, but the energy resolution achieved with this 10-bit digitizer system is worse than with the 14-bit ADC by a factor of two.
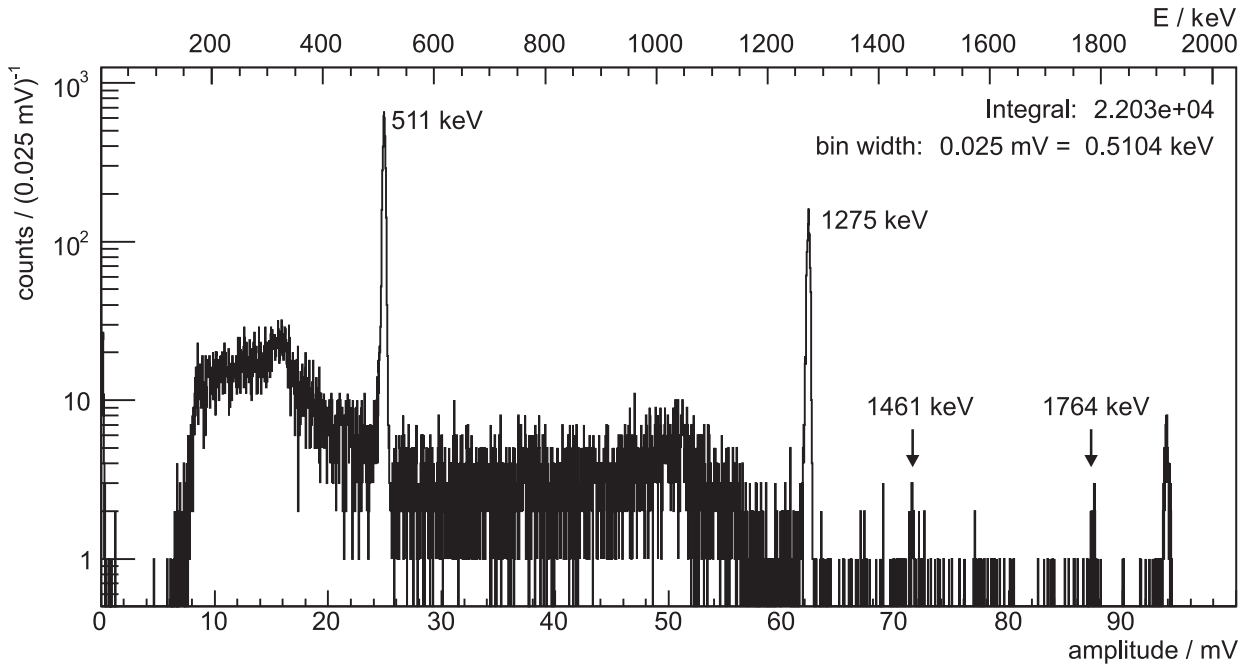
Figure 3.29: Spectrum of the pulse heights of digitally processed preamplifier signals of the HPGe detector. The signals are processed with the MWD to correct the ballistic deficit and shaped with the truncated cusp-like shaper with $m = 1500$ and $k = 3000$. The labeled peaks are described in figure 3.22. The peak at 94 mV does not stem from radiation, but contains all signals leaving the voltage range of the digitizer.
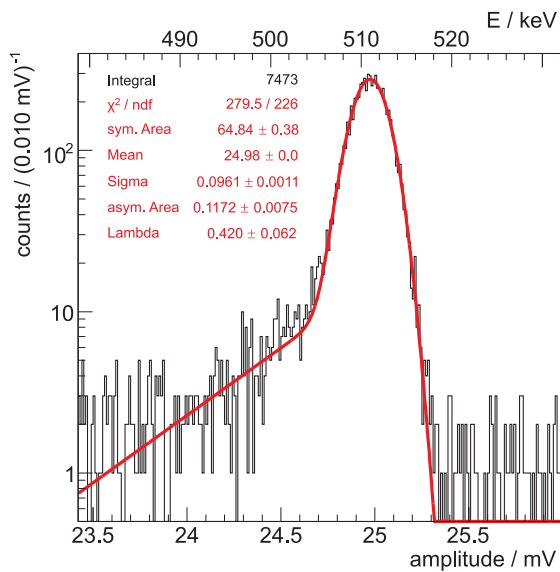
Figure 3.30: Peak in the DSP pulse height spectrum at $E = 511.00$ keV fitted with an asymmetric gaussian function. The energy resolution (FWHM) of this peak is 4.75 keV.
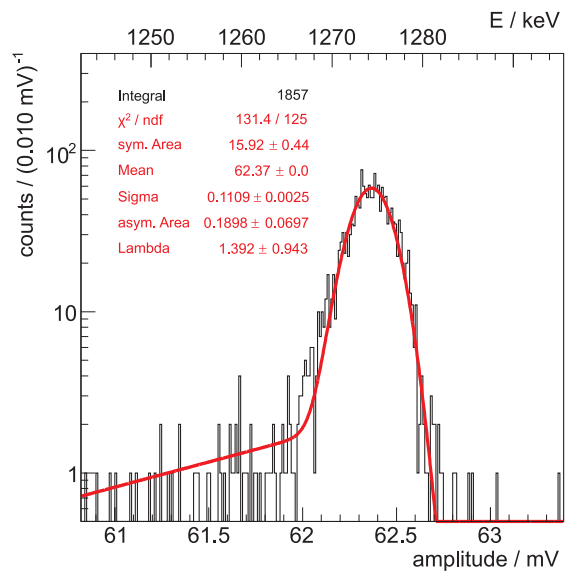
Figure 3.31: Peak in the DSP pulse height spectrum at $E = 1274.53$ keV fitted with an asymmetric gaussian function. The energy resolution (FWHM) of this peak is 5.37 keV.

n=1			n=4			n=8			n=12		
τ/ns	511	1275	τ/ns	511	1275	τ/ns	511	1275	τ/ns	511	1275
200	36.07	76.96	100	36.39	71.68	75	33.16	91.00	50	40.38	103.37
300	20.09	35.82	150	17.97	27.68	100	19.98	39.65	75	22.90	40.95
400	13.68	20.99	200	11.89	20.97	125	14.57	26.65	100	14.57	28.02
500	10.92	15.00	250	9.01	15.03	150	10.91	19.76	125	10.60	18.88
600	9.97	13.28	300	8.17	12.51	175	8.93	15.87	150	8.38	14.31
700	10.74	12.39	350	8.63	11.42	200	7.96	13.23	175	7.55	11.81
800	12.06	13.74	400	9.53	11.29	225	7.62	11.49	200	7.68	10.84
900	13.23	13.95	450	10.80	11.59	250	8.04	11.04	225	8.31	10.52
1000	13.95	14.34	500	11.99	12.57	275	8.82	10.58	250	9.25	10.58
1100	13.96	15.17	550	13.09	13.23	300	9.38	10.74	275	10.34	11.25
1200	14.43	15.70	600	14.17	14.07	325	10.19	11.02	300	13.45	23.69
						350	11.08	12.09			

Table 3.1: Energy resolutions (FWHM) / keV achieved with CR-$(RC)^n$ shaping for different shaping time-constants τ.

	trapezoidal		trunc. cusp		trapezoidal		trunc. cusp	
k	511	1275	511	1275	511	1275	511	1275
	$m = 500$				$m = 1000$			
500	10.98	12.99	13.29	21.63	9.45	9.82	10.40	12.60
1000	6.09	8.88	7.77	13.18	5.42	6.02	6.97	7.76
1500	5.91	7.32	6.23	9.36	5.49	6.11	5.81	6.46
2000	4.79	7.07	5.35	8.22	4.69	5.39	5.31	5.91
2500	5.44	6.22	6.03	7.45	4.95	5.59	5.01	5.60
3000	5.47	6.63	4.73	6.89	5.28	5.86	4.94	5.63
3500	6.11	7.29	4.76	6.54	6.18	6.46	4.95	5.58
4000	6.68	7.51	5.21	6.73	6.84	6.99	5.01	5.45
4500							5.45	6.06
5000							5.83	6.17
	$m = 1500$				$m = 2000$			
500	6.30	7.03	7.70	9.36	8.49	8.71	8.52	9.39
1000	5.30	5.95	5.60	6.28	5.24	5.80	6.34	6.97
1500	4.91	5.73	5.18	5.91	5.35	6.14	5.54	6.08
2000	4.77	5.47	4.90	5.69	5.15	5.83	5.21	5.85
2500	5.02	5.68	4.78	5.61	5.71	6.28	5.09	5.68
3000	5.54	6.23	4.75	5.37	6.11	6.59	5.26	5.83
3500	6.48	6.65	4.91	5.68	7.01	7.21	5.50	6.01
4000	7.22	7.18	5.25	5.89	7.80	7.79	5.84	6.68
	$m = 2500$				$m = 3000$			
500	6.33	6.60	7.78	8.37	8.34	8.82	8.20	9.02
1000	5.17	5.93	5.47	6.14	5.72	6.40	6.53	7.20
1500	5.34	5.91	5.12	5.83	6.14	6.77	5.95	6.71
2000	5.55	6.35	5.12	5.79	6.18	6.52	6.05	6.81
2500	6.01	6.62	5.22	5.97	6.61	7.20	6.04	6.90
3000	6.58	7.05	5.49	6.29	7.16	7.34	6.26	6.95
3500	7.52	7.88	5.83	6.47	8.30	8.09	6.57	7.02
4000	8.49	8.15	6.19	6.61	8.73	8.94	5.42	5.68

| | $(m = 0)$ | | | | $m = 1000$ | | $m = 1500$ | |
	triangular		cusp-like		trapezoidal*		trunc. cusp*	
k	511	1275	511	1275	511	1275	511	1275
500					9.61	11.37	8.08	12.65
1000					5.36	6.80	5.81	8.67
1500	27.19	66.58			5.51	6.63	5.27	7.30
2000	19.94	37.10			4.80	5.99	5.00	6.54
2500	17.16	39.27	30.05	103.18	5.08	6.05	4.98	6.50
3000	14.24	27.56	24.57	50.30	5.72	6.49	5.24	6.43
3500	12.99	26.24	21.90	50.53	6.70	7.11	5.62	6.52
4000	12.15	23.70	19.52	45.55	7.45	7.62	6.15	6.79
4500	11.67	20.86	18.04	48.23				
5000	11.46	19.52	16.38	37.00		* without MWD		
5500	11.31	18.12	15.79	32.53				
6000	11.26	17.32	14.72	30.11				

Table 3.2: Energy resolutions (FWHM) / keV achieved with trapezoidal and truncated cusp-like (trunc. cusp) shaping for different plateau lengths m and slope lengths k. For $m = 0$ this is equivalent to triangular or cusp-like shaping.

Chapter 4

Time Resolution of Scintillation Detectors

4.1 Scintillation Detectors

Scintillations are light flashes induced by ionizing radiation in certain materials. The origin of the luminescence is either a transition in the electronic band structure of materials with a crystal lattice (inorganic scintillators) or a transition in the energy level structure of a single molecule (organic scintillators). The photons emitted at these transitions are then detected by photomultiplier tubes (PMT) or photodiodes. This concept of radiation detection is applied in wide range of experiments with several different materials. Principles and applications of scintillation detectors are well described in textbooks [1, 31].

The detectors used at nELBE are plastic scintillators for neutron detection and barium fluoride (BaF_2) scintillators for photon detection. The plastic scintillators are made from the organic material *EJ-200* [32], which has a scintillation-light decay time of 2.1 ns. The dimensions of one scintillator are $1000 \times 42 \times 11\,mm^3$. At both ends of the 1000 mm long sides, the scintillator is readout by one photomultiplier tube each. Barium fluoride is an inorganic scintillator with two scintillation light components. The slow component has a decay time of $\approx 630\,ns$ and is emitted in a band centered at 310 nm. The fast component has a decay time of 0.6 ns – 0.8 ns and is emitted in bands centered at 195 nm and 220 nm. The intensity of slow component is depending on the primary ionization density and therefore it is possible to discriminate particles by their pulse shape. The crystals used here are 19 cm long and have a hexagonal cross section with an inner diameter of 53 mm. Each crystal is read out by one PMT. The PMTs used for both detector types are *Hamamatsu R2059-01* 2-inch photomultiplier tubes [33] with the active high-voltage divider socket *iseg PHQ2059* [34]. They are used at a gain of about $2 \cdot 10^7$. The tubes have a short rise time of 1.3 ns and a low transit-time spread of 0.55 ns. To be sensitive to the ultraviolet (UV) scintillation light of the fast component of BaF_2, the PMTs have a fused silica window.

4.2 Algorithms for Timing Measurements

The moment of an interaction in the detector has often to be derived with high accuracy from a detector signal. Fluctuations of the timing signal can be a result of varying pulse appearance (i.e. different amplitude, rise time, shape) or of appearance-independent

effects (e.g. noise) and are called *walk* or *jitter*. In analog signal processing there are several common methods [1, 2] to determine a precise time from detector signals. These methods can be adapted in digital signal processing, where the challenge is to achieve time signals of the same precision, although a big part of the information about the detector signal was lost in the digitizing process. Especially for signals with short rise times one has to close the gaps, that are of the width of the sampling interval Δt, between the sampled data points by interpolation or by fitting.

4.2.1 Digital Counterparts of Analog Methods

Leading Edge Timing

The sampled data points v_n are investigated point by point until the signal crosses a fixed threshold v_{th} and a slope condition (rising or falling) is fulfilled. Between the points v_i and v_{i+1}, which enclose the threshold, the signal is interpolated linearly, resulting in

$$t_{th} = \left(i + \frac{v_{th} - v_i}{v_{i+1} - v_i} \right) \cdot \Delta t \quad . \tag{4.1}$$

This method is called leading edge timing (LET), although it is also possible to determine a time signal from the trailing edge of a signal. It should be mentioned that a linear interpolation can strongly differ from the original curve shape particularly near the peak or the baseline of the signal and that LET is sensitive to the walk effect mentioned above. In figure 4.1, the two signals A and B are of identical shape but have different amplitudes and thus generate two different time signals t'_A and t_B, if LET is applied with a threshold of $v_{th} \approx 0.67\,\mathrm{V}$ in this example.

Extrapolated Leading Edge Timing

Using two different threshold values v_{th1} and v_{th2} in equation (4.1) one gets the time values t_{th1} and t_{th2} which lie upon a line that crosses the pulse's baseline v_{bl} at

$$t_{bl} = t_{th1} + \frac{v_{bl} - v_{th1}}{v_{th2} - v_{th1}} \cdot (t_{th2} - t_{th1}) \quad . \tag{4.2}$$

The second threshold value of this extrapolated leading edge timing (ELET) method can be parametrized with $v_{th2} = f_{th} \cdot v_{th1}$, where $f_{th} > 1$ is a stretch factor.

Zero-Crossing Shaper Timing

By applying the low-pass (CR) and the high-pass filter (RC) from equations (3.23) and (3.24) in the order CR-RC-CR to the detector signal, the zero crossing time t_{zc} of the output signal is theoretically independent of the amplitude of the detector signal. t_{zc} is determined by interpolating between the two surrounding data points. The correct zero-crossing is usually the only zero-crossing between the maximum and the minimum of the output signal and can be discriminated from random, noise-induced zero-crossings. While in ASP this zero-crossing shaper timing (ZCT) method will introduce more noise to the signal and contribute to the jitter, this is not the case in DSP. In figure 4.2 the response of the CR-RC-CR shaper to a BaF$_2$ detector signal is shown.
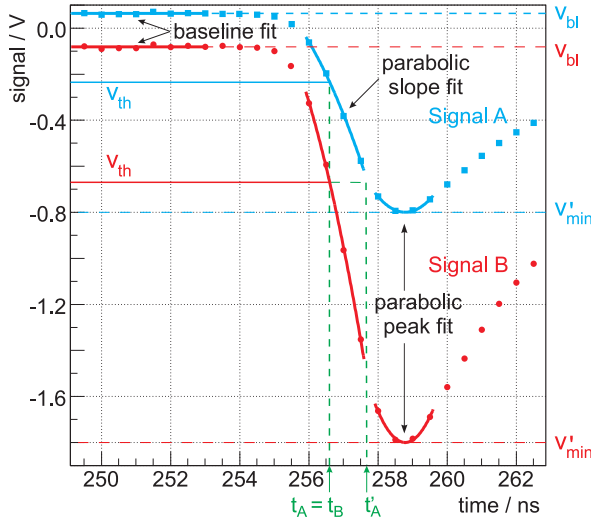
Figure 4.1: Working principle of the LET and the FCFT method. Signal B is an attenuated and shifted copy of the BaF$_2$ detector signal A. See text for details.
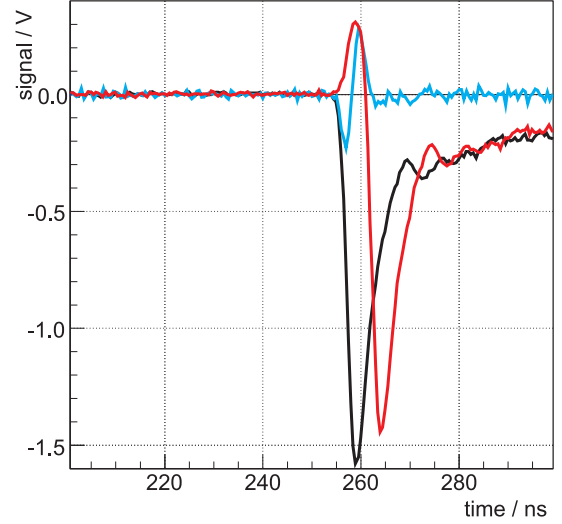
Figure 4.2: Responses of the ZCT with $\tau = 0.2\,\text{ns}$ (blue line, scaled up by a factor of 20) and the ZCCFT method with $a_{cf} = 0.2$ and $t_{cf} = 5\,\text{ns}$ (red line) to a BaF$_2$ detector signal (black line).

Zero-Crossing Constant-Fraction Timing

Figure 4.2 shows the response of the zero-crossing constant-fraction timing (ZCCFT) method to a BaF$_2$ detector signal, too. This method is similar to ZCT but with lower jitter and also free of the amplitude-walk. In ASP the ZCCFT method is realized in the *constant fraction discriminator (CFD)* and is the most common method for precision timing measurements. The working principle is: (a) the detector signal v_n is multiplied with an attenuation factor $0 < a_{cf} < 1$ on the one hand and (b) v_n is inverted and delayed by a time $t_{cf} = m \cdot \Delta t$ shorter than the pulses rise time on the other hand. The sum of (a) and (b) is

$$s_n = a_{cf} \cdot v_n - v_{n-m} \tag{4.3}$$

which has again a zero crossing at t_{zc} which is independent of the amplitude of the detector signal. t_{zc} is determined as described for ZCT. Since t_{zc} is not independent of the rise time of the detector signal there is a related method called *amplitude and rise time compensated (ARC) timing* where t_{cf} is chosen as small as possible to avoid an influence of the rise time variation on t_{zc}.

4.2.2 Fully Digital Methods

Constant Fraction Timing

Constant fraction timing (CFT) can be realized by determining the amplitude and then determining the time where the signal crosses a certain fraction of this amplitude. For the negative signal used here, the determination of v_{min} is followed by leading edge timing with $v_{th} = c_{cf} \cdot v_{min}$. This is not practicable in normal ASP systems whereas in DSP the amplitude can easily be found and the LET method from equation (4.1) allows a different threshold for each detector signal. For small fractions one has to pay attention to signals

of low amplitude, because then v_{th} is close to the baseline and noise can generate the time signal instead of the signal. This effect is compensated by moving backwards on the leading edge point by point, starting at the position of the amplitude v_{min} and determining the threshold-crossing by interpolating between the two surrounding data points.

Fitting Constant Fraction Discriminator

Motivated by results presented by BEČVÁŘ ET AL. [35], the results of CFT can maybe be improved by using fitting methods to determine the amplitude v_{min}, the baseline v_{bl} and the threshold crossing time t_{th} more precisely. The peak region, which is fitted with a parabola $f(x) = ax^2 + bx + c$, consists of the four points

$$
\begin{aligned}
v_{i-2} \;,\; v_{i-1} \;,\; v_i = v_{min} \;,\; v_{i+1} \qquad &:\quad v_{i-1} \geq v_{i+1} \qquad \text{or} \\
v_{i-1} \;,\; v_i = v_{min} \;,\; v_{i+1} \;,\; v_{i+2} \quad &:\quad v_{i-1} < v_{i+1} \qquad .
\end{aligned}
\tag{4.4}
$$

In both cases the vertex of the parabola should be located between the two central points at $t_{vertex} = -b/2a$. The new maximum is $v'_{min} = (4ac - b^2)/4a$.

From the rising slope of the detector signal the data points v_{low} and v_{trig} crossing the thresholds $0.1 \cdot v'_{min}$ and $c_{cf} \cdot v'_{min}$, respectively, are determined. The baseline v_{bl} is calculated by averaging v_n over a certain number l of points beginning $l + 5$ points before the point v_{low}. The neighborhood of v_{trig}, which consists of the four points

$$
v_{i-2} \;,\; v_{i-1} \;,\; v_i = v_{trig} \;,\; v_{i+1} \quad ,
\tag{4.5}
$$

is again fitted with a second-order polynomial. The intersection of this polynomial with the threshold $v_{th} = v_{bl} + c_{cf} \left(v'_{min} - v_{bl} \right)$ is finally the time signal of the fitting constant fraction timing (FCFT) method. In figure 4.1 the whole procedure is illustrated, where the two signals A and B are of identical shape and have different amplitudes but anyhow generate the same time signals $t_A = t_B$.

4.3 Measurements with BaF$_2$ and Plastic Scintillation Detectors at nELBE

A parasitic data acquisition with the nELBE FDDAS was performed during an experiment at the neutron time-of-flight system nELBE which was introduced in section 1.2. In this experiment the ELBE accelerator delivered an electron beam with a beam current of $2\,\mu A$ and a micro-pulse rate of $101.5625\,kHz$, i.e. the electron bunch interval was about $10\,\mu s$. The neutrons generated in the liquid-lead radiator were used to measure the cross section of the inelastic scattering reaction $^{56}Fe(n,n'\gamma)^{56}Fe$. Therefore, a target of $40\,g$ of elemental iron consisting of $91.754\,\%$ of the isotope ^{56}Fe was installed in the center of the BaF$_2$ array as shown in figure 1.4. A picture of an nELBE detector setup is shown in figure 4.3. At variance to the shown setup, in this experiment four of the five plastic scintillation detectors were located close to each other, next to the BaF$_2$ array, to detect neutrons scattered under angles near $90°$ from the direction of the neutron beam. To determine the energy dependent cross section of the reaction mentioned above the time-of-flight of the incident neutron is measured by detecting the photon emitted from the Fe target in the BaF$_2$ array and the time-of-flight of the scattered neutron is measured by detecting it in one of the plastic scintillation detectors. Thereby, the time-of-flight is determined from the measured time signal relative to the micro-pulse signal from the

ELBE-accelerator. The micro-pulse signal shown in figure 4.4 serves as a reference signal. In the time-of-flight spectrum the photon-flash peak, i.e. the almost constant time of arrival of the bremsstrahlung photons, stemming from the liquid-lead radiator, can then be used as a time reference. For the following transmission experiment the fifth plastic scintillation detector has been installed directly in the beam.

The nELBE FDDAS was equipped with one Acqiris DC-282 digitizing card and the VMETRO recording card in this experiment and data was acquired in two subsequent runs. In the first run, signals from the BaF$_2$ scintillation detectors #1, #5 and #9 (as numbered in figure 4.5) on the channels 1, 2 and 3 and the micro-pulse signal on channel 4 were acquired in a range from $-1900\,\mathrm{mV}$ to $100\,\mathrm{mV}$, while the internal hardware trigger (leading edge, negative slope) of the FDDAS was set to -300 mV for each of the channels 1, 2 and 3. In the second run, signals from the two photomultiplier tubes of the plastic scintillation detector, which stood directly in the neutron beam, on the channels 1 and 2 and the micro-pulse signal on channel 4 were acquired in a range from $-4900\,\mathrm{mV}$ to $100\,\mathrm{mV}$, while channel 3 was not connected and the internal hardware trigger (leading edge, negative slope) of the FDDAS was set to -900 mV for each of the channels 1 and 2. In both runs, the signals were sampled with $N = 10\,\mathrm{bits}$ for $2.5\,\mathrm{\mu s}$ at a sampling rate $f_S = 2\,\mathrm{GS/s}$, i.e. the sampling interval was $\Delta t = 0.5\,\mathrm{ns}$, resulting in 5000 data points per channel per event. The pre-trigger-delay, i.e. the number of data points which are stored before the trigger point was set to 512 in the first run and 2048 in the second run. In each of both runs, 1 536 000 events with a total size of 60 GiB of data were digitized, and stored for an offline analysis described in section 4.4.2.

Figure 4.3: The nELBE detector setup. The array of 42 BaF$_2$ scintillation detectors is located in the center of the picture. The five upright stripes on the right are the plastic scintillation detectors which are closely surrounded by a lead shielding. The collimated neutron beam enters the room at the left edge at the position where, here, the beam shutter (metallic cylinder) is shown, follows through another collimator made of yellow lead bricks left of the BaF$_2$ array, passes the two detector systems and is finally stopped in the beam dump at the right edge.

Analog signal processing at nELBE is done with a home-built constant fraction discrimina-tors [37] with $a_{cf} = 0.22$ and an adjustable delay time t_{cf}. The *VMEbus* data acquisition system (DAQ) uses the 128-channel multihit TDC *CAEN V1190A* [38] with a dispersion of 100 ps per channel and a dynamic range of 52 μs (19 bit). Further information about ASP and the DAQ system at nELBE can be found in reference [9]. Parts of the experi-mental data acquired with this system are analyzed in section 4.4.1 for comparison.

To characterize the digitized signals, figure 4.6 shows a typical signal of the BaF_2 scin-tillation detector #9. The inset in this figure shows this signal in shorter time range. From all signals of this detector a two-dimensional distribution of the amplitude v_{min} vs. the timing information t_{det} extracted with the FCFT method with $c_{cf} = 0.5$ is shown in figure 4.7. The histogram is limited in the time t_{det} to the inspection window of the analysis. On can see that the majority of events is close to the trigger time $(512 \cdot 0.5\,\mathrm{ns})$. The events with amplitudes to low to be triggered $(v_{min} > -300\,\mathrm{mV})$ are digitized if one of the other detectors triggered. In the same way a typical signal and the 2D his-togram are shown for the two PMTs of the plastic scintillation detectors in figures 4.8, 4.9, 4.10 and 4.11. In figure 4.10 a signal is shown, which leaves the range of the FD-DAS and is therefore distorted. In the 2D distribution one can see that these signals at $v_{min} = -4900\,\mathrm{mV}$ dominate the distribution. Further discussion of this phenomenon can be found in section 4.4.2. The time-scale difference of the two histograms is due to an offset of 100 ns between PMT0 and PMT1. Hence, in most of the cases PMT0 triggered the event. This explains why in the histogram of PMT0 only a few events have amplitudes $v_{min} > -800\,\mathrm{mV}$ while in the histogram of PMT1 also a large amount of signals with this low amplitudes is present which did not fulfill the trigger condition.
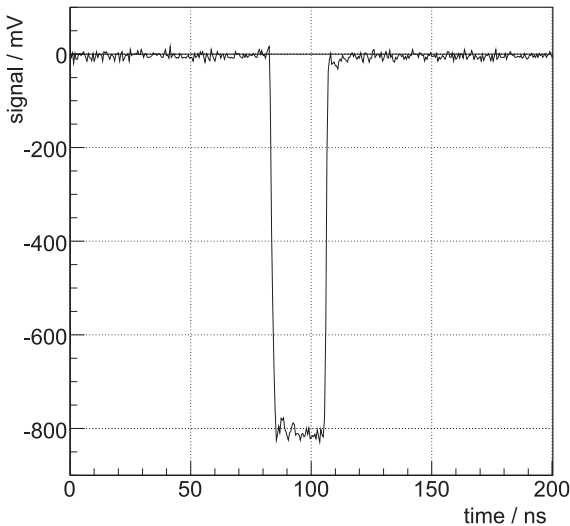
Figure 4.4: The digitized ELBE micro-pulse signal, from which t_{ref} is determined, was acquired together with the detector signal.
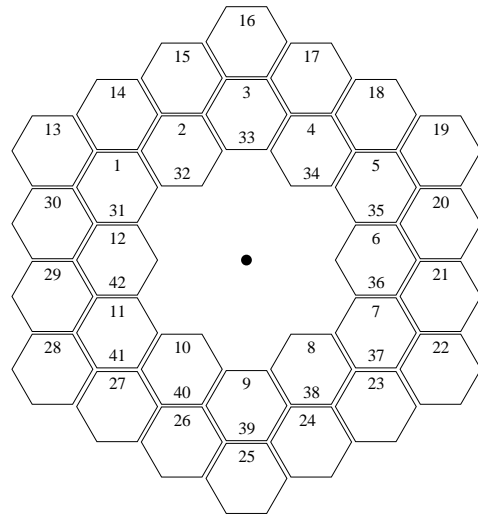
Figure 4.5: Sketch of the nELBE BaF_2 array with the consecutively numbered detectors. The neutron beam (centered black spot) points out of the plane. In the inner ring of the array, two detectors are installed head to head, whereas the detectors 1 – 12 are closer to the neutron beam dump. [36]
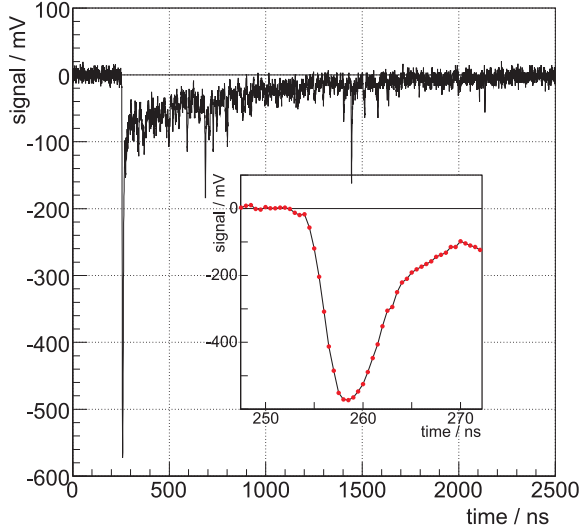
Figure 4.6: Digitized signal of the BaF$_2$ detector #9.
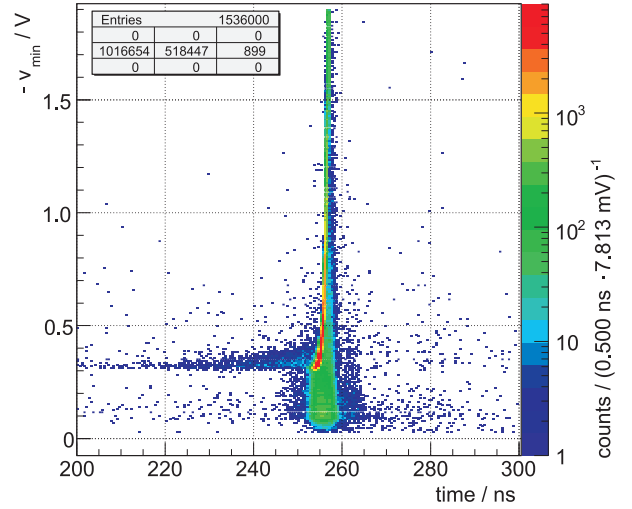
Figure 4.7: 2D histogram of t_{det} vs. v_{min} of the BaF$_2$ detector #9.
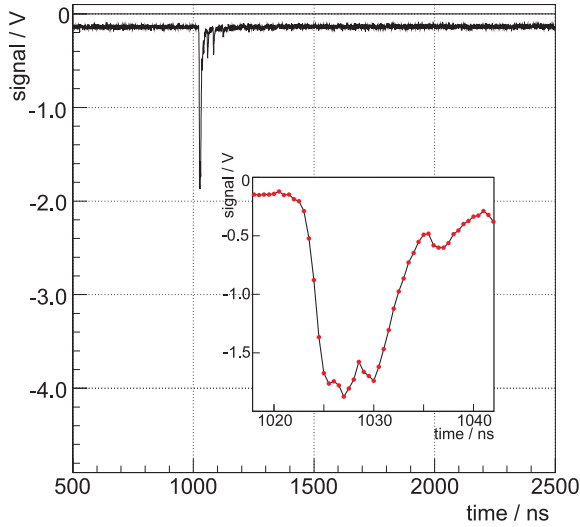
Figure 4.8: Digitized signal of the PMT0 of the plastic scint. detector.
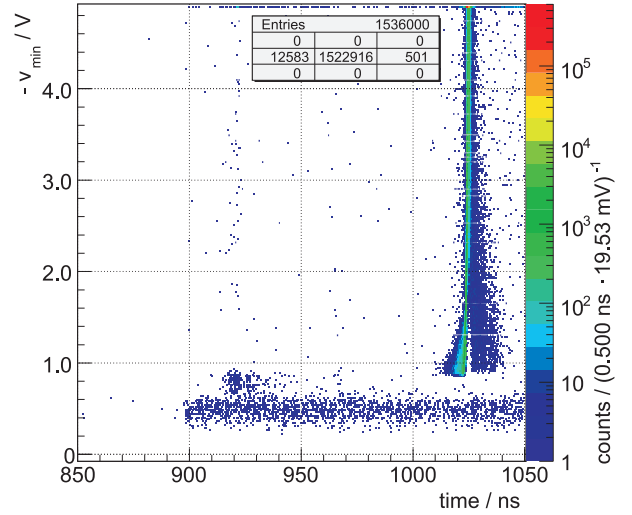
Figure 4.9: 2D histogram of t_{det} vs. v_{min} of the PMT0.
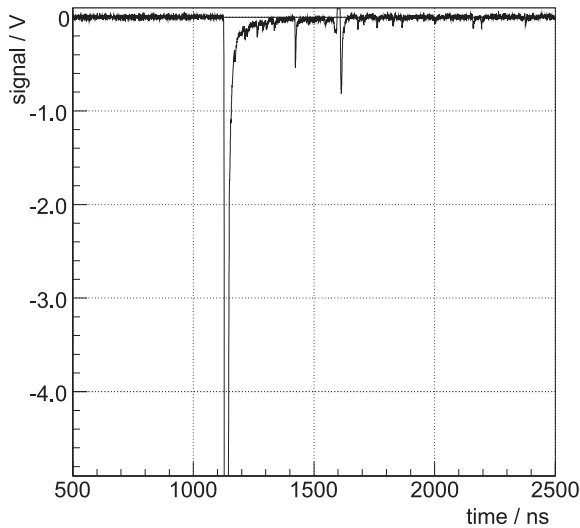
Figure 4.10: Digitized signal of the PMT1 of the plastic scint. detector.
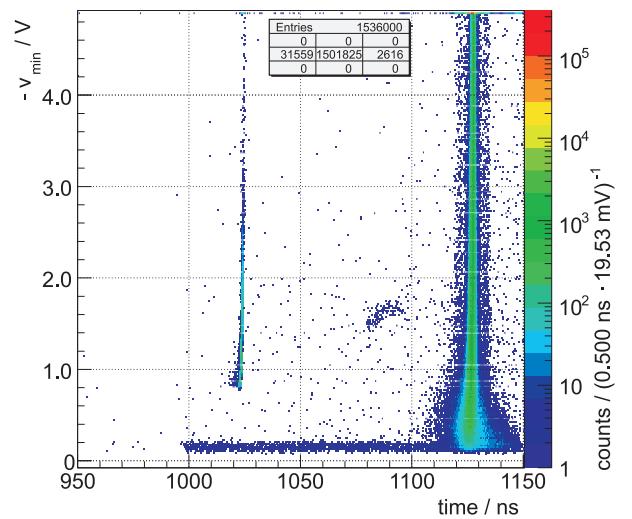
Figure 4.11: 2D histogram of t_{det} vs. v_{min} of the PMT1.

4.4   Time Resolution of BaF$_2$ and Plastic Scintillation Detectors

The timing methods described in section 4.2 are applied to data acquired with three of the 42 BaF$_2$ scintillation detectors and one of the five plastic scintillation detectors during an nELBE experiment as described in section 4.3. The detector signals, i.e. the signals of the photomultiplier tubes mounted to the scintillators, are processed using the methods leading edge timing (LET), extrapolated leading edge timing (ELET), zero-crossing shaper timing (ZCT), zero-crossing constant fraction timing (ZCCFT), constant fraction timing (CFT) and fitting constant fraction timing (FCFT) with different parameters to extract the timing information t_{det}.

From the ELBE micro-pulse signal of the same event a reference timing information t_{ref} is determined with the LET method with a threshold $v_{th} = -400 \, \text{mV}$. For the signals of the BaF$_2$ scintillation detectors the difference

$$t_{BaF2} = t_{det} - t_{ref} \tag{4.6}$$

is filled into histograms. For the signals of the plastic scintillation detectors, which have one photomultiplier tube (PMT0 or PMT1) mounted to each end, the difference

$$t_{plast} = (t_{PMT0} + t_{PMT1})/2 - t_{ref} \tag{4.7}$$

is used, in which $t_{PMT0} = t_{det}(\text{PMT0})$ and $t_{PMT1} = t_{det}(\text{PMT1})$.

To investigate the timing capability of the nELBE FDDAS, the time resolution (FWHM) of the photon-flash peak in the time spectra of t_{BaF2} and t_{plast} is investigated. Since the ELBE electron bunches are very short (some ps) and the interaction between the electron beam and the nELBE liquid-lead radiator takes place in a small volume ($0.6 \, \text{cm}^3$), the uncertainty of the generation time contributing to the FWHM can be neglected. The fitting tool of ROOT is used to perform a least-square fit with the gaussian function

$$f(x) = Ae^{-\frac{(x-\mu)^2}{2\sigma^2}} \tag{4.8}$$

to the photon-flash peaks, in which A is the amplitude, μ is the mean, σ is the standard deviation and $FWHM = \sigma \cdot 2\sqrt{2 \ln 2}$ is the time resolution. For making the results of the digital methods comparable to the analog analysis, the bin width of the histograms in DSP is chosen close to the fixed bin width of the histograms of the analog data analysis, which is 98 ps. A possible influence of the DSP bin width on the FWHM was investigated and can be neglected for a bin width of 100 ps or smaller.

4.4.1   Analogously Processed Data

As a result of the analysis of the data processed and acquired with state of the art electronics mentioned before, figure 4.12 shows the distribution of t_{BaF2} of the BaF$_2$ detector #9 and figure 4.13 shows the distribution of t_{plast}. In both figures only the part with the photon-flash peak is shown. The plastic scintillator stood in the beam during the experiment and detected about ten times more events than each of the BaF$_2$ scintillation detectors which surrounded the in-beam scattering target and mainly detected scattered photons. In both cases a peak about 24 ns before the main peak is present.

This peak is due to electron beam losses in the beam line towards nELBE neutron generator. Thereby, electrons sometimes hit structural materials of the beam guiding system and create bremsstrahlung that arrives earlier than bremsstrahlung from the liquid lead target. The suppression of the pre-photon-flash towards the main photon-flash is higher for the plastic scintillator because its position is better shielded by concrete walls and is also further away than the position of the BaF$_2$ detectors. Another peak in the time distribution of the BaF$_2$ detectors 6 ns after the main peak is also suppressed by two orders of magnitude. It is assumed that backscattering of photons from the lead shielding of the plastic scintillator in the beam is the origin of this post-photon-flash. The time resolutions (FWHM) are determined from the main photon-flash peaks. In this experiment with analog signal processing they are 1.08 ns, 0.82 ns and 0.79 ns for the BaF$_2$ scintillation detectors #1, #5 and #9, respectively, and 0.98 ns for the plastic scintillation detector.
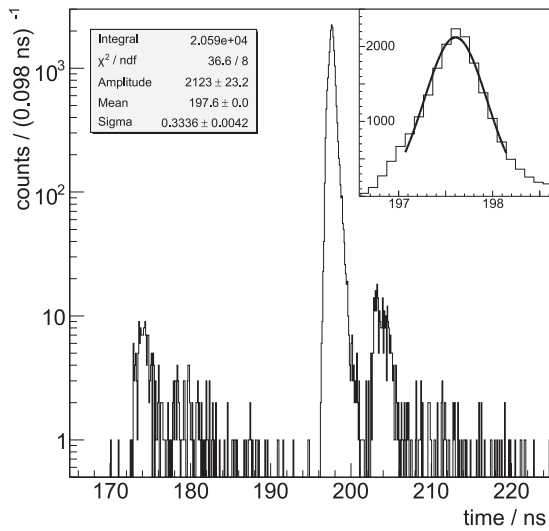
Figure 4.12: Spectrum (photon-flash peak) of t_{BaF2} determined from analog processed signals of the BaF$_2$ scintillation detector #9. In the upper right inset the peak fitted with a Gaussian function is shown.
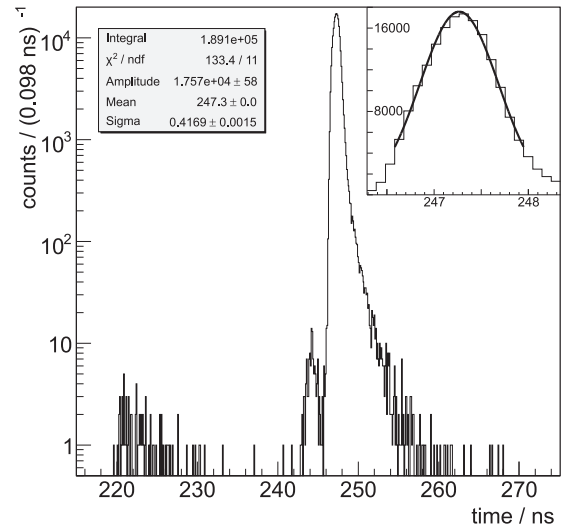
Figure 4.13: Spectrum (photon-flash peak) of t_{plast} determined from analog processed signals of the plastic scintillator. In the upper right inset the peak fitted with a Gaussian function is shown.

4.4.2 Digitally Processed Data

In the case of the negative signals of the BaF$_2$ detectors the voltage range is -1900 mV to 100 mV while no systematic offset of the signals' baseline is observed. The FDDAS triggered to the first signal coming from one of the three detectors with a internal hardware trigger (leading egde, negative slope) and a threshold of -300 mV. The analysis is limited to a narrow range of 200 to 300 ns, which includes the trigger time, in order to save analysis time. A digital copy of each detector signal signal is smoothed with the central moving-average filter ($a = 15$). If the pulse height of a smoothed signal is smaller than 30 mV, the signal is rejected.

The analysis of the ELBE micro-pulse signal, which triggered no events, is performed over the whole time range from 0 to 2500 ns. In the analysis, a few events are found with no reference time t_{ref} and are rejected. The absence of t_{ref} is possible since the accelerator

works with a micro-pulse rate of 101.5625 kHz, i.e. the electron bunch interval is about 10 μs and hence twice as long as the time range. The total number of triggered events is 1 536 000, whereas the number of accepted events is about 500 000 for the detectors #1 and #5, respectively, and about 450 000 for detector #9.

In the case of the negative signals of the two PMTs of the plastic scintillation detectors the voltage range is, as mentioned before, -4900 mV to 100 mV. The FDDAS triggered to the first signal coming from one of the two PMTs of the detector with a internal trigger (leading egde, negative slope) and a threshold of -900 mV. The analysis is limited to a narrow range of 850 to 1050 ns (PMT0) and 950 to 1150 ns (PMT1), where coincident photon-flash events are expected. The different time windows are due to a delay of about 100 ns between the two signals which was installed to suppress electronic cross-talk. A distribution of $t_{PMT1} - t_{PMT0}$ is shown in figure 4.14, while the CFT method with $c_{cf} = 0.1$ was applied.

The analysis of the ELBE micro-pulse signal is done as for BaF$_2$. In the signals of PMT0 there is a systematic offset, which is determined and finally corrected by averaging the baseline and subtracting the offset. The total number of triggered events is 1 536 000. In 80% of all events one or both PMTs show signals, which have high amplitudes ($v_{min} < -4900$ mV) and leave the range of the digitizer (see also figure 4.10). These events are rejected as well as signals that do not fulfill the coincidence condition 90 ns $< t_{PMT1} - t_{PMT0} < 130$ ns. As for BaF$_2$, signals with very low amplitude are filtered out by a central moving average filter ($a = 15$, 30 mV). Finally there are about 260 000 accepted events. In figure 4.15 a spectrum of t_{plast} for all coincident events of the PMTs of the plastic scintillation detector is shown in a larger range. Apart from the photon-flash peak, a broad distribution of neutrons is visible.
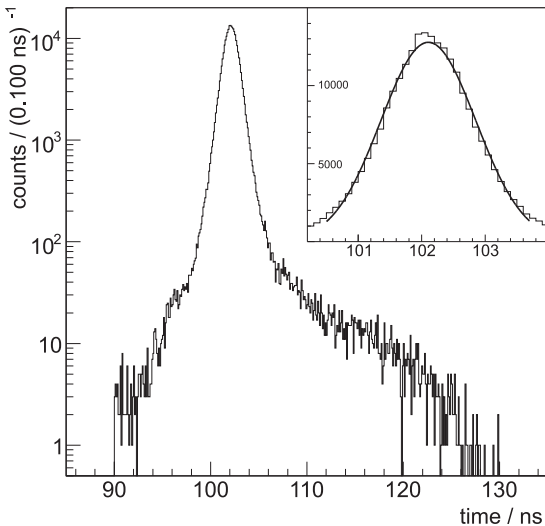
Figure 4.14: Spectrum of $t_{PMT1} - t_{PMT0}$. In the upper right inset the peak fitted with a Gaussian function is shown.
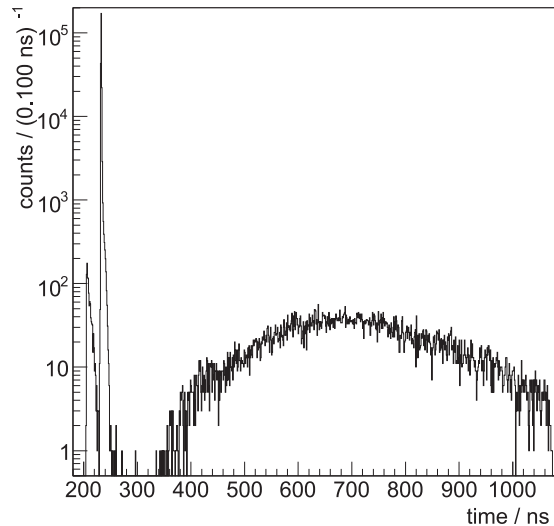
Figure 4.15: Full spectrum of t_{plast} determined from digitally processed signals of the PMTs of the plastic scintillation detector. The photon-flash peak is followed by a broad distribution of neutrons.

4.4.3   Comparison of Timing Algorithms

The results of the methods applied are presented in this section in the three following ways: (a) The determined time resolutions (FWHM) are plotted for each method as a function of the parameters varied to compare the detectors to each other on the one hand and different parameter sets to each other on the other hand. For further comparison the results of the analog analysis are shown as dashed, horizontal lines in these plots. (b) For one selected parameter set (usually the one which produces the best result) of each method the photon-flash peak in the distribution of t_{BaF2} and t_{plast} is plotted in a similar way as in figures 4.12 and 4.13 to compare the different methods to each other and to the analog result. (c) For all methods and parameter sets the determined time resolutions (FWHM) are presented in tables at the end of this section. The parts (a) and (b) are discussed in the following subsections, while similar methods are discussed together.

Leading Edge Timing and Extrapolated Leading Edge Timing

The LET method is applied with thresholds v_{th} from $-25\,$mV to $-1500\,$mV. ELET is applied with the lower threshold v_{th1} as in LET and the higher threshold $v_{th2} = f_{th} \cdot v_{th1}$, whereas the stretch factor f_{th} is 1.5, 2.0, 2.5 or 3.0. Figure 4.16 shows clearly, that the LET method applied to the detector signals results in a worse time resolution than the analog reference values. The best results are obtained with thresholds near the baseline, the worst with a threshold at the trigger level of the FDDAS. If the threshold is moved from this point up to the maximal amplitude, the results seem to become better again. The reason for that is that the further the threshold is away from the baseline the more signals are not recognized by the LET method since their amplitude is too small. Therefore, the variation of the amplitudes of the recognized signals becomes smaller and the walk effect is decreased with the drawback that more signals are rejected. The signals of the plastic scintillation detector, which have amplitudes up to $-4900\,$mV, are less sensitive to this effect at the investigated thresholds.

The results of the ELET method are not competetive in their time resolution and are therefore not shown. The problem of the rejection of signals smaller than the threshold occurs here, too. The fitted photon-flash peaks in the distributions of t_{BaF2} and t_{plast} are shown for LET with $v_{th} = -50\,$mV in figure 4.21 for BaF$_2$ detector #9 and in figure 4.27 for the plastic scintillation detector. There, it can be observed that the shape of the analog spectrum is well reproduced for BaF$_2$, while in the spectrum of the plastic scintillation detector lots of signals between the photon-flash peak and and the pre-photon-flash peak disturb the spectrum.

Zero-Crossing Shaper Timing

The ZCT method is applied with τ from $0.1\,$ns to $10.0\,$ns, which is the time constant of the used digital CR- and RC-shapers. As mentioned before the sampling interval was $\Delta t = 0.5\,$ns. Under the condition $\Delta t \ll \tau$ the used shapers are precise digital representations of their analog counterparts, but even in the cases investigated here they should show a similar behavior. In figure 4.17 the time resolution is shown as a function of τ. For all detectors this function is similar with a minimum between $\tau = 0.1\,$ns and $\tau = 1\,$ns. Smaller time-constants were not investigated since the output signal became too small in this case. For $\tau = 1\,$ns, the fitted photon-flash peak is shown in figure 4.22

for BaF_2 detector #9. For BaF_2, results similar to or better than ASP are obtained. In the case of the plastic scintillation detector, figure 4.28 shows a photon-flash peak, which is widened towards longer times. Here the results are worse compared to ASP.

Zero-Crossing Constant Fraction Timing

Using the ZCCFT method the delay parameter m is here 3, 5 or 10 points and the attenuation factor a_{cf} varies between 0.05 and 0.60. As can be seen in figure 4.18, each curve has a clear minimum, that moves towards smaller values of a_{cf} while m increases. Except for BaF_2 detector #1 the time resolution improves for increasing m, too. For all BaF_2 detectors much better results are obtained than with ASP, while for the plastic scintillation detector this is only with $m = 10$ the case. For BaF_2 detector #9, figure 4.23 shows the photon-flash peak for $m = 10$ and $a_{cf} = 0.15$. The photon-flash peak of the plastic scintillation detector is shown in figure 4.29 for $m = 10$ and $a_{cf} = 0.10$.

Constant Fraction Timing and Fitting Constant Fraction Timing

The parameter c_{cf} is varied between 0.025 and 0.80 for the CFT and the FCFT method. Also the peak time, i.e. the time when v_{min} (or v'_{min}) is reached, is determined and denoted with $c_{cf} = 1.0$. In figure 4.19 the time resolution is shown as a function of c_{cf} for both methods and the four detectors of the experiment. For all detectors much better results are obtained than with ASP. The differences between CFT and FCFT are very small except for the plastic scintillation detector, where the CFT gives slightly better resolutions. Also the photon-flash peaks shown in figures 4.24 and 4.25 as well as in figures 4.30 and 4.31 show nearly no differences and are also very similar to their counterparts of the ZCCFT method. The fact that FCFT gives equal resolutions as CFT means, that (a) the linear interpolation in CFT is competitive to the fit used in FCFT and (b) the more precise pulse height determination has no effect, since the corrections in the order of $3\% - 5\%$ do not influnce the walk effect significantly.
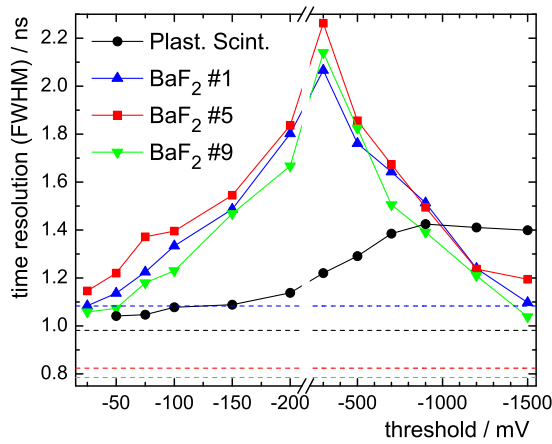
Figure 4.16: Time resolution achieved with LET. Note the change of the threshold scale at $-250\,\mathrm{mV}$. Data is listed in table 4.1.
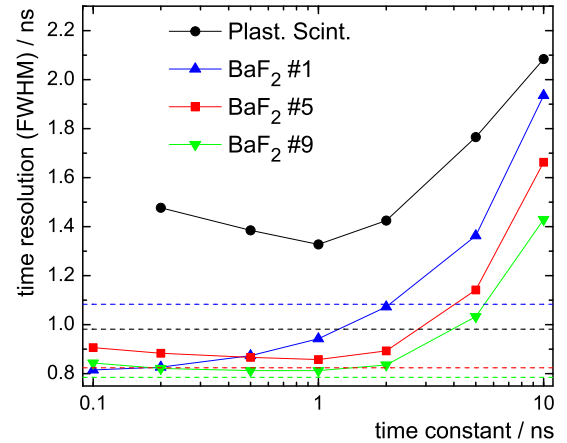
Figure 4.17: Time resolution achieved with ZCT. Note the logarithmic time-constant scale. Data is listed in table 4.2.
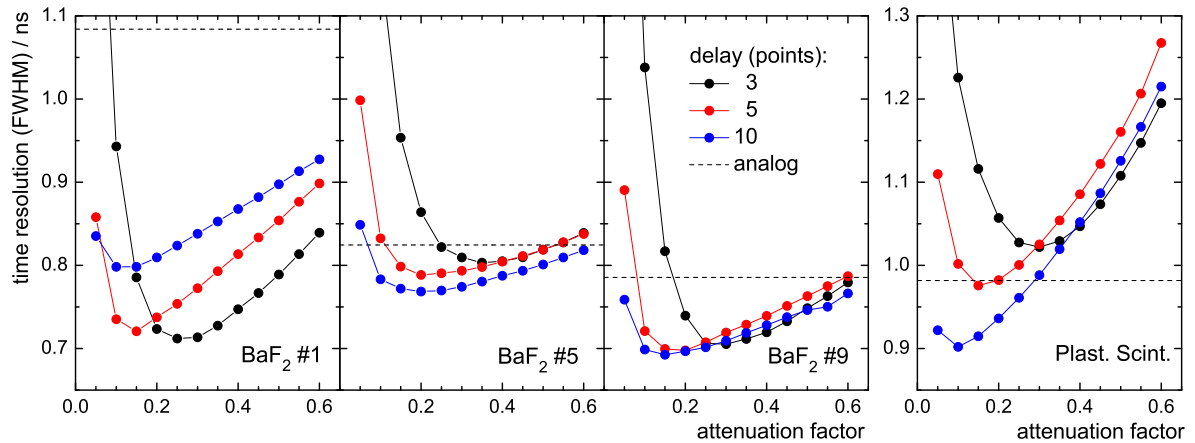
Figure 4.18: Time resolution achieved with ZCCFT. Note the different scale of the right diagram. Data is listed in 4.3.
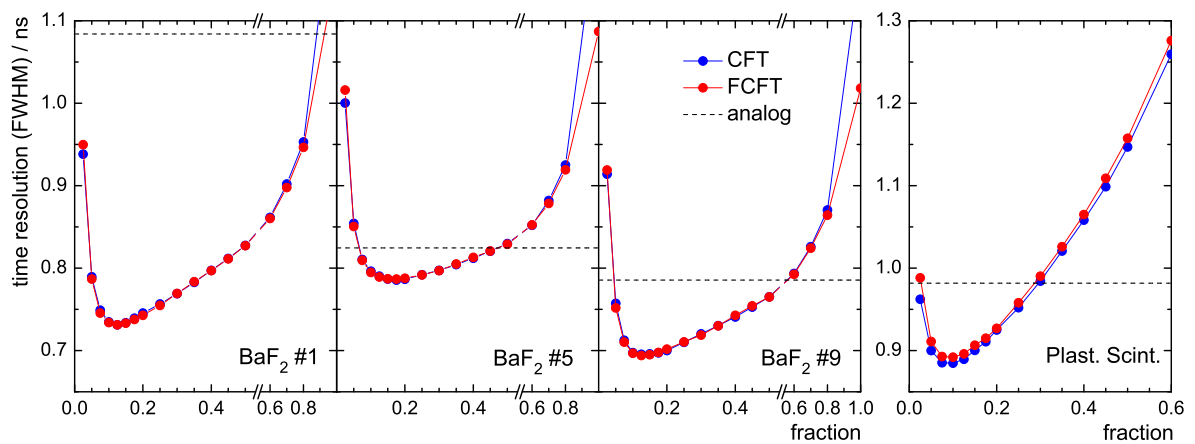
Figure 4.19: Time resolution achieved with CFT and FCFT. Note the different scales of the right diagram. Data is listed in table 4.4.
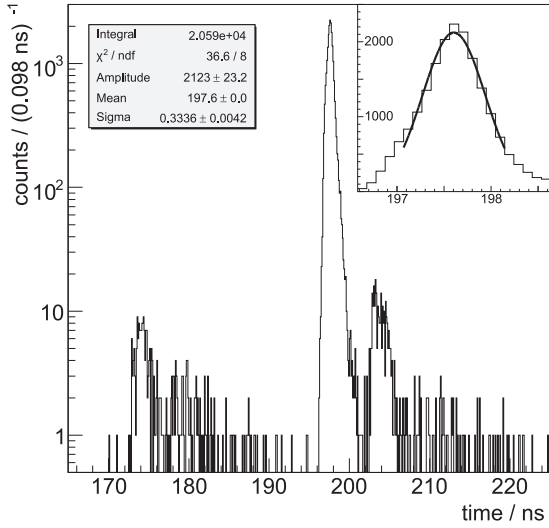
Figure 4.20: ASP (figure 4.12)
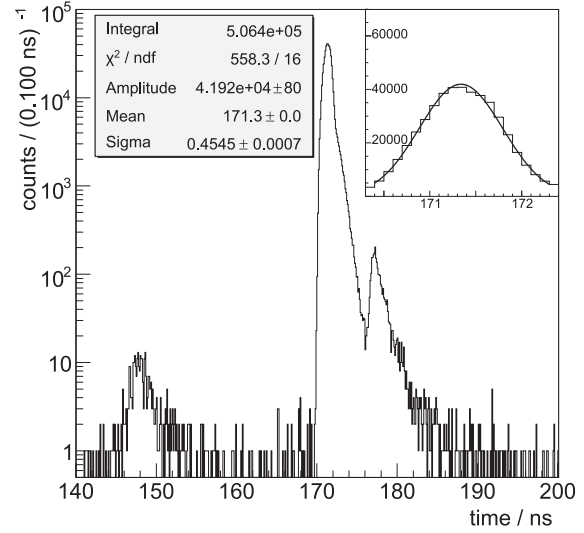
Figure 4.21: LET, $v_{th} = -50\,\text{mV}$
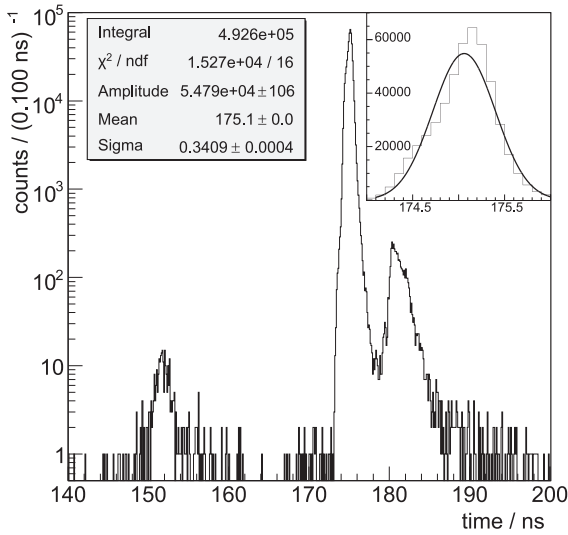
Figure 4.22: ZCT, $\tau = 1.0\,\text{ns}$
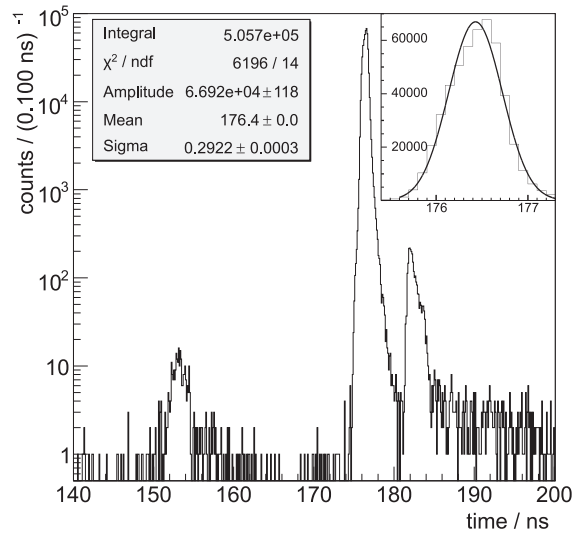
Figure 4.23: ZCCFT, $a_{cf} = 0.15$, $m = 10$
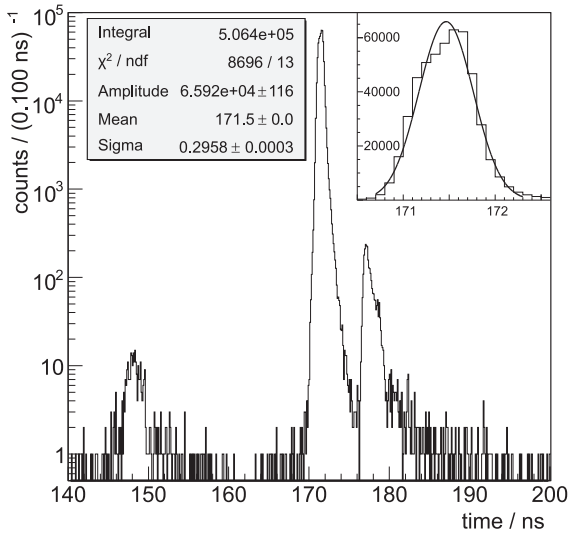
Figure 4.24: CFT, $c_{cf} = 0.125$
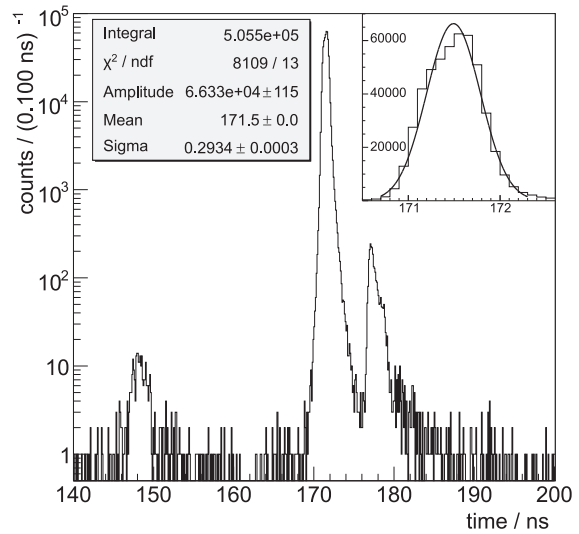
Figure 4.25: FCFT, $c_{cf} = 0.125$

Figures 4.21 - 4.25: Photon-flash peaks in the spectra of t_{BaF2} determined from digital processed signals of the BaF_2 detector #9.
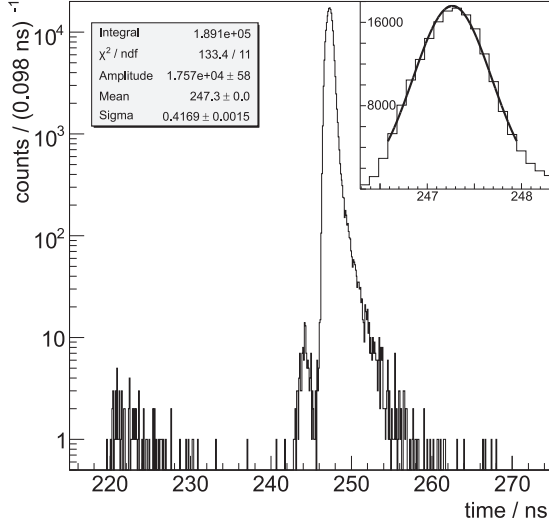
Figure 4.26: ASP (figure 4.13)
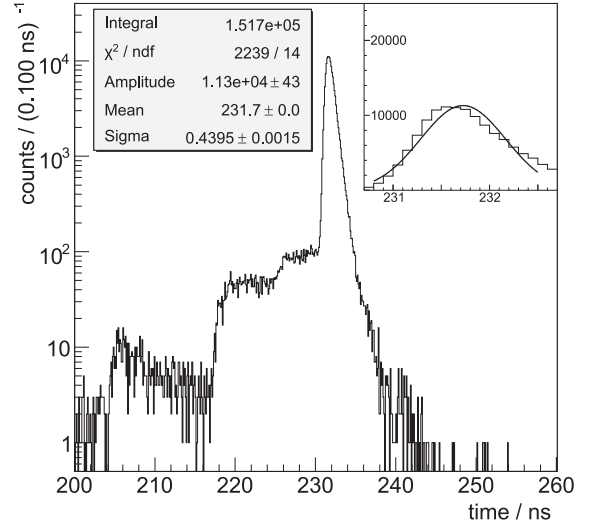
Figure 4.27: LET, $v_{th} = -50\,\mathrm{mV}$
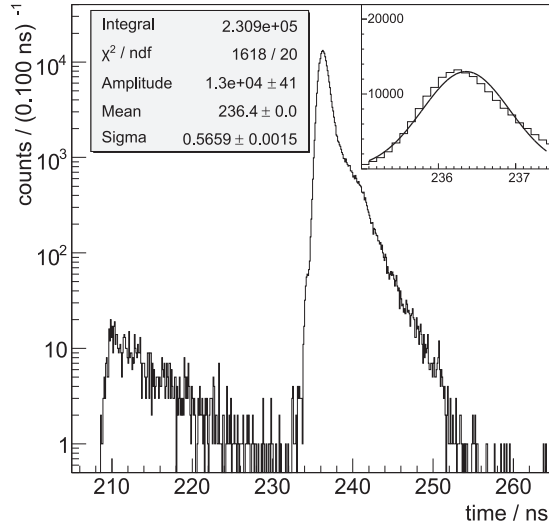
Figure 4.28: ZCT, $\tau = 1.0\,\mathrm{ns}$
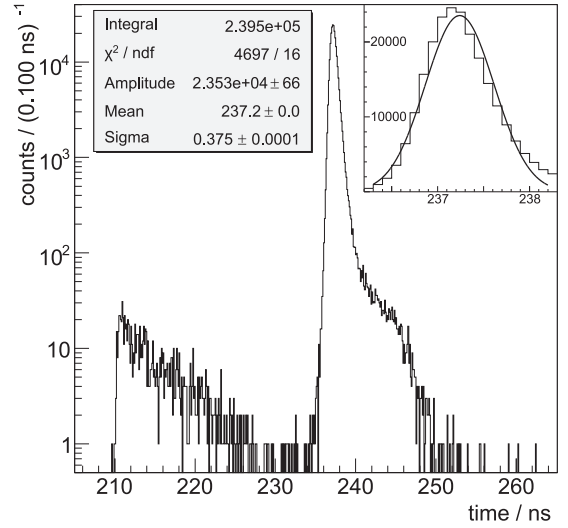
Figure 4.29: ZCCFT, $a_{cf} = 0.10$, $m = 10$
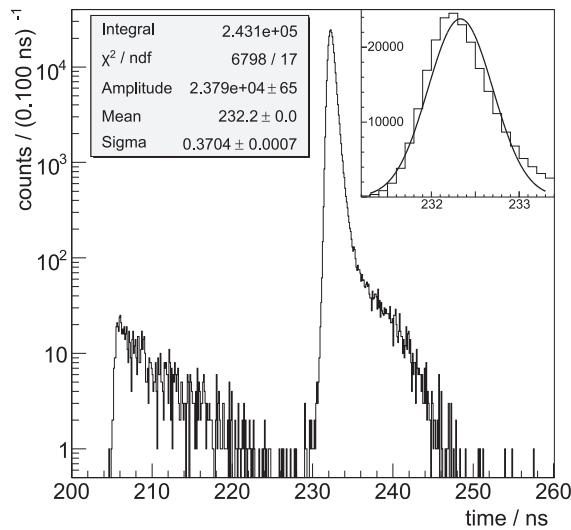
Figure 4.30: CFT, $c_{cf} = 0.10$
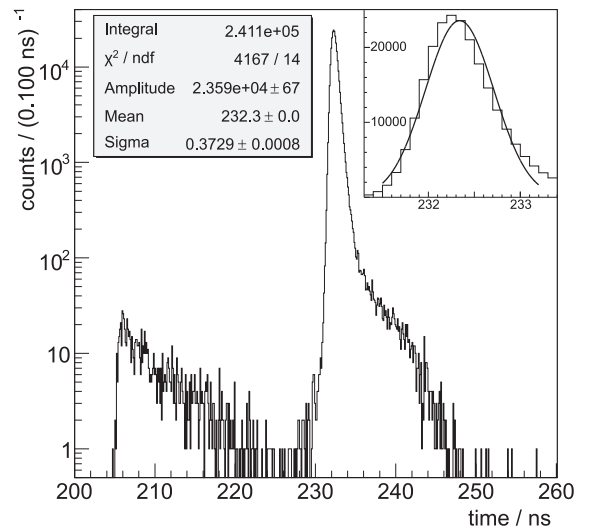
Figure 4.31: FCFT, $c_{cf} = 0.10$

Figures 4.27 - 4.31: Photon-flash peaks in the spectra of t_{plast} determined from digital processed signals of the PMTs of the plastic scintillation detector.

v_{th} / mV ↓	BaF$_2$ #1	BaF$_2$ #5	BaF$_2$ #9	Plast. Scint.
-25	1.08	1.15	1.06	
-50	1.14	1.22	1.07	1.04
-75	1.23	1.37	1.18	1.05
-100	1.33	1.40	1.23	1.08
-150	1.49	1.55	1.47	1.09
-200	1.80	1.84	1.67	1.14
-300	2.07	2.26	2.14	1.22
-500	1.76	1.86	1.82	1.29
-700	1.64	1.67	1.51	1.39
-900	1.51	1.49	1.39	1.43
-1200	1.24	1.24	1.21	1.41
-1500	1.10	1.20	1.04	1.40

Table 4.1: Time resolution (FWHM) / ns of the tested detectors with the LET method. The varied parameter is the threshold v_{th}.

τ / ns ↓	BaF$_2$ #1	BaF$_2$ #5	BaF$_2$ #9	Plast. Scint.
0.1	0.82	0.91	0.84	
0.2	0.83	0.88	0.82	1.48
0.5	0.87	0.87	0.81	1.39
1.0	0.94	0.86	0.81	1.33
2.0	1.07	0.89	0.84	1.42
5.0	1.36	1.14	1.03	1.77
10.0	1.94	1.66	1.43	2.08

Table 4.2: Time resolution (FWHM) / ns of the tested detectors with the ZCT method. The varied parameter is the time constant τ of the used CR- and RC-shapers.

a_{CF}	BaF$_2$ #1	$m \rightarrow$		BaF$_2$ #5	$m \rightarrow$		BaF$_2$ #9	$m \rightarrow$		Plast. Scint. $m \rightarrow$		
$\downarrow$	3	5	10	3	5	10	3	5	10	3	5	10
0.05	1.43	0.86	0.84	1.62	1.00	0.85	1.63	0.89	0.76	1.48	1.11	0.92
0.10	0.94	0.74	0.80	1.16	0.83	0.78	1.04	0.72	0.70	1.23	1.00	0.90
0.15	0.79	0.72	0.80	0.95	0.80	0.77	0.82	0.70	0.69	1.12	0.98	0.91
0.20	0.72	0.74	0.81	0.86	0.79	0.77	0.74	0.70	0.70	1.06	0.98	0.94
0.25	0.71	0.75	0.82	0.82	0.79	0.77	0.71	0.71	0.70	1.03	1.00	0.96
0.30	0.71	0.77	0.84	0.81	0.79	0.77	0.71	0.72	0.71	1.02	1.03	0.99
0.35	0.73	0.79	0.85	0.80	0.80	0.78	0.71	0.73	0.72	1.03	1.05	1.02
0.40	0.75	0.81	0.87	0.80	0.80	0.79	0.72	0.74	0.73	1.05	1.09	1.05
0.45	0.77	0.83	0.88	0.81	0.81	0.79	0.73	0.75	0.74	1.07	1.12	1.09
0.50	0.79	0.85	0.90	0.82	0.82	0.80	0.75	0.76	0.75	1.11	1.16	1.13
0.55	0.81	0.88	0.91	0.83	0.83	0.81	0.76	0.77	0.75	1.15	1.21	1.17
0.60	0.84	0.90	0.93	0.84	0.84	0.82	0.78	0.79	0.77	1.20	1.27	1.22

Table 4.3: Time resolution (FWHM) / ns of the tested detectors with the ZCCFT method. The varied parameters are the attenuation factor a_{cf} and the delay time $t_{cf} = m \cdot \Delta t$.

c_{cf}	BaF$_2$ #1		BaF$_2$ #5		BaF$_2$ #9		Plast. Scint.	
$\downarrow$	CFT	FCFT	CFT	FCFT	CFT	FCFT	CFT	FCFT
0.025	0.94	0.95	1.00	1.02	0.91	0.92	0.96	0.99
0.050	0.79	0.79	0.85	0.85	0.76	0.75	0.90	0.91
0.075	0.75	0.75	0.81	0.81	0.71	0.71	0.89	0.89
0.100	0.73	0.73	0.80	0.79	0.70	0.70	0.88	0.89
0.125	0.73	0.73	0.79	0.79	0.70	0.69	0.89	0.90
0.150	0.73	0.73	0.79	0.79	0.70	0.69	0.90	0.91
0.175	0.74	0.74	0.79	0.79	0.70	0.70	0.91	0.92
0.200	0.75	0.74	0.79	0.79	0.70	0.70	0.92	0.93
0.250	0.76	0.75	0.79	0.79	0.71	0.71	0.95	0.96
0.300	0.77	0.77	0.80	0.80	0.72	0.72	0.98	0.99
0.350	0.78	0.78	0.80	0.80	0.73	0.73	1.02	1.03
0.400	0.80	0.80	0.81	0.81	0.74	0.74	1.06	1.07
0.450	0.81	0.81	0.82	0.82	0.75	0.75	1.10	1.11
0.500	0.83	0.83	0.83	0.83	0.77	0.77	1.15	1.16
0.600	0.86	0.86	0.85	0.85	0.79	0.79	1.26	1.28
0.700	0.90	0.90	0.88	0.88	0.83	0.82	1.41	1.44
0.800	0.95	0.95	0.92	0.92	0.87	0.86	1.69	1.70
1.000	1.28	1.16	1.23	1.09	1.17	1.02	2.52	2.41

Table 4.4: Time resolution (FWHM) / ns of the tested detectors with the CFT and FCFT method. The varied parameter is the fraction c_{cf}.

Chapter 5

Conclusion and Outlook

The fast-digitizer data acquisition system installed at the nELBE experiment was tested in a configuration with one digitizer card, which makes it possible to perform short and simple experiments with four input channels. The strong point of the FDDAS was seen in the timing measurements of signals with short risetimes from BaF_2 and plastic scintillation detectors. In combination with timing algorithms, which compensate the walk effects, better time resolutions were achieved than with a state-of-the-art analog-signal processing system. From the tested algorithms, the leading edge timing methods (LET and ELET) resulted in no improvement or were impracticable. Applying an algorithm, which determines the time information from the zero-crossing of the shaped input signal (ZCT), the time resolution was competitive to analog reference values for the BaF_2 detectors only. The method using the working principle of an analoge constant-fraction discriminator (ZCCFT) and the methods which measure the pulse height in order to set the threshold to a constant fraction (CFT, FCFT) gave the best results. CFT and FCFT are ways of signal processing which are only feasible with digital signal processing. It showed that no significantly higher precision is obtained with fitting algorithms applied to the digitized signals used here. Further investigations should also take differences in the pulse shape into account to find the optimal timing method. A weak point which became obvious during the analysis was the response of the timing methods to low-amplitude signals and in this context the role of the analog trigger. A subject of interest for future experiments at nELBE will also be the investigation of the pulse shapes in order to find out if signals from the experiment can be discriminated from underground signals or noise in the photomultiplier.

In the measurements with the HPGe detector it turned out that the 10-bit digitizer is not competitive to a state-of-the-art analog-signal processing system with a 14-bit ADC, which even had a four times larger dynamic range. It was shown that the moving window deconvolution algorithm can reduce the ballistic deficit and improve the energy resolution. Thereby, the shaping algorithms creating a flat-top gave the best results. A correction of piled-up events or events with BGO veto signal was not included in the analysis, since the influence of these effects should be negligible under the experimental conditions described in this work.

At the moment, technical difficulties with the external trigger input and the limited flexibility of the internal trigger hinder longer experiments with a bigger detector system that uses all four cards. Furthermore, there are open questions which have to be answered before such experiments can start. On the one hand, the data acquisition in two crates

with four cards each has to be triggered and synchronized in order to combine the signals of all channels in the following offline analysis. Thereby, it has to be investigated how to synchronize the two crates with each other and if an external trigger limits the performance of the digitizer system. On the other hand, such experiments will create huge amounts of data and the capacity of the storage device will become a limiting factor. Plans exist to reduce unwanted data online with filter algorithms implemented on the digitizer card. This works in principle but has not been tested under experimental conditions, yet. Anyhow, the first measurements have been performed successfully in this work and a modular analysis program was developed. The trigger-rearm time and the data transfer time were investigated and apart from some small technical problems, the hardware has proved to be suitable for experiments at nELBE.

Appendix A

C Algorithms for Digital Signal Processing

A.1 Auxiliary Functions

```
00 double func_average (const double *v, int start, int stop)
01 { int i;  double sum=0;
02   for (i=start; i<stop; i++) sum+=v[i];
03   return sum/(double)(stop-start);
04 }

00 double func_rms (const double *v, int start, int stop)
01 { int i;  double sum=0;
02   for (i=start; i<stop; i++) sum+=v[i]*v[i];
03   return sqrt(sum/(double)(stop-start));
04 }

00 int func_extreme_value (const double *v, int start, int stop, int sign)
01 { int i, t=0;  double ev=v[start];
02   if (sign > 0)
03   { for (i=start+1; i<stop; i++)
04       if (v[i] > ev)
05       { ev=v[i];  t=i;
06       }
07   }
08   else
09     for (i=start+1; i<stop; i++)
10       if (v[i] < ev)
11       { ev=v[i];  t=i;
12       }
13   return t;
14 }

00 double func_interpolate (const double *v, int i, double th, double dt)
01 { return (i+(th-v[i])/(v[i+1]-v[i]))*dt;
02 }
```

```
00 void func_add_to_wf (double *v, int start, int npts, double add)
01 { int i;
02   for (i=start; i<start+npts; i++) v[i]+=add;
03 }


00 void func_stretch_wf (double *v, int start, int npts, double f)
01 { int i;
02   for (i=start; i<start+npts; i++) v[i]*=f;
03 }
```

A.2 Pulse Shaping Functions

```
00 void module_CR_diff_HP (const double *v, double *s, int npts,
double dt, double tau)
01 { int i;  double alpha=tau/(tau+dt);
02   s[0]=0;
03   for (i=1;i<npts;i++)
04     s[i]=alpha*(s[i-1] + v[i] - v[i-1]);
05 }


00 void module_RC_int_LP (const double *v, double *s, int npts,
double dt, double tau)
01 { int i;  double alpha=dt/(tau+dt);
02   s[0]=v[0];
03   for (i=1;i<npts;i++)
04     s[i]=(1-alpha)*s[i-1] + alpha*v[i];
05 }


00 void module_gaussian (const double *v, double *s, int npts,
double dt, double tau, int n)
01 { int i=0;  double p[npts], norm;
02   if (n > 20)
03     norm=exp((-1)*(double)n)*pow((double)n,(double)n);
04   else
05     norm=1.0/sqrt(2*acos(-1)*n);
06   module_CR_diff_HP(v, s, npts, dt, tau);
07   while (i < n)
08   { if (i%2 == 0)
09       module_RC_int_LP(s, p, npts, dt, tau);
10     else
11       module_RC_int_LP(p, s, npts, dt, tau);
12     i++;
13     if (n > 20) norm/=(double)i;
14   }
15   if (n%2 == 1) module_add_to_wf(p, s, 0, npts, 0);
16   module_stretch_wf(s, 0, npts, 1.0/norm);
17 }
```

```
00 void module_ma (const double *v, double *s, int npts, int l, int a,
int weighting, double alpha)
01 { int i,j;  double w[l];
02   if (a == 0)   // proir moving average
03   { switch (weighting)
04     { case 0: // no weighting, no scaling
05         s[0]=v[0];
06         for (i=1; i<l-1; i++)    s[i]=s[i-1]+v[i];
07         for (i=l-1; i<npts; i++) s[i]=s[i-1]+v[i]-v[i-l];
08         break;
09       case 1: // no weighting, scaling with 1/l
10         s[0]=v[0]/(double(l));
11         for (i=1; i<l; i++)    s[i]=s[i-1]+v[i]/(double(l));
12         for (i=l; i<npts; i++) s[i]=s[i-1]+(v[i]-v[i-l])/(double(l));
13         break;
14       case 2: // linear weigting, scaling with 2/(l*(l+1))
15         for (i=0; i<l; i++)    w[i]=2.0*(l-i)/((double)(l*(l+1)));
16         for (i=0; i<l; i++)
17           for (j=0; j<i; j++)  s[i]+=w[j]*v[i-j];
18         for (i=l; i<npts; i++)
19           for (j=0; j<l; j++)  s[i]+=w[j]*v[i-j];
20         break;
21       case 3: // exponential weigting
22         s[0]=v[0];
23         for (i=1; i<npts; i++) s[i]=(1.0-alpha)*s[i-1]+alpha*v[i];
24         break;
25     }
26   }
27   else if (l == 0) // central moving average
28   { l=2*a+1;
29     switch (weighting)
30     { case 0: // no weighting, no scaling
31         s[0]=v[0];
32         for (i=1; i<a+1; i++)            s[i]=s[i-1]+v[i];
33         for (i=a+1; i<=npts-a; i++)    s[i]=s[i-1]+v[i+a]-v[i-a-1];
34         for (i=npts-a+1; i<npts; i++) s[i]=s[i-1]-v[i-a-1];
35         break;
36       case 1: // no weighting, scaling with 1/l
37         for (i=0; i<a; i++)            s[i]=0;
38         for (i=0; i<l-1; i++)          s[a]+=v[i];
39         for (i=a+1; i<npts-a+1; i++)
40           s[i]=s[i-1]+(v[i+a]-v[i-a-1])/(double(l));
41         for (i=npts-a+1; i<npts; i++) s[i]=0;
42         break;
43     }
44   }
45 }
```

```
00 void module_mwd (const double *v, double *s, int npts, int m,
double tau, double dt)
01 { int i;   double sum=0, k=exp((-1)*dt/tau), d[npts];
02    s[0]=v[0];
03    for (i=1; i<m; i++)
04    { sum = sum+v[i-1];
05      s[i]=v[i]+(1-k)*sum;
06    }
07    sum=sum+v[m-1];
08    s[m]=v[m]-v[0]+(1-k)*sum;
09    for (i=m+1; i<npts; i++)
10    { sum=sum+v[i-1]-v[i-m-1];
11      s[i]=v[i]-v[i-m]+(1-k)*sum;
12    }
13 }


00 void module_trapezoid (const double *v, double *s, int npts, int k,
int m)
01 { int i;   double norm=1/(double(k));
02    s[0]=norm*v[0];
03    for (i=1;i<k;i++)          s[i]=s[i-1]+norm*v[i];
04    for (i=k;i<k+m;i++)        s[i]=s[i-1]+norm*(v[i]-v[i-k]);
05    for (i=k+m;i<2*k+m;i++)  s[i]=s[i-1]+norm*(v[i]-v[i-k]-v[i-k-m]);
06    for (i=2*k+m;i<npts;i++)
07      s[i]=s[i-1]+norm*(v[i]-v[i-k]-v[i-k-m]+v[i-2*k-m]);
08 }


00 void module_cusp_trunc (const double *v, double *s, int npts, int k,
int m)
01 { int i, l=k+m;   double p[npts], norm=2.0/(k*(k+1));
02    p[0]=v[0];   s[0]=norm*p[0];
03    for (i=1;i<k;i++)
04    { p[i]=p[i-1]+v[i];
05      s[i]=s[i-1]+norm*p[i];
06    }
07    for (i=k;i<k+m;i++)
08    { p[i]=p[i-1]+v[i]-v[i-k];
09      s[i]=s[i-1]+norm*(p[i]-v[i-k]*k);
10    }
11    for (i=k+m;i<2*k+m;i++)
12    { p[i]=p[i-1]+v[i]-v[i-k]+v[i-k-m];
13      s[i]=s[i-1]+norm*(p[i]-(v[i-k]+v[i-k-m])*k-v[i-k-m]);
14    }
15    for (i=2*k+m;i<npts;i++)
16    { p[i]=p[i-1]+v[i]-v[i-k]+v[i-k-m]-v[i-2*k-m];
17      s[i]=s[i-1]+norm*(p[i]-(v[i-k]+v[i-k-m])*k-v[i-k-m]+v[i-2*k-m]);
18    }
19 }
```

```
00 void module_triangular (const double *v, double *s, int npts, int k)
01 { int i;   double norm=1/(double(k));
02   s[0]=norm*v[0];
03   for (i=1;i<k;i++)        s[i]=s[i-1]+norm*v[i];
04   for (i=k;i<2*k;i++)     s[i]=s[i-1]+norm*(v[i]-2*v[i-k]);
05   for (i=2*k;i<npts;i++) s[i]=s[i-1]+norm*(v[i]-2*v[i-k]+v[i-2*k]);
06 }


00 void module_cusp (const double *v, double *s, int npts, int k)
01 { int i;   double p[npts], norm=2.0/(k*(k+1));
02   p[0]=v[0];   s[0]=norm*p[0];
03   for (i=1;i<k;i++)
04   { p[i]=p[i-1]+v[i];
05     s[i]=s[i-1]+norm*p[i];
06   }
07   for (i=k;i<2*k+1;i++)
08   { p[i]=p[i-1]+v[i];
09     s[i]=s[i-1]+norm*(p[i]-v[i-k]*(2*k+1));
10   }
11   for (i=2*k+1;i<npts;i++)
12   { p[i]=p[i-1]+v[i]-v[i-2*k-1];
13     s[i]=s[i-1]+norm*(p[i]-v[i-k]*(2*k+1));
14   }
15 }
```

A.3   Timing Functions

```
00 double module_let (const double *v, int start, int stop, double
threshold, int condition, double dt, double no_success)
01 { int i;
02   for (i=start; i<stop-1; i++)
03   { if ((v[i]-threshold)*(v[i+1]-threshold) <= 0)
04       if ((condition==0) || (condition*(v[i]-v[i+1]) < 0))
05         return func_interpolate(v, i, threshold, dt);
06   }
07   return no_success;
08 }
```

```
00 double module_elet (const double *v, int start, int stop, double
threshold, int condition, double dt, double factor, double no_success)
01 { int i=start;  double t1=0.0, t2=0.0;
02   while (i<stop-1)
03   { if ((v[i]-threshold)*(v[i+1]-threshold) <= 0)
04       if ((condition==0) || (condition*(v[i]-v[i+1])<0))
05       { t1=func_interpolate(v, i, threshold, dt);
06         break;
07       }
08     i++;
09   }
10   while (i<stop-1)
11   { if ((v[i]-factor*threshold)*(v[i+1]-factor*threshold) <= 0)
12       if ((condition == 0) || (condition*(v[i]-v[i+1]) < 0))
13       { t2=func_interpolate(v, i, factor*threshold, dt);
14         break;
15       }
16     i++;
17   }
18   if ((t1!=0.0) && (t2!=0.0))
19     return (t1+(module_average(v, 0, 100)-threshold)*(t2-t1)/
((factor-1.0)*threshold));
20   else
21     return no_success;
22 }
```

```
00 double module_zct (const double *v, double *s, int npts, int sign,
double tau, int start, int stop, double dt, double no_success)
01 { int i, i_min=0, i_max=0;
02   double p[npts];
03   module_CR_diff_HP(v, s, npts, dt, tau);
04   module_RC_int_LP (s, p, npts, dt, tau);
05   module_CR_diff_HP(p, s, npts, dt, tau);
06   for (i=0; i<npts; i++)
07   { if (s[i] > s[i_max]) i_max=i;
08     if (s[i] < s[i_min]) i_min=i;
```

```
09   }
10   if (i_min > i_max)
11   { if (fabs(s[i_min]) > fabs(s[i_max]))
12     { for (i=i_min-1; i>i_max; i--)
13         if (s[i+1]*s[i] < 0) return func_interpolate(s, i, 0, dt);
14     }
15     else
16     { for (i=i_max+1; i<i_min; i++)
17         if (s[i-1]*s[i] < 0) return func_interpolate(s, i-1, 0, dt);
18     }
19   }
20   else
21   { if (fabs(s[i_max] > s[i_min]))
22     { for (i=i_max-1; i>i_min; i--)
23         if (s[i+1]*s[i] < 0) return func_interpolate(s, i, 0, dt);
24     }
25     else
26     { for (i=i_min+1; i<i_max; i++)
27         if (s[i-1]*s[i] < 0) return func_interpolate(s, i-1, 0, dt);
28     }
29   }
30   return no_success;}
31 }


00 double module_zccft (const double *v, double *s, int npts, int sign,
int delay, double reduct_fact, double dt, int start, int stop,
double no_success)
01 { int i, i_max=start, i_min=start;
02   if (start < delay) start=delay;
03   for (i=start; i<stop; i++)
04   { s[i]=(-1)*reduct_fact*v[i]+v[i-delay];
05     if (s[i] > s[i_max]) i_max=i;
06     if (s[i] < s[i_min]) i_min=i;
07   }
08   if (i_min > i_max)
09   { if (fabs(s[i_min]) > fabs(s[i_max]))
10     { for (i=i_min-1; i>i_max; i--)
11         if (s[i+1]*s[i] < 0) return func_interpolate(s, i, 0, dt);
12     }
13     else
14     { for (i=i_max+1; i<i_min; i++)
15         if (s[i-1]*s[i] < 0) return func_interpolate(s, i-1, 0, dt);
16     }
17   }
18   else
19   { if (fabs(s[i_max] > s[i_min]))
20     { for (i=i_max-1; i>i_min; i--)
21         if (s[i+1]*s[i] < 0) return func_interpolate(s, i, 0, dt);
22     }
```

```
23    else
24    { for (i=i_min+1; i<i_max; i++)
25        if (s[i-1]*s[i] < 0) return func_interpolate(s, i-1, 0, dt);
26    }
27  }
28  return no_success;}
29 }


00 double module_cft (const double *v, int sign, int start, int stop,
double fraction, double dt, double no_success)
01 { int i_max=func_extreme_value(v,start,stop,sign);
02   int i=i_max;
03   if (fraction == 1.0) return i_max*dt;
04   else
05   { while (sign*v[i] > fraction*sign*v[i_max]) i--;
06     return func_interpolate(v, i, fraction*v[i_max], dt);
07   }
08 }


00 double module_fcft (const double *v, const double *t, int sign,
int start, int stop, double low, double fraction, double high,
double dt, double no_success)
01 { int i_max=func_extreme_value(v,start,stop,sign);
02   double v_rms=func_rms(v,start,start+100);
03   if (v[i_max]*sign < 5*v_rms) return no_success;
04   int i=i_max, i_low=0, i_trig=0, i_high=0, bl_start=0, bl_length=20;
05   double v_max = v[i_max], v_trig=0.0, v_bl=0;
06   double a0=0, a1=0, a2=0, t_max=0, t_trig1=0, t_trig2=0;
07   if (low == 0.0) low=5*v_rms;
08   while (sign*v[i] > high*sign*v_max) i--;
09   i_high=i;
10   while (sign*v[i] > fraction*sign*v_max) i--;
11   i_trig=i;
12   while (sign*v[i] > low) i--;
13   i_low=i+1;
14   if (sign*v[i_max-1] < sign*v[i_max+1])
15     gGraph = new TGraph(4,&(t[i_max-1]),&(v[i_max-1]));
16   else
17     gGraph = new TGraph(4,&(t[i_max-2]),&(v[i_max-2]));
18   TF1 *f1 = new TF1("f1","pol2",t[i_max-2],t[i_max+2]);
19   if (gGraph->Fit(f1,"RNQF") == 0)
20   { a0=f1->GetParameter(0);
21     a1=f1->GetParameter(1);
22     a2=f1->GetParameter(2);
23     if (a2 != 0)
24     { t_max=(-0.5)*a1/a2;
25       v_max=(4*a2*a0-a1*a1)/(4*a2);
26     }
27     f1->Delete();
```

```
28     gGraph->Delete();
29     if (fraction == 1.0) return t_max;
30   }
31   else
32   { f1->Delete();
33     gGraph->Delete();
34     return no_success;
35   }
36   if ((i_low-1-bl_length) < 0)
37   { bl_start=0;
38     bl_length=i_low-1;
39   }
40   else
41     bl_start=i_low-1-bl_length;
42   v_bl=func_average (v, bl_start, bl_start+bl_length);
43
44   v_trig=fraction*(v_max-v_bl)+v_bl;
45   if (sign*v_trig >= sign*v[i_trig])
46     gGraph = new TGraph(4,&(t[i_trig-1]),&(v[i_trig-1]));
47   else
48     gGraph = new TGraph(4,&(t[i_trig-2]),&(v[i_trig-2]));
49   TF1 *f2 = new TF1("f2","pol2",t[i_trig-2],t[i_trig+2]);
50   if (gGraph->Fit(f2,"RNQF") == 0)
51   { a0=f2->GetParameter(0);
52     a1=f2->GetParameter(1);
53     a2=f2->GetParameter(2);
54     t_trig1=a1/(-2.0)/a2+sqrt(a1*a1/4.0/a2/a2+(v_trig-a0)/a2);
55     t_trig2=a1/(-2.0)/a2-sqrt(a1*a1/4.0/a2/a2+(v_trig-a0)/a2);
56     f2->Delete();
57     gGraph->Delete();
58     if (fabs(t[i_trig]-t_trig1) < fabs(t[i_trig]-t_trig2))
59       return t_trig1;
60     else
61       return t_trig2;
62   }
63   else
64   { f2->Delete();
65     gGraph->Delete();
66     return no_success;
67   }
68 }
```

Appendix B

Mathematical Supplements

B.1 Derivation of the Response of a Charge-Sensitive Preamplifier

In subsection 3.1.3 an AC-coupled charge-sensitive resistive feedback preamplifier, shown in figure 3.4 schematically, is introduced. In this section, the response of this preamplifier to the detector current $I_{det}(t)$ is derived. Therewith, the responses $U_i(t)$ to the currents $I_i(t)$ from equations (3.5) and their local extreme values U_i^{ext} are determined.

The components of the preamplifier's feedback circuit are a resistor with the resistance R_f and a capacitor with the capacitance C_f. For the operational amplifier it is assumed that the input impedance is infinite, resulting in zero input currents, and that there is no offset voltage between the inputs. Using Kirchhoff's Current Law and Kirchhoff's Voltage Law one gets

$$
\begin{aligned}
0 &= I_{det}(t) + I_R(t) + I_C(t) \\
&= I_{det}(t) + \frac{1}{R_f}U(t) + \frac{d}{dt}Q(t) \\
&= I_{det}(t) + \frac{1}{R_f}U(t) + C_f\frac{d}{dt}U(t)
\end{aligned}
$$

resulting in the ordinary first-order inhomogeneous linear differential equation

$$
\frac{1}{\tau}U(t) + \frac{d}{dt}U(t) = \frac{1}{C_f}I_{det}(t) \tag{B.1}
$$

for the output voltage signal $U(t)$, in which $\tau = R_f C_f$ is the time constant. A general solution of equation (B.1) is the superposition of one particular solution of equation (B.1) and the general solution of the corresponding homogeneous differential equation

$$
\frac{1}{\tau}U(t) + \frac{d}{dt}U(t) = 0 \tag{B.2}
$$

which can be solved using the method of seperation of variables leading to

$$
U_{hom}(t) = A \cdot e^{-t/\tau} \tag{B.3}
$$

with the integration constant A. To find a particular solution of equation (B.1) the method of variation of parameters with the ansatz

$$
U_{part}(t) = a(t) \cdot U_{hom}(t) \tag{B.4}
$$

is used. Inserting equation (B.4) into (B.1) one finds

$$a(t) = -\frac{1}{C_f A} \int_{-\infty}^{t} I_{det}(t') \cdot e^{t'/\tau} dt' \quad . \tag{B.5}$$

Finally, the general solution of (B.1) is

$$
\begin{aligned}
U_{inhom}(t) &= U_{hom}(t) + U_{part}(t) \\
&= A \cdot e^{-t/\tau} - \frac{1}{C_f} \int_{-\infty}^{t} I_{det}(t') \cdot e^{-(t-t')/\tau} dt' \quad .
\end{aligned}
\tag{B.6}
$$

Straitening on detector currents $I_{det}(t) = 0$ for $t < 0$ and the consequential inital condition $U(t) = 0$ for $t < 0$, equation (B.6) is

$$U(t) = -\frac{1}{C_f} \int_{0}^{t} I_{det}(t') \cdot e^{-(t-t')/\tau} dt' \quad . \tag{B.7}$$

With equation (B.7) the output voltage signals of the preamplifier $U_i(t)$ are determined for the detector currents $I_i(t)$ from equation (3.5). Using the locale extreme values $U_i^{min} = U_i(t_i^{min})$ the ballistic deficit $BD_i = 1 - U_i^{min}/(-Q_0/C_f)$ is derived.

$$I_1(t) = \begin{cases} Q_0/\theta & : \quad 0 \le t < \theta \\ 0 & : \quad \theta \le t \end{cases} \tag{B.8}$$

$$U_1(t) = -\frac{Q_0}{C_f} \cdot \frac{\tau}{\theta} \cdot \begin{cases} \left(1 - e^{-t/\tau}\right) & : \quad 0 \le t < \theta \\ \left(e^{\theta/\tau} - 1\right) \cdot e^{-t/\tau} & : \quad \theta \le t \end{cases} \tag{B.9}$$

$$t_1^{min} = \theta \quad \text{(follows from the monotonicity of } U_1(t)) \tag{B.10}$$

$$BD_1 = 1 - \frac{\tau}{\theta}\left(1 - e^{-\theta/\tau}\right) \tag{B.11}$$

$$I_2(t) = \begin{cases} 0.75 \cdot Q_0/\theta & : \quad 0 \le t < \theta \\ 0.25 \cdot Q_0/\theta & : \quad \theta \le t < 2\theta \\ 0 & : \quad 2\theta \le t \end{cases} \tag{B.12}$$

$$U_2(t) = -\frac{Q_0}{C_f} \cdot \frac{\tau}{\theta} \cdot \begin{cases} 0.75 - 0.75 \cdot e^{-t/\tau} & : \quad 0 \le t < \theta \\ 0.25 + \left(0.5 \cdot e^{\theta/\tau} - 0.75\right) \cdot e^{-t/\tau} & : \quad \theta \le t < 2\theta \\ \left(0.25 \cdot e^{2\theta/\tau} + 0.5 \cdot e^{\theta/\tau} - 0.75\right) \cdot e^{-t/\tau} & : \quad 2\theta \le t \end{cases} \tag{B.13}$$

$$t_2^{min} = \begin{cases} \theta & : \quad \theta \ge \tau \cdot \ln\frac{3}{2} \\ 2\theta & : \quad \theta < \tau \cdot \ln\frac{3}{2} \end{cases} \quad \begin{array}{l} \text{(follows from } \frac{d}{dt}U_2(t) = 0 \\ \text{for } \theta < t < 2\theta \text{ and from the} \\ \text{monotonicity of } U_2(t)) \end{array} \tag{B.14}$$

$$BD_2 = \begin{cases} 1 - 0.75 \cdot \frac{\tau}{\theta}\left(1 - e^{-\theta/\tau}\right) & : \quad \theta \ge \tau \cdot \ln\frac{3}{2} \\ 1 - 0.25 \cdot \frac{\tau}{\theta}\left(1 + 2 \cdot e^{-\theta/\tau} - 3 \cdot e^{-2\theta/\tau}\right) & : \quad \theta < \tau \cdot \ln\frac{3}{2} \end{cases} \tag{B.15}$$

$$I_3(t) \;=\; e^{-t/\theta} \cdot Q_0/\theta \qquad\qquad\qquad\qquad :\quad 0 \le t \tag{B.16}$$

$$U_3(t) \;=\; -\frac{Q_0}{C_f} \cdot
\begin{cases}
\dfrac{\tau}{\tau - \theta} \cdot \left(e^{-t/\tau} - e^{-t/\theta}\right) & :\quad \tau \ne \theta \\[2ex]
\dfrac{t}{\tau} \cdot e^{-t/\tau} & :\quad \tau = \theta
\end{cases} \tag{B.17}$$

$$t_3^{min} \;=\;
\begin{cases}
\dfrac{\tau\theta}{\tau - \theta} \ln \dfrac{\tau}{\theta} & :\quad \tau \ne \theta \qquad \text{(follows from} \\[2ex]
\theta & :\quad \tau = \theta \qquad \frac{d}{dt}U_3(t) = 0 \text{ for } t = t_3^{min}\text{)}
\end{cases} \tag{B.18}$$

$$BD_3 \;=\;
\begin{cases}
1 - \left(\dfrac{\theta}{\tau}\right)^{\theta/(\tau - \theta)} & :\quad \tau \ne \theta \\[2ex]
1 - e^{-1} & :\quad \tau = \theta
\end{cases} \tag{B.19}$$

$$I_4(t) \;=\; \delta(t) \cdot Q_0 \tag{B.20}$$

$$U_4(t) \;=\; -(Q_0/C_f) \cdot e^{-t/\tau} \quad :\quad 0 \le t \tag{B.21}$$

$$t_4^{min} \;=\; 0 \quad \text{(follows from the monotonicity of } U_4(t)\text{)} \tag{B.22}$$

$$BD_4 \;=\; 0 \tag{B.23}$$

B.2 Derivation of the Recursive High- and Low-Pass Filter

In analog electronics a passive, first-order high- and low-pass filter can be realized by a simple RC-circuit consisting of a capacitor C and a resistor R connected in series. Applying an input voltage signal $U(t)$ across the circuit the voltage signals $U_R(t)$ across the resistor and $U_C(t)$ across the capacitor are the output voltage signals of a high- and low-pass filter. Kirchhoff's Voltage Law for this system is

$$U(t) = U_C(t) + U_R(t) \quad . \tag{B.24}$$

Using Ohm's Law, the definition of the electric current, the definition of the capacitance and equation (B.24) one gets

$$\begin{aligned}
U_R(t) &= R \cdot I_R(t) = R \cdot \frac{d}{dt}Q(t) = R \cdot C \cdot \frac{d}{dt}U_C(t) \\[1ex]
&= \tau \cdot \frac{d}{dt}\left[U(t) - U_R(t)\right] \tag{B.25} \\[2ex]
U_C(t) &= U(t) - U_R(t) = U(t) - R \cdot C \cdot \frac{d}{dt}U_C(t) \\[1ex]
&= U(t) - \tau \cdot \frac{d}{dt}U_C(t) \tag{B.26}
\end{aligned}$$

where $\tau = R \cdot C$ is the time constant of the filter. These formulas are discretized by the substitutions

$$U_R(t), U_C(t) \;\rightarrow\; s(n \cdot \Delta t) = s_n \tag{B.27}$$

$$U(t) \;\rightarrow\; v(n \cdot \Delta t) = v_n \tag{B.28}$$

$$\frac{d}{dt}f(t) \;:=\; \lim_{t_0 \to t} \frac{f(t_0) - f(t)}{t_0 - t} = \frac{f(t) - f(t - \Delta t)}{\Delta t} \tag{B.29}$$

which convert equation (B.25) to

$$
\begin{aligned}
s_n &= \frac{\tau}{\Delta t} \cdot (v_n - v_{n-1} - s_n + s_{n-1}) \\
&= \frac{\tau}{\tau + \Delta t} \cdot (s_{n-1} + v_n - v_{n-1})
\end{aligned}
\tag{B.30}
$$

and equation (B.26) to

$$
\begin{aligned}
s_n &= v_n - \frac{\tau}{\Delta t} \cdot (s_n - s_{n-1}) \\
&= \frac{\tau}{\tau + \Delta t} \cdot s_{n-1} + \left(1 - \frac{\tau}{\tau + \Delta t}\right) \cdot v_n \quad.
\end{aligned}
\tag{B.31}
$$

B.3 Derivation of the parameters M and N for the Jordonav-Trapezoid-Shaper

Starting from the recursive formulas of the JTS

$$
\begin{aligned}
d_n &= v_n - v_{n-k} - v_{n-k-m} + v_{n-2 \cdot k-m} \\
p_n &= p_{n-1} + d_n \\
s_n &= s_{n-1} + N \cdot (p_n + M \cdot d_n)
\end{aligned}
\tag{B.32}
$$

and provided that $v_n = d_n = p_n = s_n = 0$ for $n < 0$, iterative formulas can be derived for $0 \le n < k$

$$
\begin{aligned}
d_n &= v_n \\
p_n &= \sum_{i=0}^{n} d_i = \sum_{i=0}^{n} v_i \\
s_n &= N \cdot \sum_{i=0}^{n} (p_i + M \cdot d_i) = N \cdot \sum_{i=0}^{n} \left(\sum_{j=0}^{i} v_j + M \cdot v_i \right) \\
&= N \cdot \sum_{i=0}^{n} (M + n - i + 1) \cdot v_i
\end{aligned}
\tag{B.33}
$$

and for $n = k$

$$d_k = v_k - v_0 \tag{B.34}$$

$$p_k = \sum_{i=0}^{k-1} v_i + v_k - v_0 = \sum_{i=1}^{k} v_i \tag{B.35}$$

The rising slope of the trapezoidal shape is k samples long and starts at $n = 0$, so the slope finishes at $n = k - 1$, where the flat top is starting. Hence, $s_n = s_{n-1}$ for $k \leq n < k + m$ and with equations (B.32), (B.34), (B.35) in the case $n = k$ it follows

$$s_k = s_{k-1} + N \cdot \left(\sum_{i=1}^{k} v_i + M \cdot (v_k - v_0) \right)$$

$$\Rightarrow M = \frac{1}{v_0 - v_k} \cdot \left(\sum_{i=0}^{k} v_i - v_0 \right) \quad .$$

The purpose of this algorithm is to convert an exponentially decaying signal $v(t)$ with an amplitude A and a time constant τ into a trapezoidal shaped signal. With the sampling interval Δt one gets

$$v(t) = A \cdot e^{-t/\tau}$$
$$v_n = v(n \cdot \Delta t) = A \cdot \left(e^{-\Delta t/\tau} \right)^n := A \cdot c^n \tag{B.36}$$

resulting in

$$M = \frac{1}{1 - c^k} \cdot \left(\sum_{i=0}^{k} c^i - 1 \right)$$

and, using the properties of the geometric sequence, finally in

$$\begin{aligned}
M &= \frac{1}{1 - c^k} \cdot \frac{1 - c^{k+1}}{1 - c} - \frac{1}{1 - c^k} = \frac{1 - c^{k+1} - 1 + c}{(1 - c^k)(1 - c)} \\
&= \frac{c \cdot (1 - c^k)}{(1 - c^k)(1 - c)} = \frac{c}{1 - c} = \frac{1}{c^{-1} - 1} \\
&= \frac{1}{e^{\Delta t/\tau} - 1} \quad .
\end{aligned} \tag{B.37}$$

Since $\Delta t/\tau$ is usually small, one can use the first-order approximation $e^{\Delta t/\tau} \approx 1 + \Delta t/\tau$ to estimate M. It results in $M \approx \tau/\Delta t$.

The normalization factor N has to guarantee that $s_n = A$ for $k - 1 \leq n < k + m$, in which case A is the amplitude of v_n in equation (B.36). In the case $n = k + 1$ equation (B.33) turns into

$$s_{k-1} = A \cdot N \cdot \left((M + k) \cdot \sum_{i=0}^{k-1} c^i - \sum_{i=0}^{k-1} i \cdot c^i \right) \quad . \tag{B.38}$$

Using the relation

$$\sum_{i=0}^{n} i \cdot c^i = \frac{c - (n+1) \cdot c^{n+1} + n \cdot c^{n+2}}{(1 - c)^2}$$

and again the properties of the geometric sequence, equation (B.38) can be written as

$$\begin{aligned}
s_{k-1} &= A \cdot N \cdot \left((M + k) \cdot \frac{1 - c^k}{1 - c} - \frac{c - (n+1) \cdot c^{n+1} + n \cdot c^{n+2}}{(1 - c)^2} \right) \\
&= A \cdot N \cdot \left(\frac{(M + k)(1 - c^k)(1 - c) - c + (n+1) \cdot c^{n+1} - n \cdot c^{n+2}}{(1 - c)^2} \right) \quad .
\end{aligned}$$

After arranging the numerator by powers of c and applying $s_n = A$ the normalization factor is

$$N = \frac{(1-c)^2}{M + k - (M + k + 1) \cdot c - M \cdot c^k + (M + 1) \cdot c^{k+1}} \tag{B.39}$$

with $c = e^{-\Delta t/\tau}$.

B.4 Relation between Mowing Window Deconvolution and Jordonav-Trapezoid-Shaper

In this section the identity of the MWD with the parameter $m = l$ and the JTS with the parameters $k = 1$ and $m = l - 1$ is shown. The moving window deconvolution is given by the formulas

$$s_n = v_n - v_{n-l} + \alpha \sum_{i=n-l}^{n-1} v_i \tag{B.40}$$

$$\alpha = 1 - e^{-\Delta t/\tau} \tag{B.41}$$

while the trapezoidal shaper by Jordanov is given by the formulas

$$d_n = v_n - v_{n-1} - v_{n-l} + v_{n-l-1} \tag{B.42}$$

$$p_n = p_{n-1} + d_n \tag{B.43}$$

$$s_n = s_{n-1} + N \cdot (p_n + M \cdot d_n) \tag{B.44}$$

$$M = \frac{1}{e^{\Delta t/\tau} - 1} \tag{B.45}$$

$$N = \frac{1}{M + 1} \quad . \tag{B.46}$$

The last formula follows from equation (B.39) in the case $k = 1$. Equations (B.41), (B.45) and (B.46) result in

$$M = \frac{1}{\alpha} - 1 \tag{B.47}$$

$$N = \alpha \tag{B.48}$$

and, provided that $v_n = 0$ for $n < 0$, from equations (B.42) and (B.43) results

$$p_n = v_n - v_{n-l} \quad . \tag{B.49}$$

Using the equations (B.47), (B.48) and (B.49), the JTS from equation (B.44) can be expressed by

$$\begin{aligned} s_n &= s_{n-1} + \alpha \left(p_n - d_n \right) + d_n \\ &= s_{n-1} + \alpha \left(v_{n-1} - v_{n-l-1} \right) + d_n \quad . \end{aligned} \tag{B.50}$$

Equation (B.50) is exactly the recursive expression of the MWD described in equation (B.40).

B.5 Asymmetric Gaussian Function

With the formulas

$$F_k^j = \frac{0.565\, A_j}{\sqrt{2}\,\sigma} \cdot \left(e^{-\frac{(k-k_j)^2}{2\,\sigma^2}} + \frac{1.772\, A_{as}\, \sqrt{2}\,\sigma}{\lambda} \cdot e^{\left(\frac{k-k_j}{\lambda} + \frac{\sigma^2}{2\,\lambda^2}\right)} \cdot G\left(\frac{k-k_j}{\sqrt{2}\,\sigma} + \frac{\sigma}{\sqrt{2}\,\lambda}\right) \right)$$

$$G(x) = 0.5 \cdot erfc(x) \approx \left(e^{(\alpha \cdot x + \beta \cdot x^3)} + 1 \right)^{-1} \tag{B.51}$$

an asymmetric Gaussian function is defined [39]. Thereby j enumerates one of several peaks. The other notations are

$$
\begin{array}{ll}
k & \text{position (bin or channel)} \\
F_k^j & \text{value of peak } j \text{ at position } k \\
A_j & \text{area of peak } j \\
k_j & \text{position of peak } j \\
\sigma^2 & \text{variance of the symmetric part} \\
A_{as} & \text{area of the asymmetric part relative to } A_j \\
\lambda & \text{asymmetry parameter} \\
erfc(x) & \text{complementary error function}
\end{array}
\tag{B.52}
$$

The complementary error function $erfc(x)$ is parametrized with the constants $\alpha = 2.25718$ and $\beta = 0.202197$.

Bibliography

[1] KNOLL, G. F. *Radiation Detection and Measurement.* John Wiley & Sons, Inc., New York, 3rd edition (1999).

[2] LEO, W. R. *Techniques for Nuclear and Particle Physics Experiments.* Springer-Verlag, Berlin, 2nd edition (1994).

[3] KOWALSKI, E. *Nuclear Electronics.* Springer-Verlag, Berlin (1970).

[4] GABRIEL, F., ET AL. The Rossendorf radiation source ELBE and its FEL projects. *Nuclear Instruments and Methods in Physics Research B* 161 (2000) 1143–1147.

[5] WAGNER, A., ET AL. The new bremsstrahlung facility at the superconducting electron accelerator ELBE. *Journal of Physics G* 31 (2005) 1969.

[6] SCHWENGNER, R., ET AL. The photon-scattering facility at the superconducting electron accelerator ELBE. *Nuclear Instruments and Methods in Physics Research A* 555 (2005) 211.

[7] ALTSTADT, E., ET AL. A photo-neutron source for time-of-flight measurements at the radiation source ELBE. *Annals of Nuclear Energy* 34 (2007) 36.

[8] KLUG, J., ET AL. Development of a neutron time-of-flight source at the ELBE accelerator. *Nuclear Instruments and Methods in Physics Research A* 577 (2007) 641.

[9] BEYER, R., ET AL. Proton-recoil detectors for time-of-flight measurements of neutrons with kinetic energies from some tens of keV to a few MeV. *Nuclear Instruments and Methods in Physics Research A* 575 (2007) 449.

[10] BARDELLI, L. AND POGGI, G. Digital-sampling systems in high-resolution and wide dynamic-range energy measurements: Comparison with peak sensing adcs. *Nuclear Instruments and Methods in Physics Research A* 560 (2006) 517.

[11] Product information *High-speed 10-bit PXI/compactPCI digitizers.* Acqiris, Geneva, Switzerland. Available online: http://www.acqiris.com/products/digitizers/10-bit-cpci-6u-digitizers/dc282/datasheet/DC282-DC252-DC222.pdf (2008, September 18).

[12] User manual *Agilent Acqiris 10-bit digitizers.* Agilent Technologies, Santa Clara, CA, USA. Available online: http://cp.literature.agilent.com/litweb/pdf/U1092-90004.pdf (2008, September 18).

[13] Product information *PowerMIDAS C5000.* VMETRO, Oslo, Norway. Available online: http://www.vmetro.com/category4314.html (2008, September 18).

[14] Product information *VS-FC41F*. VMETRO, Oslo, Norway. Available online: http://www.vmetro.com/category3836.html (2008, September 18).

[15] Product information *SAN Access Kit*. VMETRO, Oslo, Norway. Available online: http://www.vmetro.com/category3859.html (2008, September 18).

[16] Product information *ProLiant DL380 G5*. Hewlett-Packard, Palo Alto, CA, USA. Available online: http://h18006.www1.hp.com/products/storageworks/dl380g5_ss/ (2008, September 18).

[17] Dammrau, A., Forschungszentrum Dresden-Rossendorf. Private communication.

[18] Brun, R., et al. *ROOT User Guide 5.20*. CERN, Geneva, Switzerland (2008). Available online: http://root.cern.ch/root/doc/RootDoc.html (2008, September 18).

[19] Product information *BNC Model BL-2 Fast Tail Pulse Generator*. Berkeley Nucleonics Corporation, San Rafael, CA, USA. Available online: http://www.berkeleynucleonics.com/products/model-bl2.html (2008, September 22).

[20] Berger, M., et al. *XCOM: Photon Cross Section Database (version 1.3)*. National Institute of Standards and Technology, Gaithersburg, MD, USA (2005). Available online: http://physics.nist.gov/xcom (2008, August 4).

[21] Goulding, F. S. and Landis, D. A. Ballistic deficit correction in semiconductor detector spectrometers. *IEEE Transactions on Nuclear Science* 35, 1 (1988) 119–124.

[22] Georgiev, A. and Gast, W. Digital pulse processing in high resolution, high throughput gamma-ray spectroscopy. *IEEE Transactions on Nuclear Science* 40, 4 (1993) 770–779.

[23] Büchner, A., et al. Schaltungsanordnung für die digitale Verarbeitung von Halbleiterdetektorsignalen. Patent EP 0 550 830 A1, 14.07.1993.

[24] Stein, J., et al. X-ray detectors with digitized preamplifiers. *Nuclear Instruments and Methods in Physics Research B* 113 (1996) 141–145.

[25] Jordanov, V. T. and Knoll, G. F. Digital synthesis of pulse shapes in real time for high resolution radiation spectroscopy. *Nuclear Instruments and Methods in Physics Research A* 345 (1994) 337–345.

[26] Product information *GAMMA-X Germanium (HPGe) Coaxial Detectors*. ORTEC, Oak Ridge, TN, USA. Available online: http://www.ortec-online.com/detectors/photon/b2_2.htm (2008, September 22).

[27] Ekström, L. and Firestone, R. *WWW Table of Radioactive Isotopes, database version 2/28/99*. Available online: http://ie.lbl.gov/toi/index.htm (2008, September 22).

[28] Product information *671 Spectroscopy Amplifier*. ORTEC, Oak Ridge, TN, USA. Available online: http://www.ortec-online.com/electronics/amp/671.htm (2008, September 22).

[29] Product information *Model 7423/UHS 16k Ultra High-Speed Spectroscopy*. SILENA INTERNATIONAL, Cernusco sul Naviglio, Italy. Available online: http://www.geocities.com/silena_spa/silena/products/nimadc/742316k.htm (2008, September 22).

[30] GIESEN, F.-J. *Entwicklung eines Hochgeschwindigkeits-ADC-Controllers für Datenaufnahmesystem in der Kernphysik*. Diploma thesis, Universität zu Köln (1996).

[31] BIRKS, J. *The Theory and Practice of Scintillation Counting*. Pergamon Press, Oxford (1964).

[32] Product information *EJ-200 Plastic Scintillator*. Eljen Technology, Sweetwater, TX, USA. Available online: http://www.eljentechnology.com/datasheets/EJ200%20data%20sheet.pdf (2008, September 26).

[33] Product information *R2059 Photomultiplier Tube*. Hamamatsu Photonics Deutschland GmbH, Herrsching am Ammersee, Germany. Available online: http://sales.hamamatsu.com/index.php?id=13189280 (2008, September 26).

[34] Product information *PHQ PMT-base integrated high-voltage power supply*. Iseg Spezialelektronik GmbH, Radeberg, Germany. Available online: http://www.iseg-hv.de/download.php/500/file_url_de/iseg_PHQ.pdf (2008, September 26).

[35] BEČVÁŘ, F., ET AL. The asset of ultra-fast digitizers for positron-lifetime spectroscopy. *Nuclear Instruments and Methods in Physics Research A* 539 (2005) 372.

[36] Courtesy of R. BEYER, Forschungszentrum Dresden-Rossendorf.

[37] HEIDEL, K. *5fold CFD - Technical Information Manual*. Forschungszentrum Dresden-Rossendorf, Germany (2006). Available online: http://www.fzd.de/db/Cms?pOid=22647 (2008, September 22).

[38] Product information *V1190A 128 Channel Multihit TDC*. CAEN, Viareggio, Italy. Available online: http://www.caen.it/nuclear/product.php?mod=V1190A (2008, September 22).

[39] SCHWENGNER, R., Forschungszentrum Dresden-Rossendorf. Private communication.

Danksagung / Acknowledgement

Erklärung / Declaration

Hiermit erkläre ich, dass ich diese Arbeit selbstständig und ohne andere als die angegebenen Hilfsmittel angefertigt habe.

_____   _____
Ort, Datum der Abgabe   Unterschrift